Rijksuniversiteit Groningen

Atmospheric Variability and the Atlantic Multidecadal Oscillation

Mathematical Analysis of Low-Order Models

Proefschrift

ter verkrijging van het doctoraat in de
Wiskunde en Natuurwetenschappen
aan de Rijksuniversiteit Groningen
op gezag van de
Rector Magnificus, dr. F. Zwarts,
in het openbaar te verdedigen op
vrijdag 1 oktober 2010
om 16.15 uur

door

Alef Edou Sterk

geboren op 25 april 1982
te Sneek

Promotores:	Prof. dr. H.W. Broer
	Prof. dr. C. Simó
	Prof. dr. ir. H.A. Dijkstra
Beoordelingscommissie:	Prof. dr. A. Doelman
	Prof. dr. R.S. MacKay
	Prof. dr. H. Waalkens

ISBN: 978–90–367–4475–1

Acknowledgements

Many people have made a contribution to this thesis, either directly or indirectly, and it is a pleasure to thank them all.

First of all, I would like to thank my advisors Henk Broer, Carles Simó, and Henk Dijkstra, and also Renato Vitolo, co-author of our joint papers. I have been very fortunate to be in the company of these four people. The present work would not have been written without their encouragement and strong commitment.

I express my gratitude to Professors Arjen Doelman, Robert MacKay, and Holger Waalkens for taking part in the Ph.D. committee and for reading and commenting on preliminary versions of this thesis.

The atmosphere at the Johann Bernoulli Institute for Mathematics and Computer Science has always been pleasant. I would like to thank the staff and my fellow Ph.D. students, former and present, for their contributions to the positive atmosphere.

I am indebted to the University of Barcelona for the kind hospitality during several visits. I would also like to thank the staff and Ph.D. students at MAIA for many fruitful conversations.

Finally, I would like to thank my family and friends for their sincere interest in my work and their moral support.

Groningen, Summer 2010, A.E.S.

Contents

Chapter 1

Introduction

1.1 Motivation and setting of the problem

In this work we study low-frequency variability of the North Atlantic climate system with particular emphasis on the Atlantic Multidecadal Oscillation and recurrent atmospheric flow patterns. We study suitable low-order models for the oceanic and atmospheric circulation using concepts of dynamical systems theory.

Models for climatological phenomena typically involve a Hopf bifurcation. A particular example is El Niño (Dijkstra, 2005, Chapter 7). In the models of the present work a Hopf bifurcation leads to periodic attractors representing multidecadal temperature swings in the ocean and planetary waves in the atmosphere. Along several routes to chaos the periodic attractors bifurcate into strange attractors. Key notions are unpredictability and low-dimensional chaos (Broer and Takens, 2010), which have also been associated with the onset of turbulence (Ruelle and Takens, 1971). In the ocean model we find (quasi-periodic) period doublings leading to (quasi-periodic) Hénon-like strange attractors. In the atmosphere model we find period doubling cascades, Hopf-Neĭmark-Sacker bifurcations followed by the breakdown of a quasi-periodic attractor, and intermittency.

The present study is a typical example of *experimental mathematics*. Even in the simplified setting of this work rigorous proofs are out of reach so that mathematical theorems are replaced by educated guesses.

Motivation and aims. Observational and model based studies provide evidence for variability in the North Atlantic sea surface temperature with a time scale of several decades. This phenomenon is called the Atlantic Multidecadal Oscillation (AMO). Investigations with ocean-only models show that the spatio-temporal properties of the AMO are explained by an internal oscillatory mode of these models (referred

to as the AMO mode). Many studies, however, indicate that the growth rate of the AMO mode is negative due to atmospheric damping of sea surface temperature anomalies. On the other hand, the atmosphere itself shows variability on a multitude of time and spatial scales, which may excite the AMO mode. In the present work we study:

1. the dynamics of atmospheric low-frequency variability as observed at midlatitudes in the northern hemisphere;

2. the effect of atmospheric forcing on the AMO mode.

We apply concepts of dynamical systems theory to suitable low-order models.

Low-order models. In the geophysical literature, models for the atmospheric and oceanic circulation are typically derived from first principles, such as conservation laws, global balances, etc. This approach leads to systems of partial differential equations that govern the evolution of geophysical fields, such as velocity, pressure, or temperature.

In this work we derive *low-order models* from the equations of motion by means of Galerkin projections. The idea is to expand the unknown fields of the equations of motion in terms of a chosen basis, determining the spatial structure, with unknown time-dependent coefficients. In this expansion only a finite number of terms is retained. Then an orthogonal projection onto the basis gives a set of finitely many ordinary differential equations for the expansion coefficients.

Unfortunately, there is no theory which suggests how a basis must be chosen so that the dynamics of the low-order model qualitatively represent the dynamics of the original equations of motion. In the geophysical literature different bases have been used, such as Empirical Orthogonal Functions and their variants (Selten, 1995; Kwasniok, 1996), or eigenvectors computed from a linear stability problem of a particular steady state (Van der Vaart et al., 2002). Since these bases are computed numerically from a discretised model, they have the disadvantage that physical parameters have to be fixed in advance. For a bifurcation analysis, artificial parameters have to be re-introduced.

In the present study we use analytical basis functions, which are solutions of appropriate boundary value problems in order to satisfy certain boundary conditions. The advantage is that physical parameters are preserved in the projection. Hence, we can perform a bifurcation analysis where the bifurcation parameters have a straightforward physical interpretation. We select the retained basis functions based on physical considerations. We only retain those basis functions so that the truncated expansions can represent patterns on the relevant spatial scales.

1.2 Atmospheric low-frequency variability

The observed planetary-scale atmospheric circulation exhibits persistent and irregularly recurring patterns on time scales beyond 10 days during northern hemisphere winters. One way of characterising low-frequency variability is by means of spectral analysis of observed atmospheric fields. Fraedrich and Böttger (1978) studied spatio-temporal spectra of the variance of the 500 mb geopotential heights and found that the low-frequency component is characterised by temporal periods larger than 10 days and zonal wave numbers less than 5. Benzi and Speranza (1989) re-examined previous studies of amplification of waves with wave number 3 and of onset of Pacific anomalies. In addition, they summarise the main physical features of atmospheric low-frequency variability: on average planetary waves have a fixed geographic position, anomalies are vertically coherent, and low-frequency variability seems to be related to ultralong wave amplification through a non-standard form of baroclinic instability in which orography plays an essential role.

The central question of Chapter 2 is:

> Does the atmospheric variability characterising the northern hemisphere midlatitude circulation result from dynamical processes specific to the interaction of zonal flow and planetary waves with orography, and what are these processes?

To that end, we study a low-order model derived from the 2-layer shallow-water equations on a β-plane channel. The main ingredients of the low-order model are a zonal flow, a planetary scale wave (wave number 3), orography, and a baroclinic-like forcing.

We use orography height (h_0) and magnitude of zonal wind forcing (U_0) as control parameters to study the bifurcations of equilibria and periodic orbits. Along two curves of Hopf bifurcations an equilibrium loses stability ($U_0 \geq 12.5$ m/s) and gives birth to two distinct families of periodic orbits. These periodic orbits bifurcate into strange attractors along three routes to chaos: period doubling cascades, breakdown of 2-tori by homo- and heteroclinic bifurcations, or intermittency ($U_0 \geq 14.5$ m/s and $h_0 \geq 800$ m).

The observed attractors exhibit spatial and temporal low-frequency patterns comparing well with those observed in the atmosphere. For $h_0 \leq 800$ m the periodic orbits have a period of about 10 days and patterns in the vorticity field propagate eastward. For $h_0 \geq 800$ m, the period is longer (30-60 days) and patterns in the vorticity field are non-propagating. The dynamics on the strange attractors are associated with low-frequency variability: the vorticity fields show weakening and strengthening of

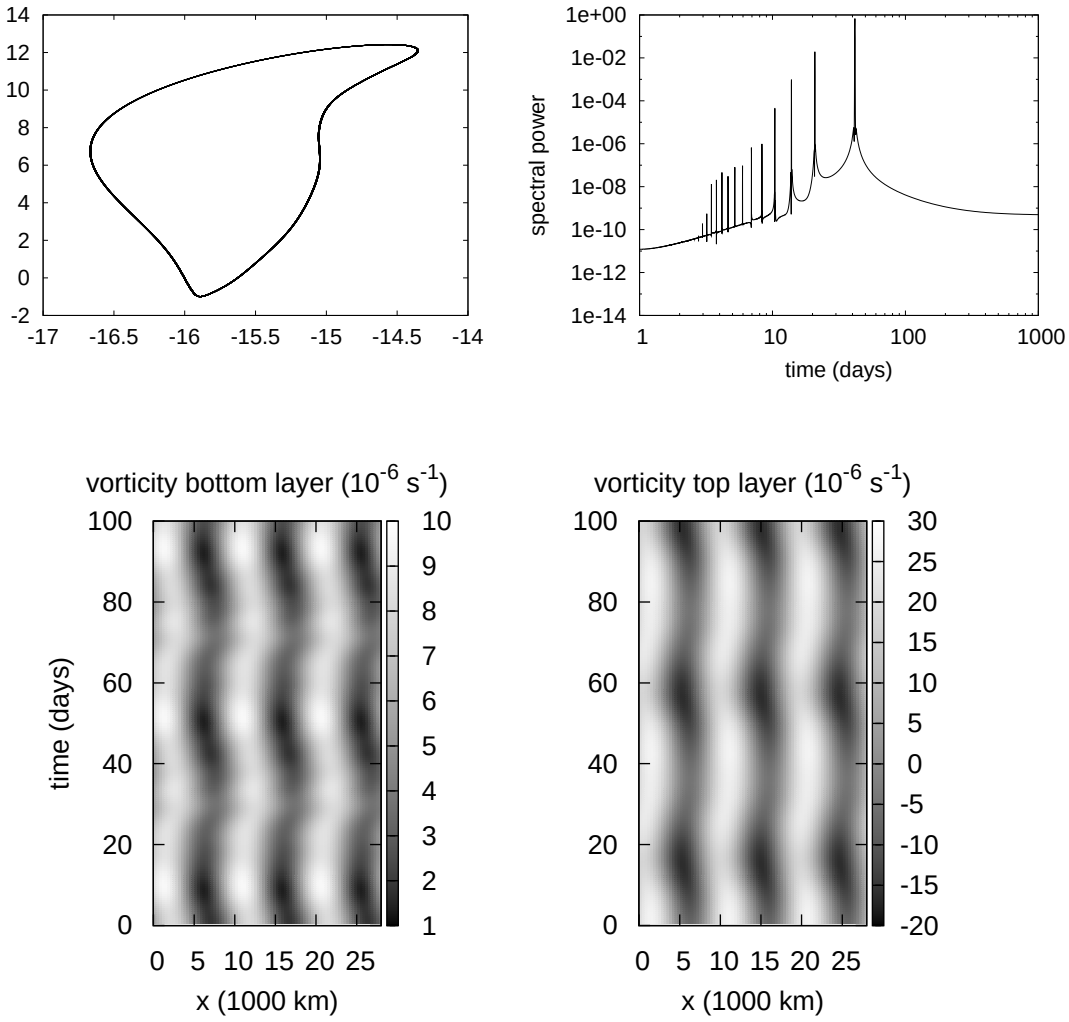

Figure 1.1. Top: Periodic orbit born at a Hopf bifurcation ($U_0 = 14.64$ m/s, $h_0 = 1400$ m) and its power spectrum. The period is approximately 60 days. Bottom: Hovmöller diagram computed from the periodic orbit in the top panel. The magnitude of the vorticity field is plotted as a function of time and longitude while keeping the latitude fixed at $y = 1250$ km. Observe that this wave is non-propagating in both layers.

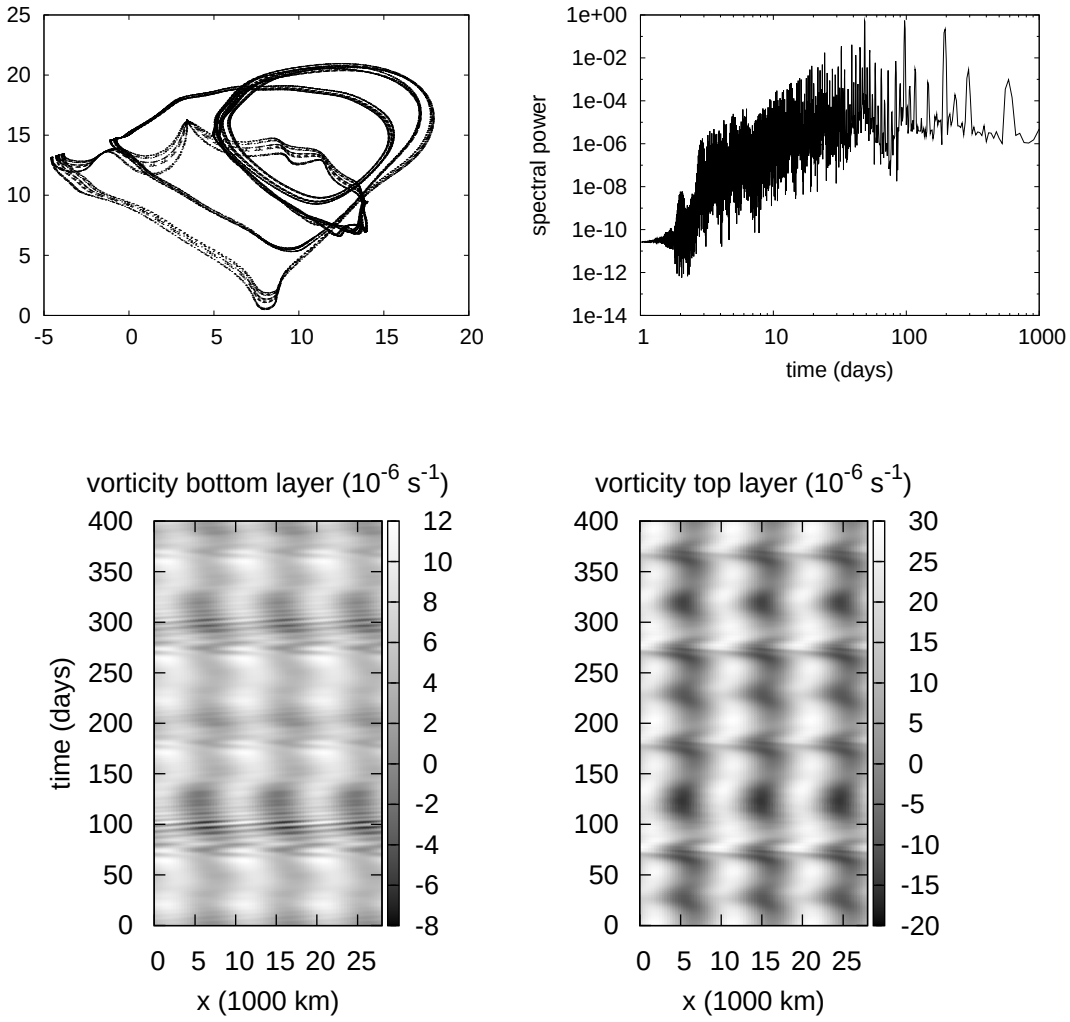

Figure 1.2. Same as Figure 1.1, but for $U_0 = 15$ m/s and $h_0 = 1400$ m. The periodic orbit has bifurcated into a strange attractor through a cascade of period doubling bifurcations. The non-propagating nature is 'inherited' from the bifurcating periodic orbit. Observe the irregular variability in the bottom layer, which is due to the harmonics induced by the period doubling bifurcations.

non-propagating planetary waves on time scales of 10-200 days. The spatio-temporal characteristics are 'inherited' (by intermittency) from the two families of periodic orbits and are detected in a relatively large region of the parameter plane. An example of this scenario for the period doubling case is shown in Figures 1.1 and 1.2.

The scenario presented in Chapter 2 is different from scenarios involving 'multiple equilibrium theories,' which associate atmospheric flow patterns with equilibria of the governing equations (Charney and DeVore, 1979). Recently, this idea has been adopted by Crommelin et al. (2004) to explain transitions between flow patterns by means of Shil′nikov-like strange attractors appearing in the Hopf-saddle-node scenario (Broer and Vegter, 1984). Such attractors give rise to intermittency near two saddle equilibria representing different flow patterns. See Broer and Vitolo (2008) for an overview of low-order atmosphere models where Shil′nikov-like strange attractors play an essential role.

1.3 The Atlantic Multidecadal Oscillation

Analyses of sea surface temperature observations provide evidence for variability in the North Atlantic Ocean with a time scale of several decades and a well-defined spatial pattern. This variability is called the Atlantic Multidecadal Oscillation (AMO). Figure 1.3 shows a specific pattern characterising the difference between the warm period 1950–1964 and the cold period 1970–1984.

The starting point for Chapter 3 is the paper of Te Raa and Dijkstra (2002) in which they study a minimal model for thermally driven flows in 3-dimensional ocean basin. Their bifurcation analysis shows the existence of an oscillatory mode, hereafter referred to as the AMO mode, which is characterised by a multidecadal time scale, westward propagation of temperature anomalies, and a phase difference between the anomalous meridional and zonal overturning circulations (Figure 1.4). The main goals of Chapter 3 are:

1. to develop a low-order model which captures the spatio-temporal signature of the AMO mode;

2. to study the stability of the AMO mode upon variation of parameters;

3. to study the effect of annual atmospheric forcing on the AMO mode.

From the model of Te Raa and Dijkstra we derive a low-order model, which consists of a system of 27 ordinary differential equations.

In models for thermally driven ocean flows different forcing mechanisms can be used. Two typical choices are restoring and prescribed heat flux. Restoring heat flux

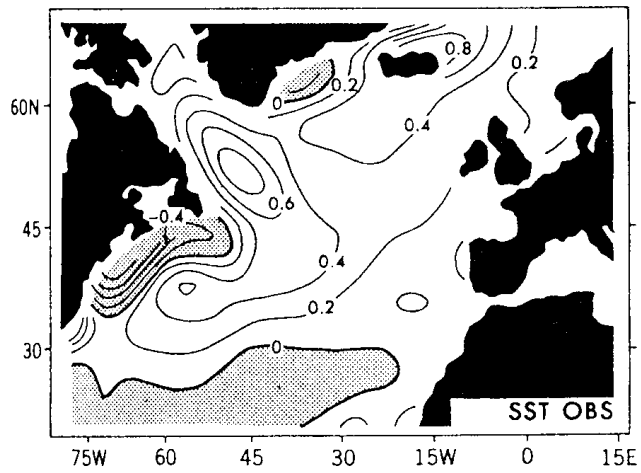

Figure 1.3. Pattern of the sea surface temperature anomaly determined by Kushnir (1994): difference between the averages taken over the warm years 1950–1964 and the cold years 1970–1984. The picture is taken from Latif (1998).

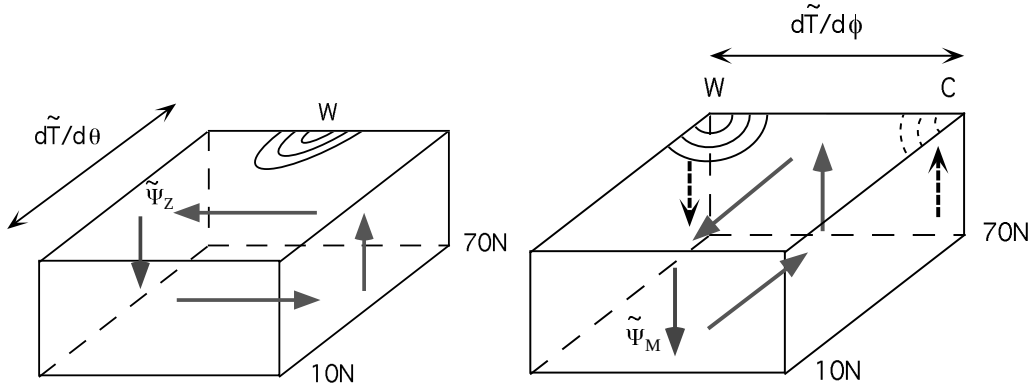

Figure 1.4. Two phases of the AMO mode as detected by Te Raa and Dijkstra (2002). A warm anomaly in the north central part of the basin induces a meridional temperature gradient, which induces an anomalous zonal overturning circulation. The latter causes the warm anomaly to travel westward, which leads to a zonal temperature gradient. The latter induces an anomalous meridional overturning circulation, and the second half of the oscillation starts.

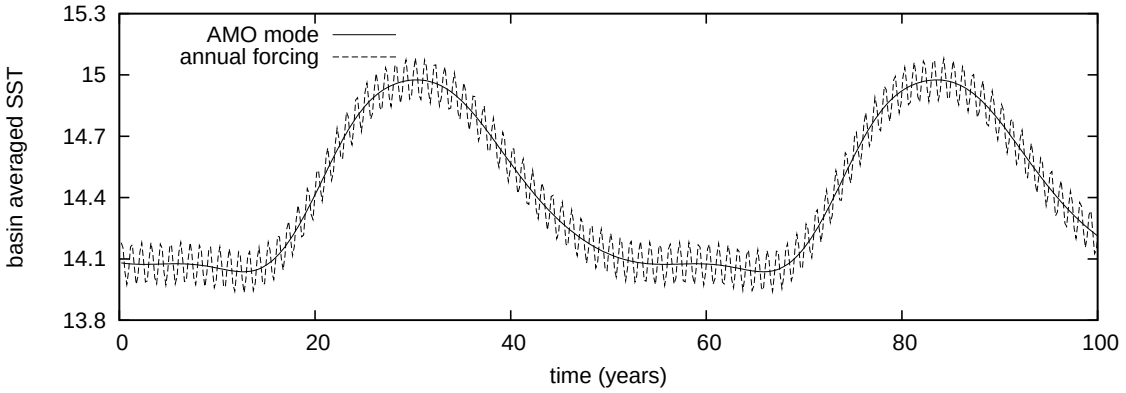

Figure 1.5. The basin averaged sea surface temperature plotted as a function of time for the AMO mode (solid) and the 2-torus attractor in the annually forced system (dashed).

is proportional to the temperature difference between the atmosphere and the sea surface, which results in atmospheric damping on sea surface temperature anomalies. Prescribed heat flux is a constant term, which results in net zero atmospheric damping.

Initially we use restoring heat flux as forcing, where a parameter Δ controls the equator-to-pole atmospheric temperature gradient. For the standard value $\Delta = 20°\text{C}$ the attractor of the low-order model is a stable equilibrium, which corresponds to a steady ocean flow. From this equilibrium we compute the corresponding heat flux which we then use as prescribed heat flux. Moreover, we introduce a parameter γ which interpolates between restoring ($\gamma = 0$) and prescribed heat flux ($\gamma = 1$). Hence, we study the stability of steady ocean flows as a function of atmospheric damping on the sea surface temperature. By increasing γ from 0 to 1 a supercritical Hopf bifurcation at $\gamma_H \approx 0.951$ gives birth to a periodic attractor, which has the spatio-temporal characteristics of the AMO mode as found by Te Raa and Dijkstra.

By means of a Poincaré return map we study the stability of the periodic orbit upon variation of the parameters Δ and γ. For $\Delta = 20°\text{C}$, the periodic orbit remains stable up to $\gamma = 1$, but for $\Delta > 20°\text{C}$ period doubling bifurcations occur. For $\Delta = 22°\text{C}$ the periodic orbit undergoes two period doublings, and for $\Delta = 24°\text{C}$ a complete cascade takes place. Strange attractors appearing after the period doubling cascade are Hénon-like: they are the closure of the unstable manifold of a saddle fixed point. See Figure 1.6 (left panel) for an example.

Finally, we impose periodic forcing to model annual variations in the surface heat flux. The Hopf bifurcation of the autonomous model turns into a Hopf-Neĭmark-

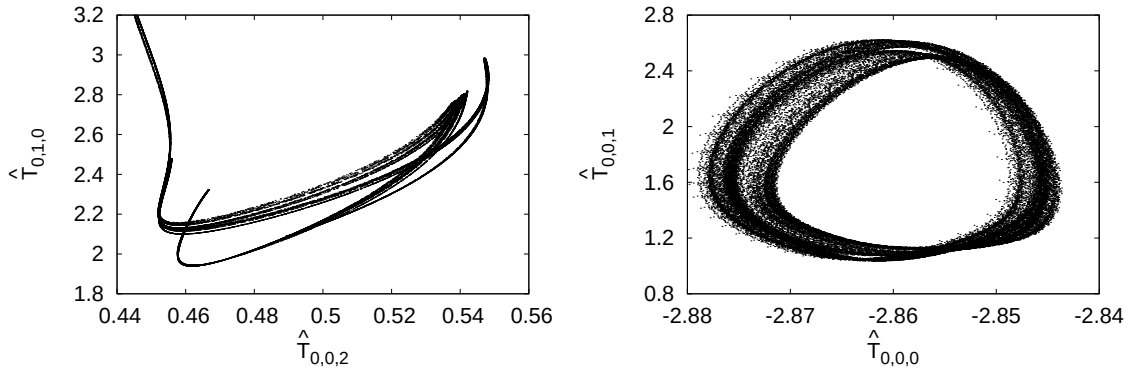

Figure 1.6. Left: A Hénon-like strange attractor which appears after a period doubling cascade of the AMO mode ($\Delta = 24°$C, $\gamma = 0.998$). Right: A quasi-periodic Hénon-like strange attractor which appears after a sequence of doublings of an invariant circle ($\Delta = 24°$C, $\gamma = 0.997185$).

Sacker bifurcation, which gives birth to a 2-torus attractor. The dynamics on the 2-torus attractor corresponds to the annual cycle imposed on the original AMO signal, see Figure 1.5. Clearly, the peak-to-peak amplitude of the quasi-periodic signal is larger than that of the original periodic signal, which shows that periodic forcing amplifies the AMO. The AMO mode is, however, not excited since the HNS bifurcation occurs for almost the same value of γ for which the Hopf bifurcation occurs in the autonomous system.

We study the dynamics of the nonautonomous system by means of a Poincaré stroboscopic map. In particular, the period doubling bifurcations of the autonomous system become doublings of an invariant circle of the Poincaré map. For $\Delta = 24°$C we detected at least 11 doublings, and we conjecture that a full cascade takes place. After these doublings we find quasi-periodic Hénon-like strange attractors, see Figure 1.6 (right panel). These attractors are the closure of the unstable manifold of a saddle invariant circle. Similar attractors were detected in the Lorenz-84 atmospheric model with seasonal forcing studied by Broer, Simó and Vitolo (2002, 2005).

1.4 Excitation of the AMO

Prescribed heat flux in ocean models is a strong idealisation since it amounts to net zero atmospheric damping. In reality sea surface temperature anomalies are substantially damped by the atmosphere. Dijkstra et al. (2008) estimate that realistic

values of γ are less than $\gamma_H \approx 0.951$, which implies that AMO mode is damped. The central question of Chapter 4 is:

> Can atmospheric low-frequency variability excite a weakly damped AMO mode?

Here, weakly damped refers to the parameter range $\gamma < \gamma_H$, but for values of γ not too far away from the Hopf bifurcation. We speak of excitation when multidecadal variability related to the AMO mode occurs in this parameter range.

The results of Chapter 3 show that annual atmospheric forcing increases the amplitude of the AMO in supercritical conditions. But since there is no decrease

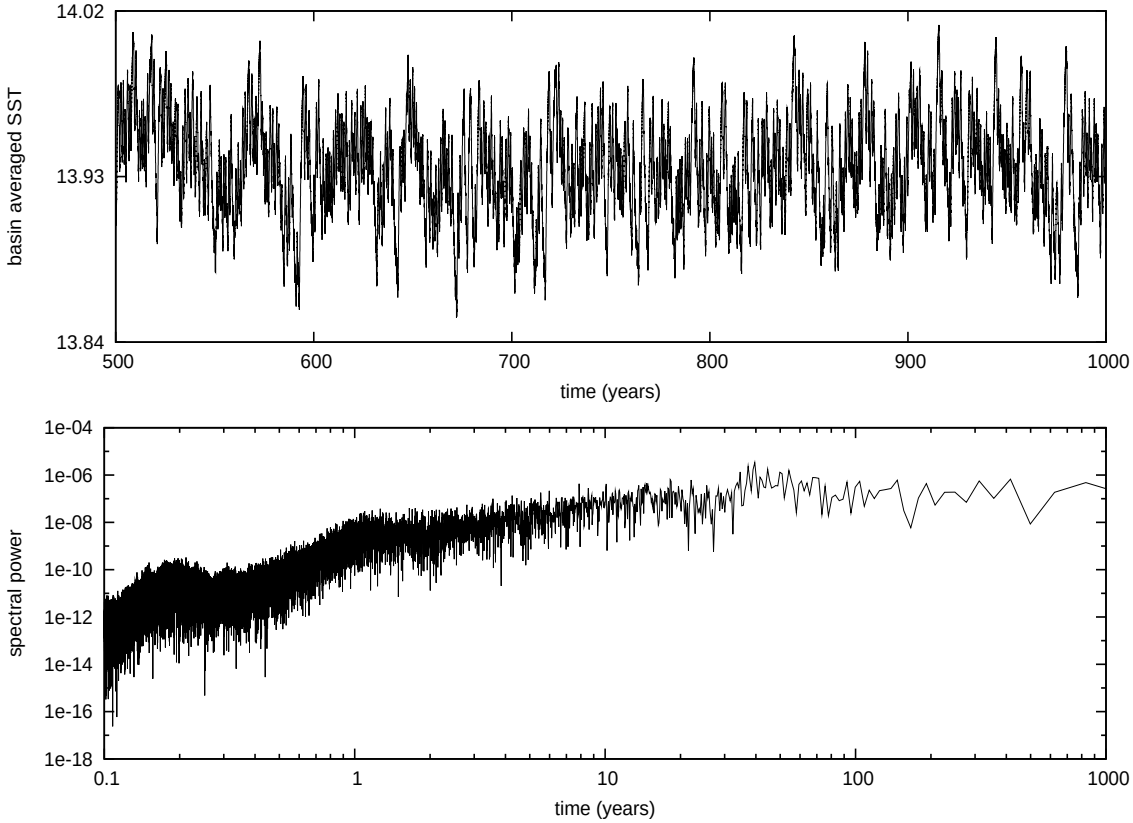

Figure 1.7. Induced multidecadal variability for $\Delta = 20°\text{C}$ and $\gamma = 0.90$. For these parameter values the autonomous ocean model of Chapter 3 has a stable equilibrium representing a steady ocean flow. With additional irregular forcing obtained from the atmosphere model in Chapter 2 multidecadal variability does occur. Top: basin averaged sea surface temperature as a function of time. Bottom: power spectrum.

of the critical value of γ, we cannot speak of excitation. On the other hand, we know that the atmosphere itself exhibits variability on a multitude of time scales. In Chapter 4 we study the low-order ocean model of Chapter 3 with additional forcing from the low-order atmosphere model of Chapter 2. The resulting model should not be considered as a coupled ocean-atmosphere model, but rather as an ocean model with additional atmospheric forcing.

With chaotic atmospheric forcing, the AMO is indeed excited. Figure 1.7 shows the basin averaged sea surface temperature when $\Delta = 20°\text{C}$ and $\gamma = 0.9$. The time series shows high-frequency fluctuations which are due to the fast variability of the atmosphere, but one can also observe a slower time scale. This is confirmed by the power spectrum, which shows a maximum for multidecadal time scales.

Invariant objects of the autonomous ocean model (equilibria, periodic orbits) no longer exist when chaotic atmospheric forcing is applied. Instead, the chaotic atmospheric forcing causes high-frequency, irregular fluctuations in the state variables of the ocean model. Nevertheless, the 'ghost' of the formerly existing nearby Hopf bifurcation still influences the dynamics. Such behaviour is typical for scenarios involving intermittency. In Chapter 4 we give a preliminary interpretation of this phenomenon. A more precise explanation is the subject of future research.

1.5 Discussion

The results presented in this work provide ample motivation for a further investigation of both mathematical and physical topics.

Persistence of dynamical phenomena? Reduction of infinite-dimensional systems to finite-dimensional systems is a challenging problem. On the one hand there are computational procedures such as discretisation by means of finite-differences or Galerkin-like projections. On the other hand there exist conceptual reductions to lower-dimensional models such as restrictions to invariant manifolds containing attractors. However, often the available theorems are not constructive. The challenge lies in reconciling the computational methods with the conceptual methods. The present study is only a first step in the coherent analysis of the infinite-dimensional models under consideration. There are two important open questions:

1. Which dynamical features of the low-order model persist as the number of retained basis functions is increased in the Galerkin projection?

2. Which dynamical features of the low-order models persist in the infinite-dimensional systems?

For the former question, one can think of the approach used for a Rayleigh-Bénard convection problem in Puigjaner et al. (2004, 2006, 2008).

The persistence question is also relevant from a physical point of view. Higher-dimensional Galerkin projections can describe phenomena with a smaller spatial scale, and the interaction between phenomena with different spatial scales likely affects the global dynamics. Therefore, an important question is:

> How can one objectively compare the dynamics of a low-dimensional model with the dynamics of higher-dimensional models?

Related to this question is how to compare the dynamics of low-order models with observations.

Existence of global attractors or inertial manifolds? Apart from the computational approach, a rigorous mathematical investigation of the infinite-dimensional systems should be undertaken. Indeed, in the present study the notion 'infinite-dimensional dynamical system' has been used in a rather loose sense. An important open question is:

> What is the state space of the infinite-dimensional model generated by the partial differential equations of Chapters 2 and 3?

Answering this question requires proving the existence of (weak) solutions. The idea would be to follow the methods used for the 2-dimensional Navier-Stokes equations and certain reaction-diffusion equations, see Temam (1997) and Robinson (2001). For these equations the Galerkin method is used to construct a sequence of successive approximations which converge to a solution of the weak form of the equations in a suitable Hilbert space. This Hilbert space then serves as a suitable state space on which an evolution operator can be defined. When this has been achieved one can try to prove the existence of finite-dimensional global attractors inside inertial manifolds.

Bibliography for Chapter 1

Benzi, R. and Speranza, A. (1989), Statistical properties of low frequency variability in the Northern Hemisphere, *Journal of Climate* **2**, pp. 367–379.

Broer, H.W., Simó, C. and Vitolo, R. (2002), Bifurcations and strange attractors in the Lorenz-84 climate model with seasonal forcing, *Nonlinearity* **15**, pp. 1205–1267.

Broer, H.W., Simó, C. and Vitolo, R. (2005), Quasi-periodic Hénon-like attractors in the Lorenz-84 climate model with seasonal forcing, *in* F. Dumortier, H.W. Broer, J. Mahwin, A. Vanderbauwhede and S.M. Verduyn-Lunel (eds), *Equadiff 2003, Proceedings International Conference on Differential Equations, Hasselt 2003*, World Scientific, pp. 714–719.

Broer, H.W. and Takens, F. (2010), *Dynamical Systems and Chaos*, Vol. 172 of *Applied Mathematical Sciences*, Springer.

Broer, H.W. and Vegter, G. (1984), Subordinate Šil'nikov bifurcations near some singularities of vector fields having low codimension, *Ergodic Theory and Dynamical Systems* **4**, pp. 509–525.

Broer, H.W. and Vitolo, R. (2008), Dynamical systems modelling of low-frequency variability in low-order atmospheric models, *Discrete and Continuous Dynamical Systems B* **10**, pp. 401–419.

Charney, J.G. and DeVore, J.G. (1979), Multiple Flow Equilibria in the Atmosphere and Blocking, *Journal of the Atmospheric Sciences* **36**, pp. 1205–1216.

Crommelin, D.T., Opsteegh, J.D. and Verhulst, F. (2004), A Mechanism for Atmospheric Regime Behavior, *Journal of the Atmospheric Sciences* **61**, pp. 1406–1419.

Dijkstra, H.A. (2005), *Nonlinear Physical Oceanography: A Dynamical Systems Approach to the Large Scale Ocean Circulation and El Niño*, second edn, Springer.

Dijkstra, H.A., Frankcombe, L.M. and von der Heydt, A.S. (2008), A Stochastic Dynamical Systems View of the Atlantic Multidecadal Oscillation, *Philosophical Transactions of the Royal Society A* **366**, pp. 2545–2560.

Fraedrich, K. and Böttger, H. (1978), A Wavenumber-Frequency Analysis of the 500 mb Geopotential at 50°N, *Journal of the Atmospheric Sciences* **35**, pp. 745–750.

Kushnir, Y. (1994), Interdecadal Variations in North Atlantic Sea Surface Temperature and Associated Atmospheric Conditions, *Journal of Climate* **7**, pp. 141–157.

Kwasniok, F. (1996), The reduction of complex dynamical systems using principal interaction patterns, *Physica D* **92**, pp. 28–60.

Latif, M. (1998), Dynamics of Interdecadal Variability in Coupled Ocean–Atmosphere Models, *Journal of Climate* **11**, pp. 602–624.

Puigjaner, D., Herrero, J., Giralt, F. and Simó, C. (2004), Stability analysis of the flow in a cubical cavity heated from below, *Physics of Fluids* **16**, pp. 3639–3655.

Puigjaner, D., Herrero, J., Giralt, F. and Simó, C. (2006), Bifurcation analysis of multiple steady flow patterns for Rayleigh-Bénard convection in a cubical cavity at $Pr = 130$, *Physical Review E* **73**. 046304.

Puigjaner, D., Herrero, J., Simó, C. and Giralt, F. (2008), Bifurcation analysis of steady Rayleigh–Bénard convection in a cubical cavity with conducting sidewalls, *Journal of Fluid Mechanics* **598**, pp. 393–427.

Robinson, J.C. (2001), *Infinite-Dimensional Dynamical Systems*, Cambridge University Press.

Ruelle, D. and Takens, F. (1971), On the nature of turbulence, *Communications in Mathematical Physics* **20**, pp. 167–192.

Selten, F.M. (1995), An efficient description of the dynamics of barotropic flow, *Journal of the Atmospheric Sciences* **52**, pp. 915–936.

Te Raa, L.A. and Dijkstra, H.A. (2002), Instability of the Thermohaline Ocean Circulation on Interdecadal Timescales, *Journal of Physical Oceanography* **32**, pp. 138–160.

Temam, R. (1997), *Infinite-Dimensional Dynamical Systems in Mechanics and Physics*, Vol. 68 of *Applied Mathematical Sciences*, second edn, Springer.

van der Vaart, P.C.F., Schuttelaars, H.M., Calvete, D. and Dijkstra, H.A. (2002), Instability of time-dependent wind-driven ocean gyres, *Physics of Fluids* **14**, pp. 3601–3615.

Chapter 2

Atmospheric low-frequency variability

2.1 Introduction

The atmosphere shows variability on a wide range of time and spatial scales. In this chapter we study the dynamics of atmospheric low-frequency variability as observed at midlatitudes in northern hemisphere winters. In Chapter 4 we investigate its potential role in the excitation of the Atlantic Multidecadal Oscillation.

2.1.1 Statement of the problem

A classical problem in the theory of General Atmospheric Circulation is the characterisation of the recurrent flow patterns observed at midlatitudes in northern hemisphere winters (Dole, 1983). This issue has been subject of much scientific attention at least since Baur's definition of *Grosswetterlagen* (Baur, 1951), or Rex's description of Atlantic blocking (Rex, 1950). One of the motivations for the interest is the potential importance of this problem to understand persistence and predictability of atmospheric motion beyond the time scales of baroclinic synoptic disturbances (2 to 5 days). Indeed, it is expected that insight in the nature of *low-frequency regime dynamics* will lead to significant progress in the so-called extended range weather forecasting (Reinhold, 1987). At the same time, the problem is of great relevance in climate science, since it has been proposed that climate change predominantly manifests itself through changes in the atmospheric circulation regimes, that is 'changes in the probability distribution function of the climate attractor' (Corti et al., 1999). As a matter of fact, misrepresentation of the statistics of blocking and planetary waves is widespread in climate models (Palmer et al., 2008; Lucarini, Calmanti, Dell'Aquila, Ruti and Speranza, 2007): this may have a profound impact on the ability of such models to reproduce both current climate and climate change.

There are various approaches to the problem of low-frequency atmospheric variability and they are not equivalent—though not independent of each other. An old theory associates recurrent large-scale flow patterns with stationary states of the atmospheric circulation, which correspond to equilibria in the dynamical equations of atmospheric motion. Small-scale weather acts then as a random perturbation inducing fluctuations around equilibria and transitions between states. This mechanism would be responsible for the existence of multimodal statistics in observed data, like the bimodal distribution of planetary activity on zonal wave numbers 2, 3, and 4 found by Hansen and Sutera (1986).

Orographic resonance theories lend support to the hypothesis that activity of planetary waves possesses a multimodal distribution (Benzi, Speranza and Sutera, 1986). A seminal paper in this direction was that by Charney and DeVore (1979): they proposed that the interaction between zonal flow and wave field via form-drag causes the occurrence of two equilibria for the amplitude of planetary waves. This idea was further elaborated by Legras and Ghil (1985) who found intermittent transitions between multiple equilibria representing blocked and zonal flows. Crommelin (2002, 2003) and Crommelin et al. (2004) explain the transitions in terms of homo- and heteroclinic dynamics near equilibria corresponding to distinct preferred flow patterns. More recent developments aimed at theories allowing for multiple stable equilibria at the same zonal wind speed, in such a way that the amplitudes of the corresponding ultra long (planetary scale) waves differ by values of the order of 100 m of geopotential height (Malguzzi et al., 1996).

Despite this remarkable research effort, the scientific debate is still very much open on whether a single equilibrium/mode (Ambaum, 2008; Nitsche et al., 1994; Stephenson et al., 2004) or multiple equilibria/modes (Benzi and Speranza, 1989; Charney and DeVore, 1979; Hansen and Sutera, 1995; Mo and Ghil, 1988; Ruti et al., 2006) characterise the large-scale atmospheric circulation.

Spectral analysis is an alternative way of characterising low-frequency atmospheric variability. Examination of the so-called Hayashi spatio-temporal spectra show that the low-frequency component of the variance of the 500 mb geopotential heights is concentrated in the region of periods larger than 10 days and zonal wave numbers less than 5 (Fraedrich and Böttger, 1978). Benzi and Speranza (1989) reexamine previous studies of amplification of waves with zonal wave number 3 (Itoh, 1983) and of onset of Pacific anomalies (Dole, 1986). They summarise the main physical features of low-frequency atmospheric variability:

- it is on average almost totally non-propagating; planetary waves show a slight tendency to propagate westwards for wave numbers 1-2 and eastwards for wave number 4;

- it seems related to ultra long wave amplification through a non-standard form of baroclinic instability in which orography plays an essential role;

- it is characterised by vertical coherence of the anomalies, see, e.g., Dole (1986, Figures 9 and 10).

Hansen and Sutera (1986) hypothesise a baroclinic conversion process balancing dissipation at wave numbers 2, 3, and 4, which is not associated to the ordinary baroclinic instability, given the equivalent barotropic nature of the difference fields between the two modes of their wave indicator. It has been known since Charney and Eliassen (1949) that the interaction between eddy field and orography on planetary scales is characterised by a non-propagating amplification of the eddy field: this is one of the common features observed in many studies of transitions between regimes (see e.g. Malguzzi et al. (1997) and references therein).

The central question debated here is: does the atmospheric variability characterising the northern hemisphere midlatitude circulation result from dynamical processes specific to the interaction of zonal flow and planetary waves with orography, and what are these processes?

2.1.2 Our approach

We derive a 'minimal model' for the midlatitude atmospheric circulation, containing the essential 'ingredients' to capture the basic features of low-frequency variability: zonal flow, a large-scale planetary wave, orography, and a baroclinic-like forcing. The model is obtained by Galerkin projection of the two-layer shallow-water equations onto a small number of spatial modes: in the zonal direction we select wave numbers $m = 0$ (for the zonal flow) and $m = 3$ (for the large-scale wave). We choose the latter because it is where the maximum of the low-frequency stationary variance is attained, see e.g., Fraedrich and Böttger (1978, Figure 2). We retain wave numbers $0, 1, 2$ in the meridional direction. The basic idea is to search for dynamical processes inherent to the largest spatial scales, using a conceptual model which is sufficiently simple for this purpose. We do not aim at a realistic representation of atmospheric motion, although our modelling approach is motivated by the observational evidence discussed in the previous section. We return to this point at the end of §2.4.

The full shallow-water equations are a system of 6 partial differential equations for the horizontal velocity field u_ℓ, v_ℓ and thickness h_ℓ for $\ell = 1, 2$. Forcing is modelled as relaxation to an apparent westerly wind and orography is included in the bottom layer. Orography height and the forcing zonal wind strength are controlled by parameters h_0 and U_0 respectively. Working with a shallow-water model, instead

of the more traditional quasi-geostrophic models, offers the advantage that physically relevant values can be used for h_0: this parameter is bound to be small in the quasi-geostrophic models traditionally used to study low-frequency variability, due to the perturbative nature of orography in quasi-geostrophic theory (Bannon, 1983).

2.1.3 Summary of the results

The major achievement in this work is to propose a characterisation of low-frequency atmospheric behaviour in terms of intermittency due to bifurcations of waves. Non-propagating planetary waves arise in our model from the interaction of zonal flow with orography. The waves are associated to mixed baroclinic/barotropic instabilities, where the baroclinicity is not that associated to midlatitude synoptic systems (indeed, wave number 3 is not the most unstable baroclinic mode). Rather, instabilities here bear resemblance to the orographic baroclinic instability (see Cessi and Speranza (1985) and references therein).

Low-frequency behaviour with the appropriate time scales (10-200 days, where the lower frequency components of 60-200 days can be interpreted as harmonics of the higher frequency components of 10-60 days) is exhibited by our 'minimal model' for physically relevant values of the parameters ($U_0 \approx 15$ m/s and $h_0 \approx 1000$ m). Here, the dynamics of our minimal model takes place on strange attractors which are formed through sequences of bifurcations of periodic orbits (waves) as the forcing wind speed U_0 increases.

The model dynamics is stationary for $U_0 \leq 12.2$ m/s due to the presence of a stable equilibrium corresponding to a steady westerly wind. This steady flow becomes unstable through Hopf bifurcations (associated with mixed baroclinic/barotropic instabilities) as the forcing U_0 increases. This gives rise to two types of stable waves: for lower orography (about 800 m), the period is about 10 days and there is eastward propagation in the bottom layer; for more pronounced orography, the period is longer (30-60 days) and the waves are non-propagating. These waves remain stable in relatively large parameter domains and bifurcate into strange attractors through a number of scenarios (see below) in the parameter quadrant $U_0 \geq 14.5$ m/s and $h_0 \geq 850$ m. The dynamics on these strange attractors is associated with irregularly recurring vorticity patterns, which are inherited from the periodic orbit that gives birth to the strange attractor.

The Lyapunov diagram (top panel of Figure 2.1) shows a classification of the dynamical behaviour in the different regions of the (U_0, h_0)-plane. Bifurcations of equilibria and periodic orbits (bottom panel) explain the main features of the Lyapunov diagram (see Appendix B for the algorithms). The two Hopf curves $H_{1,2}$ give

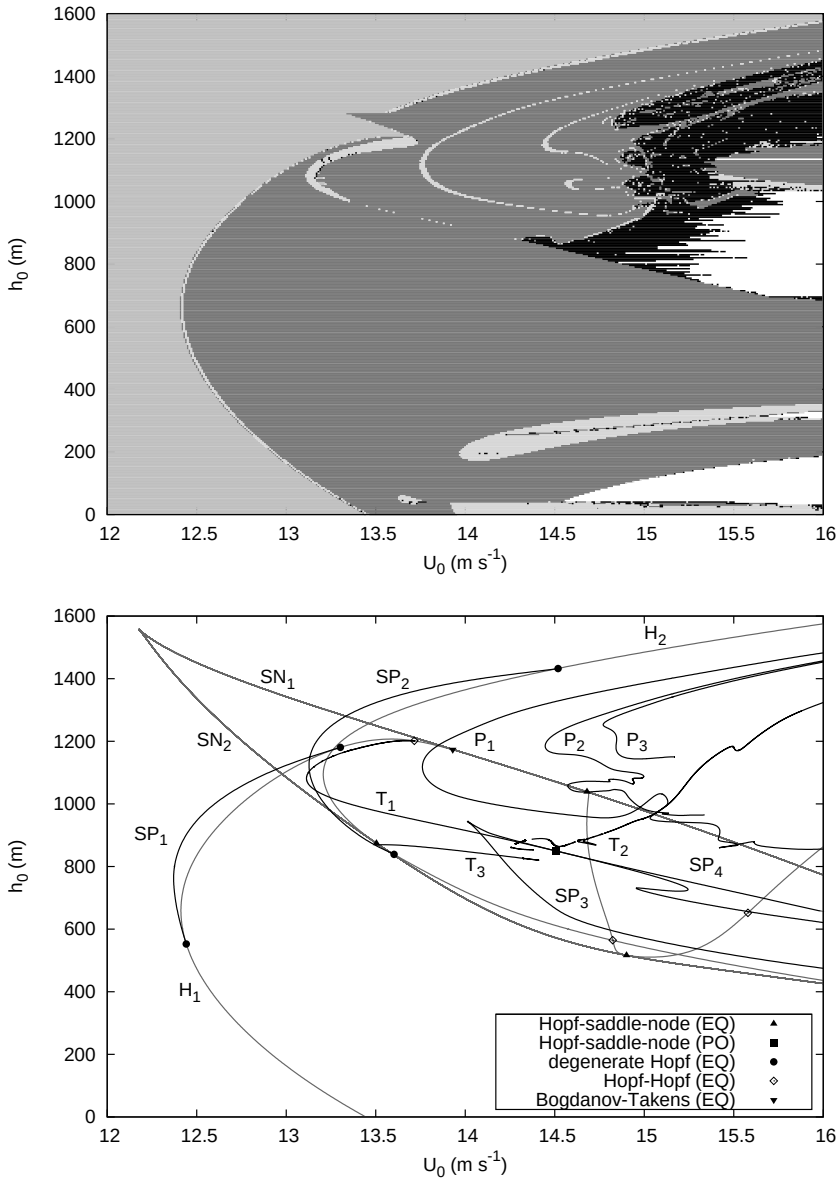

Figure 2.1. Organisation of the (U_0, h_0) parameter plane of the low-order model. Top: Lyapunov diagram for the attractors of the system. Bottom: bifurcation diagram of attractors, same parameter window as above. The marked locations are codimension-2 bifurcations. See Table 2.1 for the grey tone coding; see Appendix B for the algorithms.

Colour	Lyapunov exponents	Attractor type
grey 2	$0 > \lambda_1 \geq \lambda_2 \geq \lambda_3$	equilibrium
grey 3	$\lambda_1 = 0 > \lambda_2 \geq \lambda_3$	periodic orbit
grey 1	$\lambda_1 = \lambda_2 = 0 > \lambda_3$	2-torus
black	$\lambda_1 > 0 \geq \lambda_2 \geq \lambda_3$	strange attractor
white		escaping orbit
Colour	Bifurcation type	Bifurcating attractor
grey	saddle-node and Hopf	equilibrium
black	period doubling, Hopf-Neĭmark-Sacker, and saddle-node	periodic orbit

Table 2.1. Grey scale coding for the Lyapunov diagram and bifurcation diagram in Figure 2.1.

birth to stable periodic orbits. In turn, these periodic orbits bifurcate into strange attractors through three main routes to chaos:

- period doubling cascade of periodic orbits (the curves $P_{1,2,3}$);
- Hopf-Neĭmark-Sacker bifurcation of periodic orbits (the curve T_2), followed by the breakdown of a 2-torus;
- saddle-node bifurcation of periodic orbits taking place on a strange attractor (the curve SP_4), the so-called intermittency route (Pomeau and Manneville, 1980).

Similar routes have been described in many studies of low-order atmospheric models (Broer et al., 2002; Legras and Ghil, 1985; Lucarini, Speranza and Vitolo, 2007; De Swart, 1989; Van Veen, 2003). We here establish a new link between intermittency due to nonlinear instability of waves and low-frequency variability.

This chapter is structured as follows. In §2.2.1 we present the derivation of the low-order model from the 2-layer shallow-water equations. The bifurcation diagram of the low-order model is discussed in §2.3.1, followed by analysis of the routes to chaos in §2.3.2. In §2.3.3 we explain the model phenomenology in terms of mathematical concepts (bifurcations, intermittency) and §2.3.4 provides a physical interpretation. Finally, in §2.4 our results are discussed in the context of the literature.

2.2 Model

We consider atmospheric flow in two layers. In each layer the velocity field (u, v) is 2-dimensional. The thickness h of each layer is variable, which is the only 3-dimensional aspect of this model. The governing equations are given by a system of six partial differential equations. By means of truncated Fourier expansions and a Galerkin projection we obtain a low-order model which consists of a 46-dimensional system of ordinary differential equations.

2.2.1 The 2-layer shallow-water equations

The constants H_1 and H_2 denote the mean thickness of each layer, and the fields η_1' and η_2' denote deviations from the mean thickness, where primes indicate that the variable is dimensional. The thickness fields of the two layers are given by

$$\begin{aligned} h_1' &= H_1 + \eta_1' - \eta_2', && (2.1)\\ h_2' &= H_2 + \eta_2' - h_b', && (2.2) \end{aligned}$$

where h_b denotes the bottom topography profile; see Figure 2.2. The pressure fields are related to the thickness fields by means of the hydrostatic relation

$$\begin{aligned} p_1' &= \rho_1 g(h_1' + h_2' + h_b'), && (2.3)\\ p_2' &= \rho_1 g h_1' + \rho_2 g(h_2' + h_b'), && (2.4) \end{aligned}$$

where the constants ρ_1 and ρ_2 denote the density of each layer.

The governing equations are nondimensionalised using scales L, U, L/U, D, and $\rho_0 U^2$ for length, velocity, time, depth, and pressure, respectively, and are given by

$$\begin{aligned} \frac{\partial u_\ell}{\partial t} + u_\ell \frac{\partial u_\ell}{\partial x} + v_\ell \frac{\partial u_\ell}{\partial y} &= -\frac{\partial p_\ell}{\partial x} + (Ro^{-1} + \beta y) v_\ell \\ &\quad - \sigma\mu(u_\ell - u_\ell^*) + Ro^{-1} E_H \left(\frac{\partial^2 u_\ell}{\partial x^2} + \frac{\partial^2 u_\ell}{\partial y^2} \right) - \sigma r \delta_{\ell,2} u_\ell \\ \frac{\partial v_\ell}{\partial t} + u_\ell \frac{\partial v_\ell}{\partial x} + v_\ell \frac{\partial v_\ell}{\partial y} &= -\frac{\partial p_\ell}{\partial y} - (Ro^{-1} + \beta y) u_\ell \\ &\quad - \sigma\mu(v_\ell - v_\ell^*) + Ro^{-1} E_H \left(\frac{\partial^2 v_\ell}{\partial x^2} + \frac{\partial^2 v_\ell}{\partial y^2} \right) - \sigma r \delta_{\ell,2} v_\ell \\ \frac{\partial h_\ell}{\partial t} + u_\ell \frac{\partial h_\ell}{\partial x} + v_\ell \frac{\partial h_\ell}{\partial y} &= -h_\ell \left(\frac{\partial u_\ell}{\partial x} + \frac{\partial v_\ell}{\partial y} \right) \end{aligned} \qquad (2.5)$$

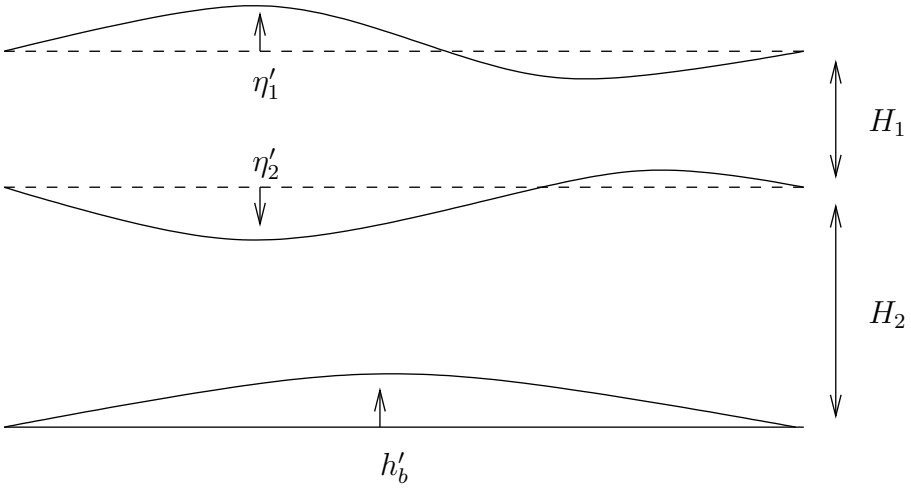

Figure 2.2. Layers in the shallow-water model.

where u_ℓ and v_ℓ are eastward and northward components of the 2-dimensional velocity field, respectively. In addition, the nondimensional pressure terms are given by

$$p_1 = \frac{\rho_1}{\rho_0} F(h_1 + h_2 + h_b),$$
$$p_2 = \frac{\rho_1}{\rho_0} F h_1 + \frac{\rho_2}{\rho_0} F(h_2 + h_b).$$

Several nondimensional numbers appear in the governing equations: the advective time scale σ, the nondimensional β-parameter, the Rossby number Ro, the horizontal Ekman number E_H, and the inverse Froude number F. These parameters have the following expressions in terms of the dimensional parameters:

$$\sigma = \frac{L}{U}, \quad \beta = \frac{\beta_0 L^2}{U}, \quad Ro = \frac{U}{f_0 L}, \quad E_H = \frac{A_H}{f_0 L^2}, \quad F = \frac{gD}{U^2}.$$

Standard values of the dimensional parameters are listed in Table 2.2.

The dynamical equations will be considered on the zonal β-plane channel

$$0 \le x \le L_x/L, \quad 0 \le y \le L_y/L.$$

Suitable boundary conditions have to be imposed: we require all fields to be periodic in the x-direction. At $y = 0, L_y/L$ we impose the conditions

$$\frac{\partial u_\ell}{\partial y} = \frac{\partial h_\ell}{\partial y} = v_\ell = 0.$$

Parameter		Value	
A_H	momentum diffusion coefficient	1.0×10^2	[m^2 s^{-1}]
μ	relaxation coefficient	1.0×10^{-6}	[s^{-1}]
r	linear friction coefficient	1.0×10^{-6}	[s^{-1}]
f_0	Coriolis parameter	1.0×10^{-4}	[s^{-1}]
β_0	planetary vorticity gradient	1.6×10^{-11}	[m^{-1} s^{-1}]
ρ_0	reference density	1.0	[kg m^{-3}]
ρ_1	density (top)	1.01	[kg m^{-3}]
ρ_2	density (bottom)	1.05	[kg m^{-3}]
g	gravitational acceleration	9.8	[m s^{-2}]
α_1	zonal velocity forcing strength (top)	1.0	[–]
α_2	zonal velocity forcing strength (bottom)	0.5	[–]
L_x	channel length	2.9×10^7	[m]
L_y	channel width	2.5×10^6	[m]
H_1	mean thickness (top)	5.0×10^3	[m]
H_2	mean thickness (bottom)	5.0×10^3	[m]
L	characteristic length scale	1.0×10^6	[m]
U	characteristic velocity scale	1.0×10^1	[m s^{-1}]
D	characteristic depth scale	1.0×10^3	[m]

Table 2.2. Standard values of the fixed parameters.

The model is forced by relaxation to an apparent westerly wind given by the profile

$$u_1^*(x,y) = \alpha_1 U_0 U^{-1}(1 - \cos(2\pi y L/L_y)), \quad v_1^*(x,y) = 0,$$
$$u_2^*(x,y) = \alpha_2 U_0 U^{-1}(1 - \cos(2\pi y L/L_y)), \quad v_2^*(x,y) = 0,$$

where the dimensional parameter U_0 controls the strength of the forcing and the nondimensional parameters α_1 and α_2 (Table 2.2) control the vertical shear of the forcing. For the bottom topography we choose a profile with zonal wave number 3:

$$h_b(x,y) = h_0 D^{-1}(1 + \cos(6\pi x L/L_x)),$$

where the dimensional parameter h_0 controls the amplitude of the topography. We require that the bottom topography is contained entirely in the bottom layer which implies the restriction $h_0 \leq H_2/2$.

2.2.2 The low-order model

The governing equations (2.5) form a dynamical system with an infinite-dimensional state space. We reduce the infinite-dimensional system to a system of finitely many

ordinary differential equations by means of a Galerkin projection. This amounts to an expansion of the unknown fields u_ℓ, v_ℓ, h_ℓ in terms of known basis functions, depending only on spatial variables, with unknown coefficients, depending only on time. An orthogonal projection onto the space spanned by the basis functions gives a set of finitely many ordinary differential equations for the expansion coefficients.

As basis functions we use Fourier modes with half wave numbers. For an integer $k \geq 0$ and a real number a these functions are given by

$$s_k(x;a) = \sqrt{\frac{2}{a}} \sin(k\pi x/a), \quad c_k(x;a) = \begin{cases} \sqrt{\frac{1}{a}} & \text{if } k = 0, \\ \sqrt{\frac{2}{a}} \cos(k\pi x/a) & \text{if } k \neq 0, \end{cases} \tag{2.6}$$

where $x \in [0, a]$, and the numerical factors serve as normalisation constants.

Deciding which Fourier modes to retain in the Galerkin projection is a non-trivial problem. *A priori* it is not known which choice captures the dynamics of the infinite-dimensional system in the best possible way. In Puigjaner et al. (2004, 2006, 2008) this problem has been addressed in the setting of a Rayleigh-Bénard convection problem by checking qualitative changes in dynamical behaviour and quantitative information on the location of branches of equilibria and their bifurcations, while increasing the number of retained modes. In this work we choose a different approach: first of all, we construct a minimal model, retaining only those Fourier modes which are essential to reproduce atmospheric low-frequency behaviour. Observational evidence (see §2.1.1) suggests that the fundamental physical processes involved in low-frequency behaviour manifest themselves at zonal wave numbers less than 5 (Benzi and Speranza, 1989). For the above reasons, we choose wave numbers $m = 0, 3$ in the zonal direction, and the wave numbers $n = 0, 1, 2$ in the meridional direction. Let

$$R = \{(0,0), (0,1), (0,2), (3,0), (3,1), (3,2)\}$$

denote the set of retained wave number pairs. Moreover, set $a = L_x/L$ and $b = L_y/L$. Then all nondimensional fields are expanded as

$$\begin{aligned} u_\ell(x,y,t) &= \sum_{(m,n)\in R} \left[\widehat{u}^c_{\ell,m,n}(t) c_{2m}(x;a) + \widehat{u}^s_{\ell,m,n}(t) s_{2m}(x;a)\right] c_n(y;b), \\ v_\ell(x,y,t) &= \sum_{(m,n)\in R} \left[\widehat{v}^c_{\ell,m,n}(t) c_{2m}(x;a) + \widehat{v}^s_{\ell,m,n}(t) s_{2m}(x;a)\right] s_n(y;b), \\ h_\ell(x,y,t) &= \sum_{(m,n)\in R} \left[\widehat{h}^c_{\ell,m,n}(t) c_{2m}(x;a) + \widehat{h}^s_{\ell,m,n}(t) s_{2m}(x;a)\right] c_n(y;b). \end{aligned}$$

In this way the truncated expansions satisfy the boundary conditions.

By substituting the truncated expansions in (2.5) and projecting (with respect to the standard inner product) the governing equations on the Fourier modes, we obtain a system of ordinary differential equations for the time-dependent Fourier coefficients. With the above choice of the retained wave numbers, we need 9, 6, and 9 coefficients for the fields u_ℓ, v_ℓ, and h_ℓ, respectively. However, due to conservation of mass, it turns out that the coefficients $\hat{h}_{\ell,0,0}$ are constant in time and therefore they can be treated as a constant. Hence, the low-order model is 46-dimensional. Formulas to compute the coefficients of the low-order model are presented in Appendix A.2.

2.3 Results

We here investigate the dynamics of the low-order model, starting from a description of the bifurcations in Figure 2.1 (§2.3.1). It is shown how low-frequency dynamical behaviour is linked to strange attractors, which occur in a relatively large parameter domain. The onset of chaotic dynamics is explained in terms of bifurcation scenarios ('routes to chaos,' §§2.3.2, 2.3.3). Lastly, physical interpretation of the dynamics is given in terms of atmospheric low-frequency variability (§2.3.4).

2.3.1 Organisation of the parameter plane

In this section we give a detailed description of the bifurcation diagram and we explain how this clarifies various parts of the Lyapunov diagram. The bifurcations detected in our model are standard, and they are discussed in detail in, e.g., Kuznetsov (2004).

Lyapunov diagram. The top panel of Figure 2.1 contains the Lyapunov diagram of the attractors of the low-order model. This is produced by scanning the (U_0, h_0)-parameter plane from left to right and classifying the detected attractor by means of Lyapunov exponents, see Appendix B.3.1 and Broer et al. (2008a,b) for details. Along each line of constant h_0 we start with a fixed initial condition when $U_0 = 12$ m/s. For the next parameter values on this line we take the last point of the previous attractor as an initial condition for the next one.

We do not exclude the possibility of coexisting attractors, but this can not be detected by our procedure. More refined procedures, with varying initial conditions, detect coexistence of attractors as well. For large values of the parameter U_0 orbits can escape to infinity (see the white parts in Figure 2.1), but this also depends on the

chosen initial condition. These unbounded orbits also appear in a low-order model of Lorenz (1980).

Bifurcations of equilibria. The transition from stationary to periodic behaviour in the Lyapunov diagram (Figure 2.1) is explained by Hopf bifurcations where an equilibrium loses stability. Bifurcations are computed here with the AUTO–07p software (Doedel and Oldeman, 2007). A stable equilibrium is found for $U_0 = 0$ m/s and remains stable up to $U_0 = 12.2$ m/s. The equilibrium undergoes one or more Hopf bifurcations for $U_0 > 12.2$ m/s approximately: loss of stability occurs at curves H_1 and H_2 in Figure 2.1 (we only focus on bifurcations leading to loss of stability here). Periodic orbits born at the H_1 curve have periods of about 10 days, whereas periodic orbits born at the H_2 curve have periods in the range of 30-60 days; see Figure 2.3 and Figure 2.4, respectively.[1]

A pair of degenerate Hopf points occurs at the tangencies between the Hopf curves $H_{1,2}$ and the curves SP_1 and SP_2 of saddle-node bifurcations of periodic orbits. The bifurcation type on $H_{1,2}$ changes from supercritical to subcritical at the degenerate Hopf points. Two branches of stable periodic orbits are thus formed on either of $SP_{1,2}$ or $H_{1,2}$.

Two curves SN_1 and SN_2 of saddle-node bifurcations of equilibria meet in a cusp. This leads to a domain in the parameter plane for which three equilibria coexist. The boundaries of this domain are tangent to the Hopf curves H_1 and H_2 at three different Hopf-saddle-node bifurcation points. Moreover, a Bogdanov-Takens point occurs along one of the saddle-node curves, where one additional real eigenvalue crosses the imaginary axis.

Bifurcations of periodic orbits born at H_1 or SP_1. The periodic orbits born at the curves H_1 or SP_1 lose stability through either Hopf-Neĭmark-Sacker or saddle-node bifurcations. The Hopf-Neĭmark-Sacker curve T_1 originates from a Hopf-Hopf point at the curve H_1, where two pairs of complex eigenvalues cross the imaginary axis. The saddle-node curves $SP_{3,4}$ are joined in a cusp, and the curve SP_4 forms part of a boundary between periodic and chaotic behaviour in the Lyapunov diagram. Moreover, the curve SP_4 becomes tangent to the Hopf-Neĭmark-Sacker curve T_1 at a Hopf-saddle-node bifurcation point of periodic orbits.

[1] Unless specified otherwise, attractors are plotted on directions of maximal amplitude. See Appendix B.3.1 for details. Since the projection is computed numerically, labels for the axes are omitted.

Bifurcations of periodic orbits born at H_2 or SP_2. The periodic orbits born at the curves H_2 or SP_2 may lose stability through either a period doubling bifurcation or Hopf-Neĭmark-Sacker bifurcations. The former occurs on curve P_1, which is the first of a cascade leading to a chaotic attractor, see the next section. Hopf-Neĭmark-Sacker bifurcations occur on curves T_2 and T_3 in Figure 2.1: T_2 is tangent to the period doubling curve P_1 at a 1:2-resonance point, and T_3 originates from a Hopf-saddle-node bifurcation point of periodic orbits.

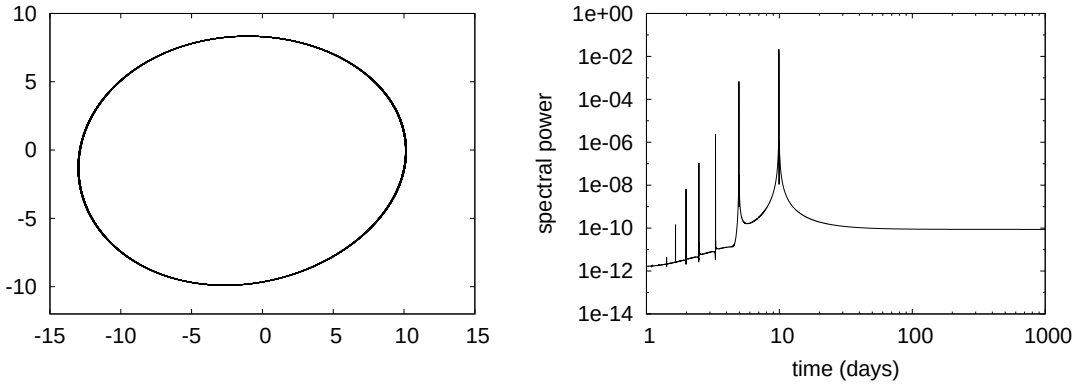

Figure 2.3. Periodic orbit born at Hopf bifurcation H_1 ($U_0 = 13.32$ m/s, $h_0 = 800$ m) and its power spectrum. The period is approximately 10 days.

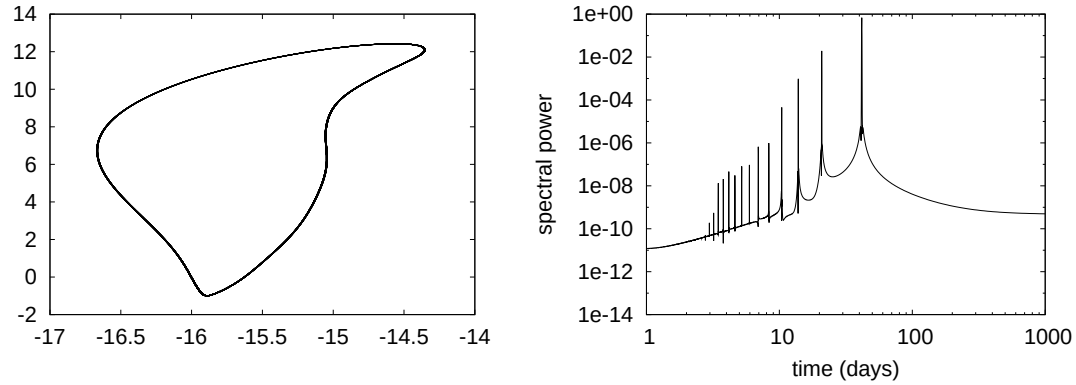

Figure 2.4. Periodic orbit born at Hopf bifurcation H_2 ($U_0 = 14.64$ m/s, $h_0 = 1400$ m) and its power spectrum. The period is approximately 60 days.

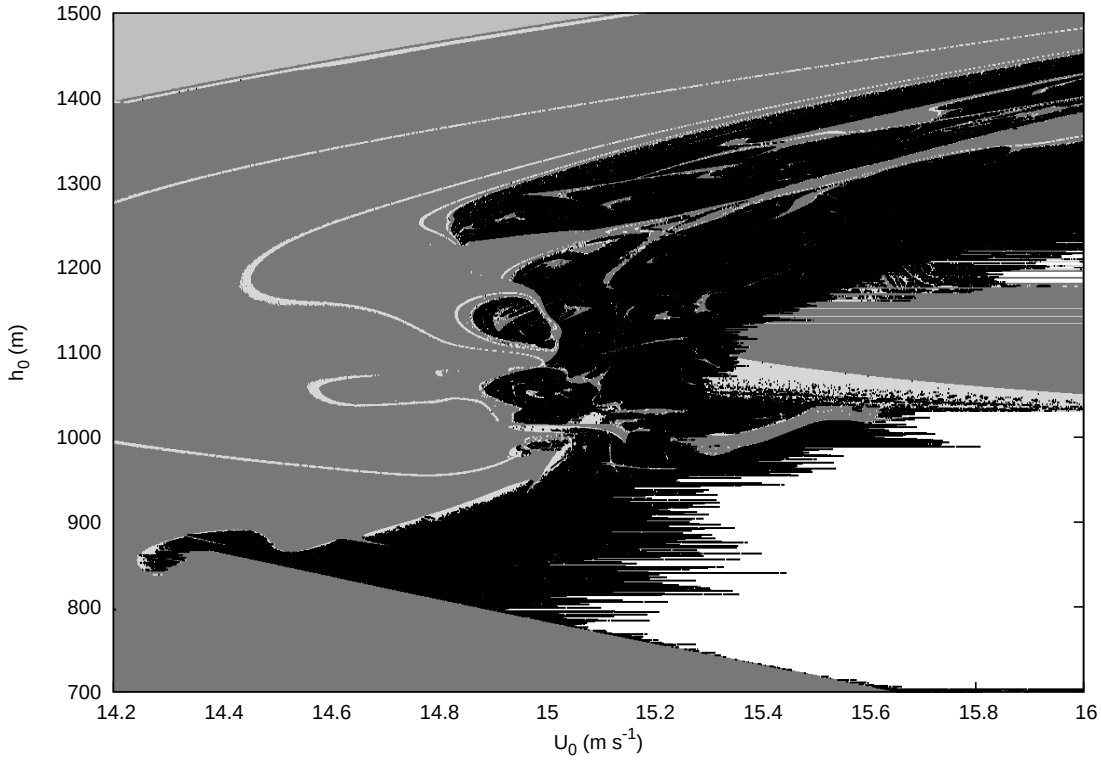

Figure 2.5. Magnification of the Lyapunov diagram in Figure 2.1; see Table 2.1 for the grey tone coding.

2.3.2 Routes to chaos

We have identified three different routes from orderly to chaotic behaviour. All of them involve one or more bifurcations of the stable periodic orbits described in the previous section.

Period doublings. The periodic orbits born at the Hopf bifurcation H_2 lose stability through a period doubling bifurcation (see previous section). Three period doubling curves $P_{1,2,3}$ are shown in Figure 2.1, and we expect that they are the first of an infinite cascade. Indeed, a magnification of the Lyapunov diagram (Figure 2.5) reveals a large chaotic region at the right of P_3, interrupted by narrow domains of periodic behaviour. Occurrence of these windows of periodicity is confirmed in the diagrams in Figure 2.6. However, these gaps disappear for lower values of the parameter h_0, and chaotic behaviour seems to be persistent on a continuum.

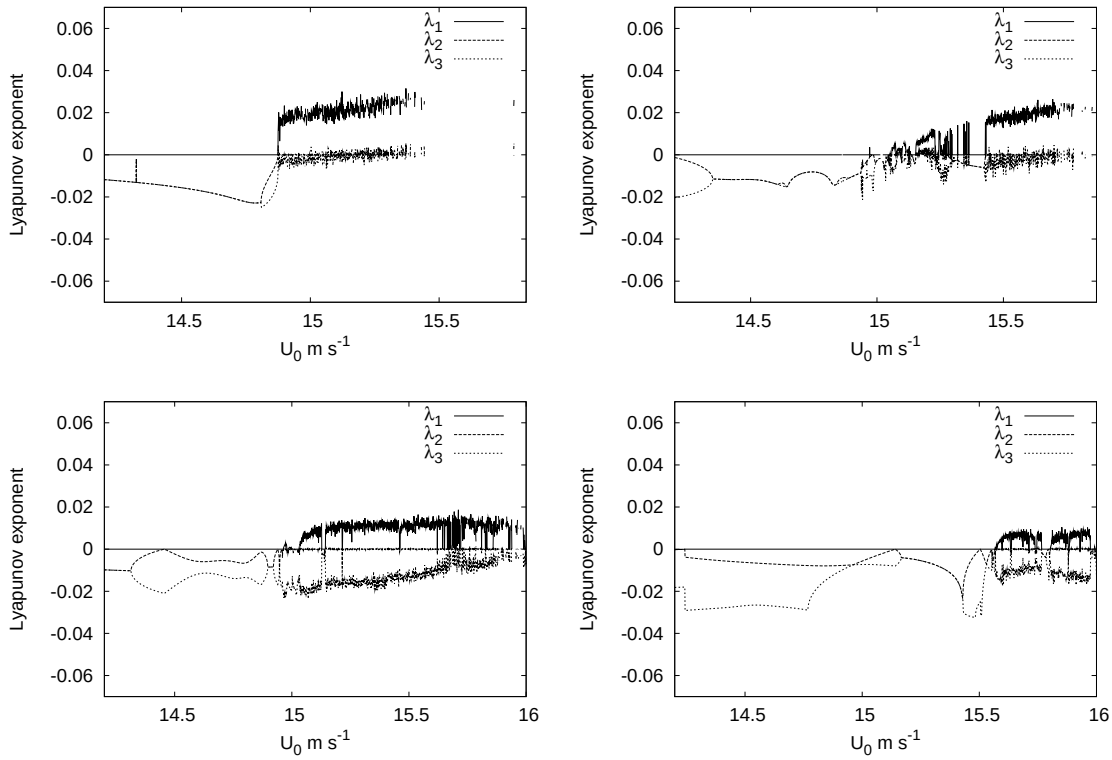

Figure 2.6. The three largest Lyapunov exponents $\lambda_1 \geq \lambda_2 \geq \lambda_3$ (non-dimensional) as a function of U_0. The value of the parameter h_0 is fixed at $h_0 = 800$ m (top left), $h_0 = 1000$ m (top right), $h_0 = 1200$ m (bottom left), and $h_0 = 1400$ m (bottom right).

Figure 2.7 shows a twice-doubled stable periodic orbit along the cascade and a strange attractor after the end of the cascade. The dynamics on the strange attractor exhibits low-frequency behaviour in the range 20-200 days (see the power spectrum in Figure 2.7). The peaks around 100 and 200 days are 'inherited' from the twice-doubled periodic orbit. In turn, these originate from the same branch of periodic orbits as in Figure 2.4: just before the first period doubling bifurcation P_1 ($U_0 = 13.9$ m/s, $h_0 = 1200$ m) this stable periodic orbit has a period of approximately 50 days (not shown).

Broken torus. Two-torus attractors occur in a narrow region separating periodic from chaotic behaviour in the Lyapunov diagram (Figure 2.5). The 2-torus attractors branch off from periodic orbits at the Hopf-Neĭmark-Sacker bifurcations on curve T_2.

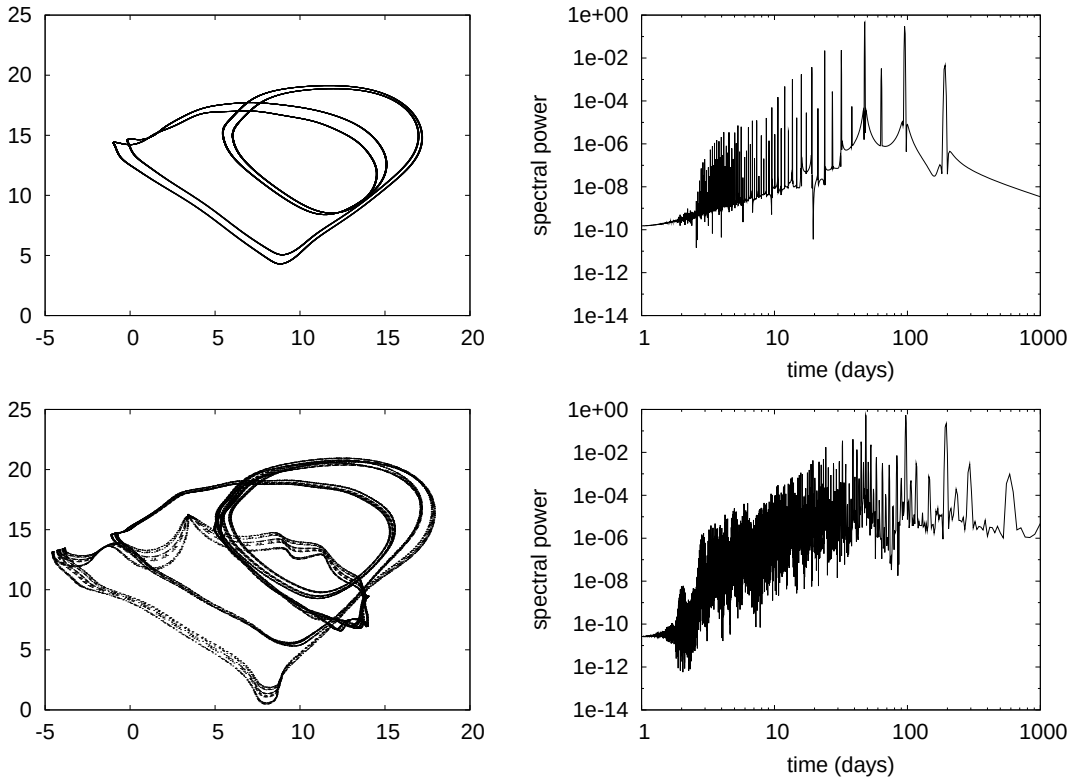

Figure 2.7. Attractors (left panels, same projection) and their power spectra (right) for $h_0 = 1200$ m. Top: periodic orbit after two period doublings ($U_0 = 14.48$ m/s). Bottom: strange attractor after a period doubling cascade ($U_0 = 15$ m/s).

The periodic orbits losing stability here belong to the branch created at the Hopf curve H_2 (see previous section). The 2-torus attractors quickly break down giving rise to a strange attractor (Figure 2.8). This strange attractor exhibits low-frequency behaviour in the range 10-100 days. The main spectral peaks at 56 and 11 days are inherited from the 2-torus, which has two frequencies $\omega_1 = 0.0178$ days^{-1} and $\omega_2 = 0.0888$ days^{-1} for parameters right after the Hopf-Neĭmark-Sacker bifurcation. In turn the torus inherits one of the frequencies from the periodic orbit, which has a period of approximately 56 days just before the Hopf-Neĭmark-Sacker bifurcation ($U_0 = 14.74$ m/s, $h_0 = 900$ m, not shown).

The process leading to the creation of the above strange attractor involves transition through a number of phase-locking windows as U_0 is increased. Figure 2.9 shows Poincaré sections for $U_0 = 14.750$ m/s up to $U_0 = 14.780$ m/s with step 0.001

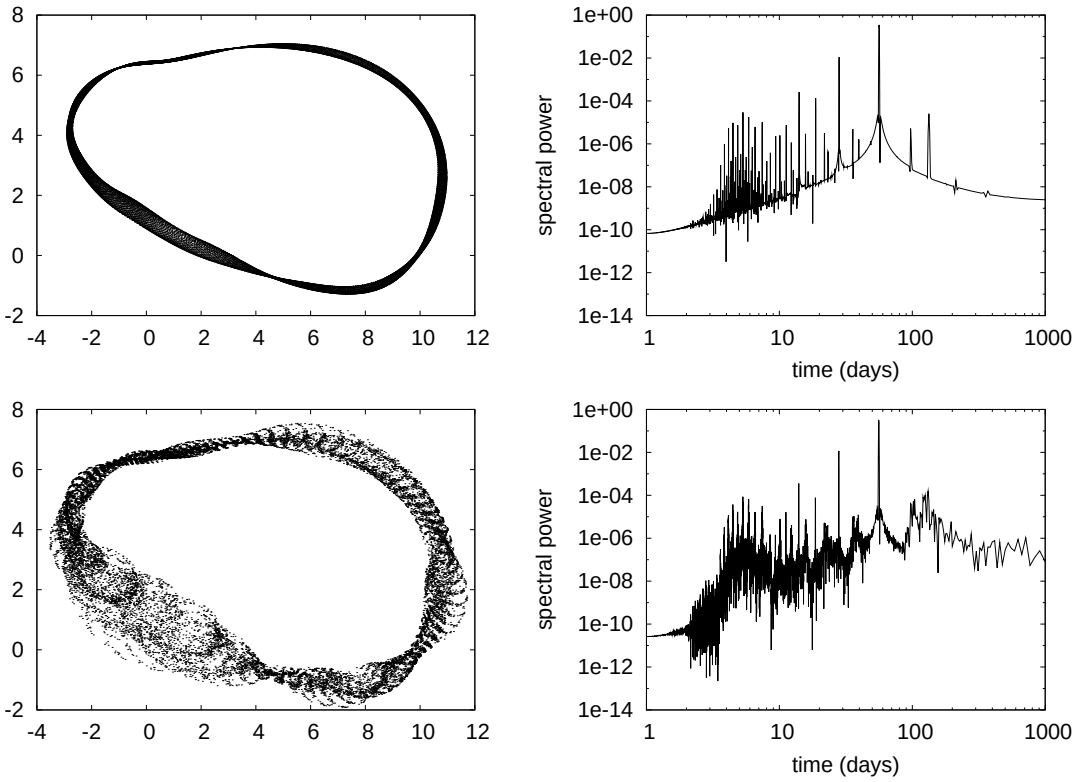

Figure 2.8. Same as Figure 2.7 for $h_0 = 900$ m: a 2-torus attractor (top, $U_0 = 14.75$ m/s) and a strange attractor after the 2-torus breakdown (bottom, $U_0 = 14.78$ m/s).

m/s with $h_0 = 900$ m fixed. Densely filled invariant circles and periodic points in the Poincaré section correspond to quasi-periodic 2-tori and periodic orbits of the flow, respectively. Periodicity windows with with periods 16, 25, 34, 9, and 11 are crossed as U_0 is increased, until the invariant circle breaks up and the quasi-periodic dynamics is replaced by chaotic dynamics. The size of the attractor is growing rapidly in phase space as U_0 is changed. The breakdown of a 2-torus typically involves homo- and heteroclinic bifurcations; see §2.3.3 for details.

Intermittency. The saddle-node curve SP_4 in Figure 2.1 forms one of the boundaries between the regions of periodic and chaotic behaviour in the Lyapunov diagram. Figure 2.10 (top left panel) shows a stable periodic orbit born at the curve SP_1; the period is 10 days. When the parameters cross the saddle-node curve SP_4, the stable periodic disappears and a strange attractor is found; see Figure 2.10 (bottom left).

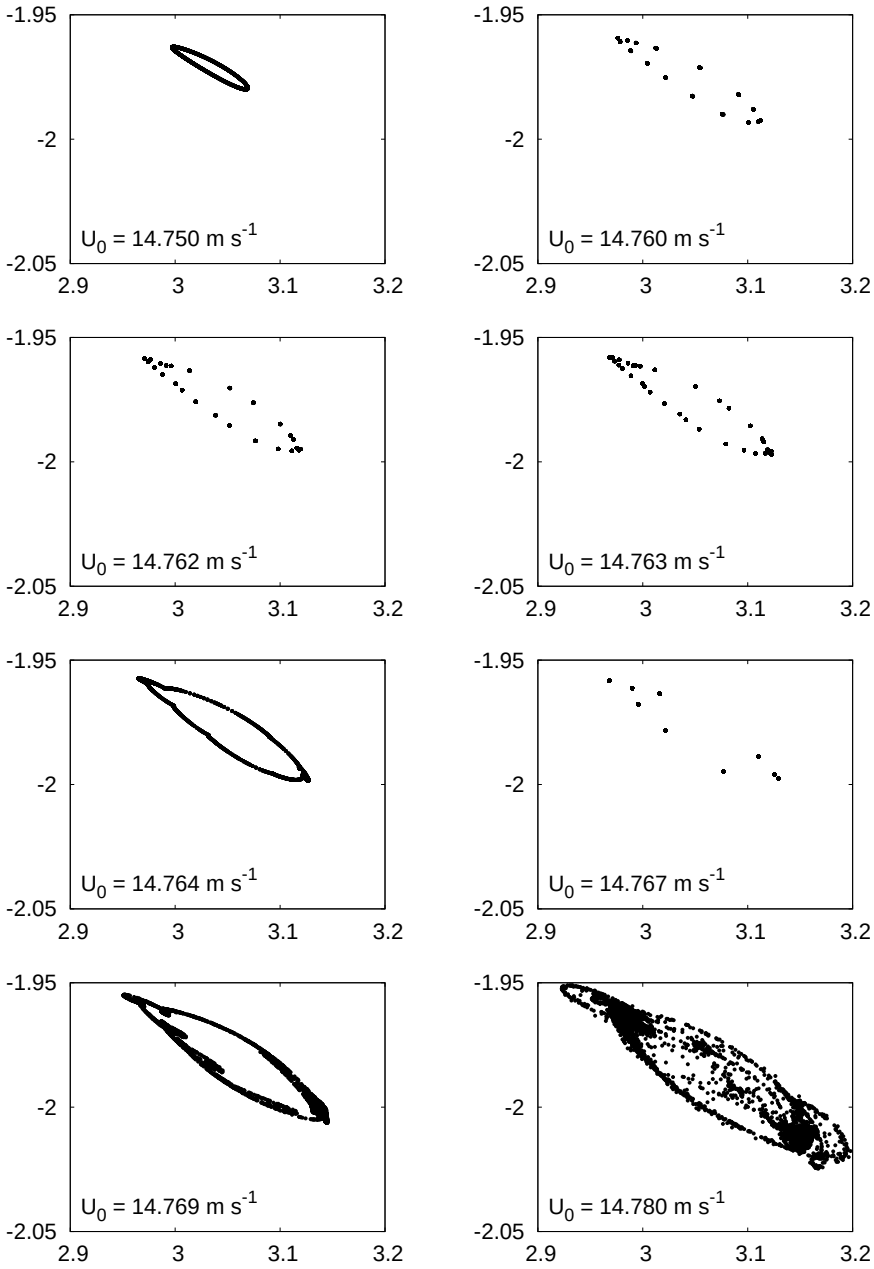

Figure 2.9. Breakdown of the 2-torus attractor, visualised in the Poincaré section $\widehat{u}_{2,0,0} = 1.8$, projection on $(\widehat{u}_{2,0,1}, \widehat{u}_{2,0,2})$: alternation of periodic, quasi-periodic, and chaotic dynamics as the parameter U_0 is varied with constant $h_0 = 900$ m.

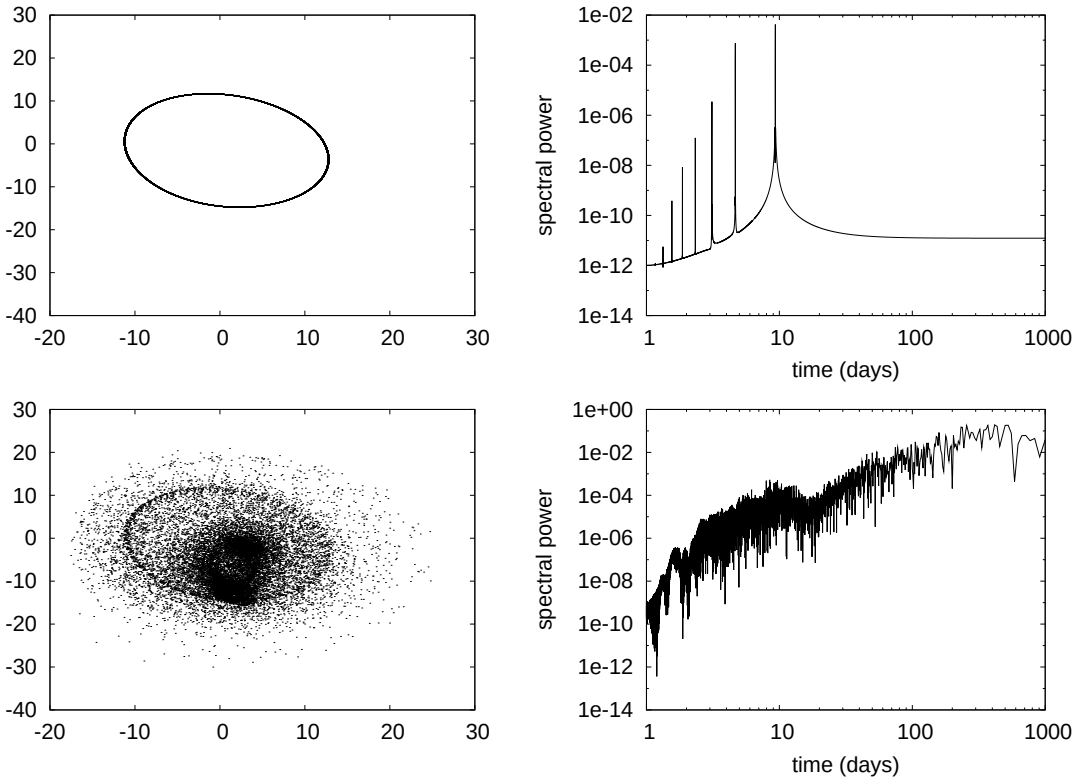

Figure 2.10. Same as Figure 2.7 for $h_0 = 800$ m. Top row: stable periodic orbit before the saddle-node bifurcation ($U_0 = 14.87$ m/s). Bottom row: strange attractor after the saddle-node bifurcation ($U_0 = 15$ m/s).

The dynamics on the attractor seems to consist of a sequence of passages close to heteroclinic orbits between different objects. The attractor coexists with (at least) the following objects:

- an unstable periodic orbit with a 2-dimensional unstable manifold (due to one pair of complex conjugate Floquet multipliers in the right half-plane).
- three unstable equilibria with unstable manifolds of dimension 4, 3, and 2 (due to two, one, and one pair(s) of complex conjugate eigenvalues in the right half plane, respectively).

Time series of various observables of an orbit on the attractor are shown in Figure 2.11. At least two different regimes can be detected. Regimes of nearly regular periodic behaviour correspond to intermittency near the formerly existing stable

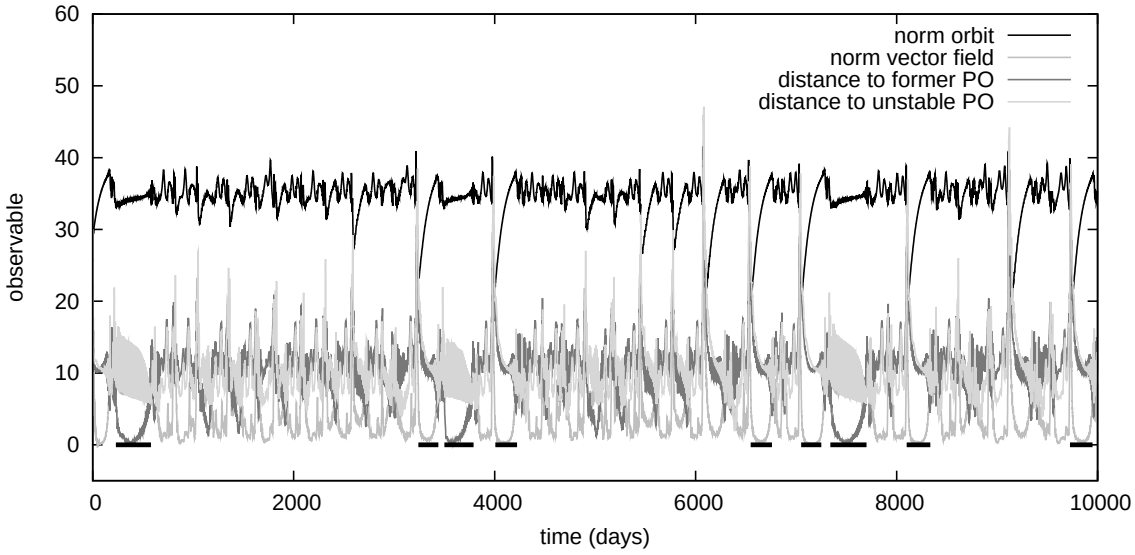

Figure 2.11. Four time series, derived from one orbit on the attractor in Figure 2.10 using four different observables: the norms of the orbit and the vector field and the distances of the orbit to the position of the formerly existing periodic orbit and the unstable periodic orbit. Black bars underneath mark time intervals of intermittency near either the periodic orbit or an equilibrium.

periodic orbit, which disappeared through the saddle-node curve SP_4. Regimes of nearly stationary behaviour are observed when the orbit approaches one of the three equilibria mentioned above. These regimes are alternated with irregular behaviour.

The intermittency regimes often occur directly after the orbit approached one the equilibria, but this is not always the same equilibrium. We have tested this by computing a large number of orbits, for which the initial conditions are random points in the tangent space to the unstable manifold of the equilibrium. The intermittency regime can be reached immediately by starting near the equilibria with the 4-dimensional and 3-dimensional unstable manifolds. When starting near the equilibrium with the 2-dimensional unstable manifold, however, the orbit shows irregular behaviour before reaching the intermittency regime.

Orbits on the attractor never approach the unstable periodic orbit within a small distance. Again we have computed a large number of orbits, for which the initial conditions are random points in the tangent space of the unstable manifold of the periodic orbit. In general, first a long transient of irregular behaviour is observed, and then the orbit reaches the intermittency regime.

2.3.3 Theoretical remarks

The results of the previous subsections are now interpreted in terms of known theory.

Bifurcations of equilibria and periodic orbits. The codimension-1 bifurcations of equilibria and periodic orbits we have found are standard and have been described extensively in the literature; see, for instance, Broer et al. (1996); Broer and Takens (2010); Guckenheimer and Holmes (1983); Kuznetsov (2004) and the references therein. For each bifurcation a (truncated) normal form can be derived by restricting the vector field to an approximation of a centre manifold. This normal form can be used to check the appropriate genericity and transversality conditions and to study different unfolding scenarios. This methodology is described in detail in Kuznetsov (2004); see Simó (1990) for other methods of computing normal forms.

The codimension-2 bifurcations of equilibria (Bogdanov-Takens, Hopf-Hopf, and Hopf-saddle-node) have been described in detail in Kuznetsov (2004). In this case, however, the truncated normal forms only provide partial information on the dynamics near the bifurcation. The Hopf-saddle-node bifurcation for diffeomorphisms has been studied extensively in Broer et al. (2008a,b).

Period doubling route. This scenario for the birth of strange attractors is theoretically well-understood, see for example Broer et al. (1998), Devaney (1989), and references therein. Strange attractors obtained from infinite period doublings in one direction may be reached at once by homo- and heteroclinic tangencies from another direction (Palis and Takens, 1993). When curves of period doubling bifurcations form unnested islands, the chaotic region can be reached by a variety of routes, including the breakdown of a 2-torus or the sudden appearance of a chaotic attractor (Wieczorek et al., 2001).

2-tori and their breakdown. It is well known that 2-torus attractors of dissipative systems generically occur as families of quasi-periodic attractors parameterised over a Cantor set (of positive 1-dimensional Hausdorff measure) in a Whitney-smooth way (Broer et al., 1996, 1990; Broer and Takens, 2010). These attractors are often a transient stage between periodic and chaotic dynamics.

The birth and death of periodic orbits on an invariant torus occur when the parameters move across Arnol′d resonance tongues. These are regions in the parameter plane bounded by pairs of curves of saddle-node bifurcations originating from a common resonant Hopf-Neĭmark-Sacker bifurcation. For parameters inside a tongue the dynamics on the torus is phase locked, meaning that the invariant circle of the

Poincaré map (defined by a section transversal to the torus) is the union of a stable periodic point and the unstable manifolds of an unstable periodic point (see, for example, the top right panel in Figure 2.9). The circle can be destroyed by homoclinic tangencies between the stable and unstable manifolds of the unstable periodic point, or the circle can interact with other objects via heteroclinic tangencies. See Broer et al. (1993) and Broer et al. (1998) for an extensive discussion.

Intermittency. The phenomenon of intermittency near a saddle-node bifurcation is well-known (Pomeau and Manneville, 1980), but it only explains a part of the dynamics on the strange attractor in Figure 2.10. The geometric structure of the attractor remains unclear too.

In some cases strange attractors are formed by the closure of the unstable manifold of a saddle-like object. This *Ansatz* is discussed in several works, see e.g. Broer et al. (1998); Broer and Takens (2010) and references therein. However, the structure of the attractor in Figure 2.10 seems to be more complicated, involving interaction with *several* nearby invariant objects (equilibria, periodic orbits) of saddle type. Another possibility is that the attractor arises through a scenario studied by Zeeman (1982), in which the main saddle of a horseshoe is annihilated by an attracting node. See also the papers by Takens (1987) and Díaz et al. (2001).

We consider it as an interesting problem for future research to investigate the structure of the attractor in Figure 2.10 in more detail. At least the stable and unstable manifolds of the equilibria and the periodic orbit should be computed, in order to gain more insight in the structure of the attractor. Next, the 'genealogy' of the attractor should be determined, e.g., by identifying whether the present shape is created through a sequence of bifurcations. For a more thorough analysis it might be necessary to derive a simpler model for this attractor, having a state space with the lowest possible dimension.

2.3.4 Physical interpretation

In this section we investigate the physical aspects (mainly instability and wave propagation) associated with the attractors analysed in the previous section. Hopf bifurcations are first interpreted in terms of geophysical fluid dynamical instabilities, giving rise to planetary waves. The structure of these waves is then studied through Hovmöller diagrams of the vorticity field (Hovmöller, 1949). This allows us to visualise structural differences and changes, such as the onset of large-scale meanders in the westerly wind.

Hopf bifurcations. A fluid is said to be hydrodynamically unstable when small perturbations of the flow can grow spontaneously, drawing energy from the mean flow. At a Hopf bifurcation an equilibrium loses its stability and gives birth to a periodic orbit. In the context of a fluid this can be interpreted as a steady flow becoming unstable to an oscillatory perturbation (such as a travelling wave). Two wave instabilities are well-known in geophysical fluid dynamics: barotropic and baroclinic instabilities. The fundamental difference lies in the source of energy: perturbations derive their energy from the horizontal shear of the mean flow in a barotropically unstable flow. In a baroclinically unstable flow, perturbations derive their kinetic energy from the potential energy of the mean flow associated with the existence of vertical shear in the velocity field. The reader is referred to standard textbooks on geophysical fluid dynamics for a full discussion on this subject (Dijkstra, 2005, 2008; Holton, 2004).

At a Hopf bifurcation the Jacobian matrix of the vector field has two eigenvalues $\pm\omega i$ on the imaginary axis. Let $\Phi_1 \pm i\Phi_2$ denote corresponding eigenvectors, then

$$P(t) = \cos(\omega t)\,\Phi_1 - \sin(\omega t)\,\Phi_2 \tag{2.7}$$

is a periodic orbit of the vector field obtained by linearisation around the equilibrium undergoing the Hopf bifurcation. This can be interpreted as a wave-like response to a perturbation of the equilibrium. The propagation of the physical pattern associated to this wave can be followed by looking at the physical fields at the phases $P(-\pi/2\omega) = \Phi_2$ and $P(0) = \Phi_1$. Figure 2.12 shows the layer thickness associated with the eigenvectors at the Hopf bifurcation H_1. Clearly, positive and negative anomalies are opposite in each layer. Moreover, this is accompanied by vertical shear in the velocity fields (not shown in the figure). Hence, we interpret this Hopf bifurcation as a mixed barotropic/baroclinic instability. The same plot for the Hopf bifurcation H_2 is given in Figure 2.13. Here, we see again that positive and negative anomalies are opposite in each layer. Therefore, we interpret this Hopf bifurcation also as a mixed barotropic/baroclinic instability.

The periodic orbits. The physical patterns associated with periodic dynamics change with the parameters U_0 and h_0. Namely the propagation features of the periodic orbits in Figures 2.3 and 2.4 differ from those at the Hopf bifurcations that gave birth to these orbits. The vorticity field associated with the periodic orbit in Figure 2.3 propagates eastward in the bottom layer, whereas it does not propagate in the top layer, see the Hovmöller diagram in Figure 2.14. Also, the variability is stronger in the top layer. The vorticity field associated with the periodic orbit in Figure 2.4 is non-propagating in both layers (Figure 2.15).

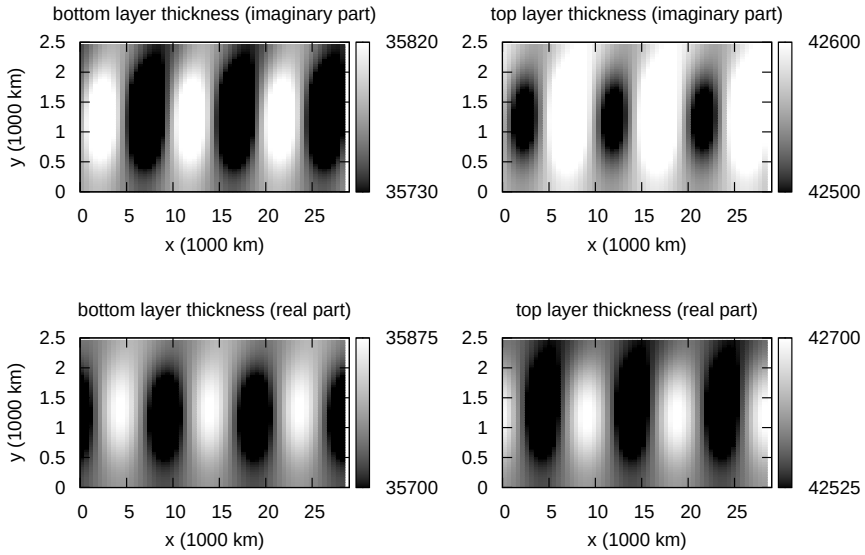

Figure 2.12. Patterns of layer thickness associated with the eigenvectors at the Hopf bifurcation H_1, for $U_0 = 12.47$ m/s and $h_0 = 800$ m. The scale is arbitrary, since any scalar multiple of (2.7) is a solution of the linearised vector field.

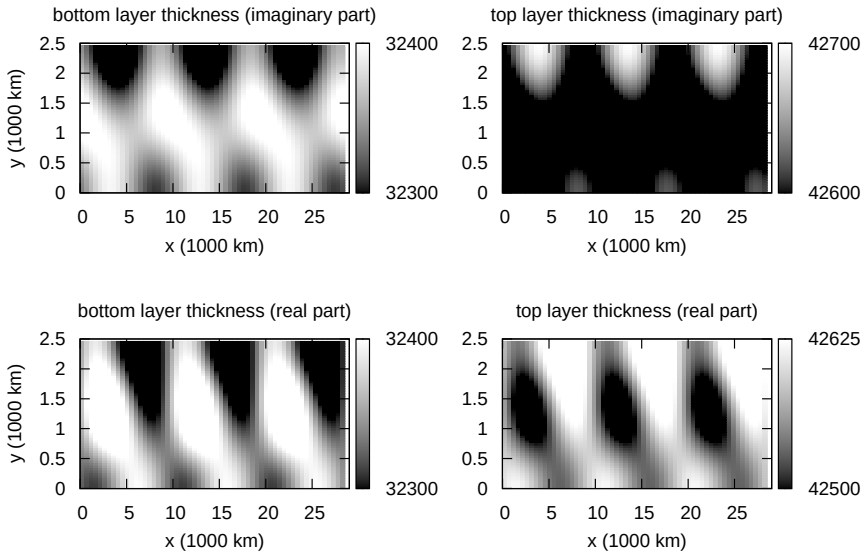

Figure 2.13. Same as Figure 2.12 at Hopf curve H_2, for $U_0 = 13.31$ m/s and $h_0 = 1200$ m.

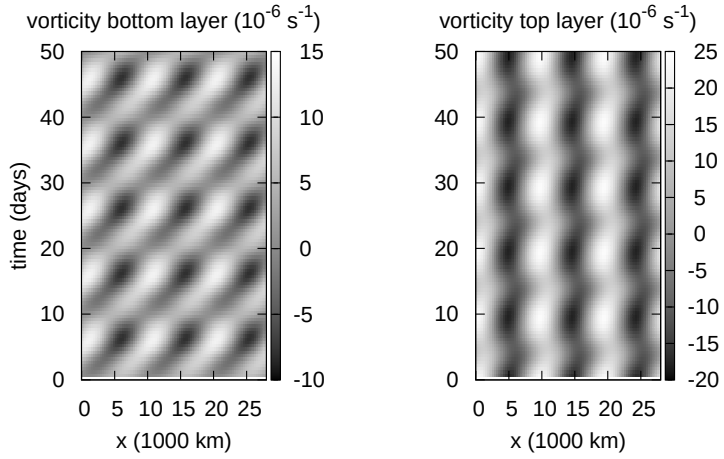

Figure 2.14. Hovmöller diagram of the periodic orbit of Figure 2.3. The magnitude of the vorticity field is plotted as a function of time and longitude while keeping the latitude fixed at $y = 1250$ km. Observe the eastward propagation in the bottom layer.

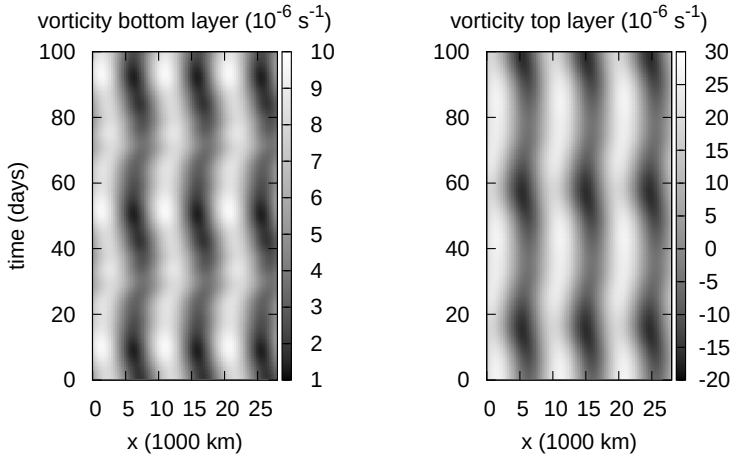

Figure 2.15. Same as Figure 2.14 for the periodic orbit of Figure 2.4. Observe that this wave is non-propagating in both layers.

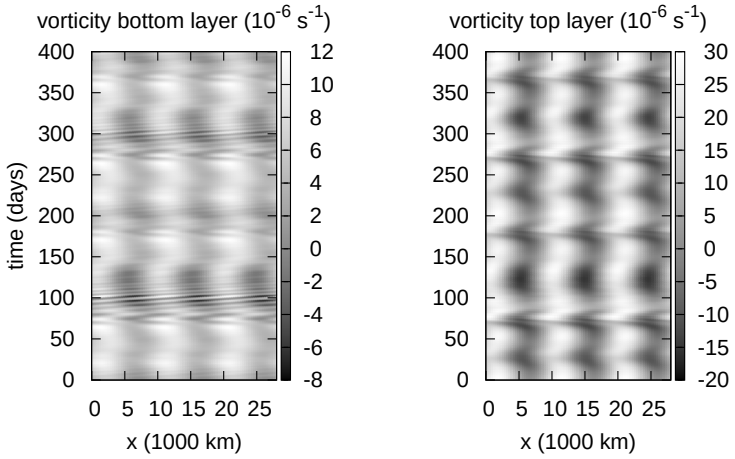

Figure 2.16. Same as Figure 2.14 for the strange attractor of Figure 2.7. The non-propagating nature is inherited from the periodic orbit of Figure 2.3. Observe the irregular variability in the bottom layer. This is due to the harmonics induced by the period doubling bifurcations.

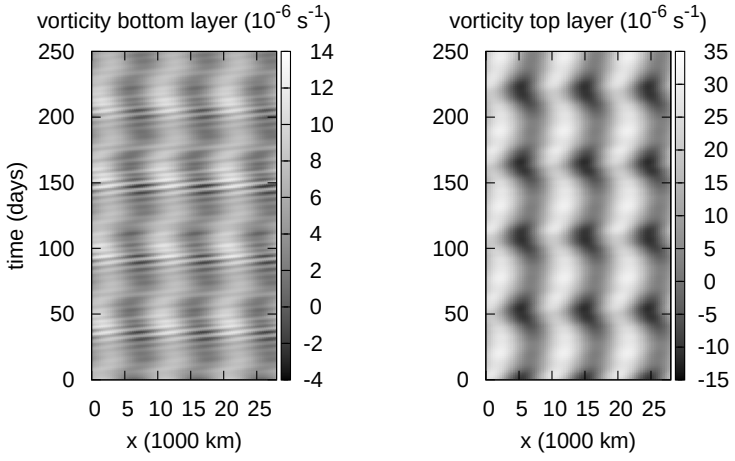

Figure 2.17. Same as Figure 2.14 for the strange attractor of Figure 2.8. Again, the non-propagating nature is inherited from the periodic orbit of Figure 2.3. The two fundamental periods (11 and 56 days) of the formerly existing 2-torus can still be identified.

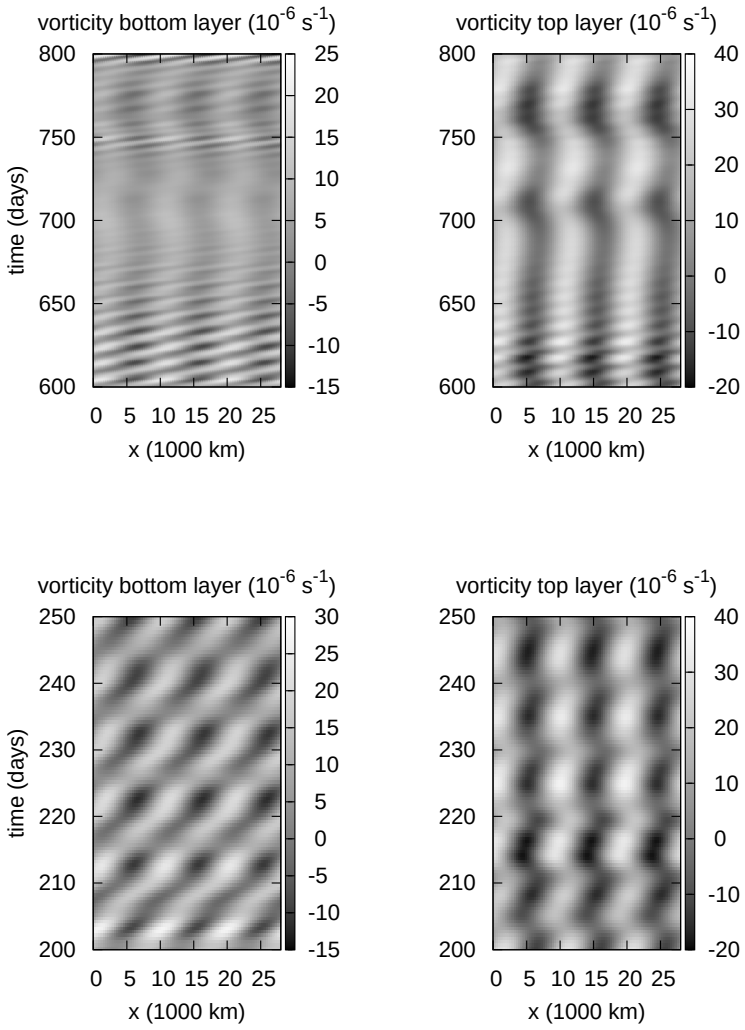

Figure 2.18. Hovmöller diagrams of the strange attractor of Figure 2.10 for two different time intervals. The magnitude of the vorticity field is plotted as a function of time and longitude while keeping the latitude fixed at $y = 1250$ km. The lower panels correspond to the intermittency regime near the vanished periodic orbit. The propagating nature in the bottom layer is inherited from the periodic orbit of Figure 2.4. The top panels are associated with a stationary regime, where the orbit approaches one of the nearby equilibria.

Period doublings. The strange attractor after the period doubling sequence is associated with non-propagating wave behaviour in both layers (Figure 2.16). The characteristic time scale is approximately 100 days. Again the variability is stronger in the upper layer.

Broken torus. The dynamics on the broken 2-torus attractor corresponds to non-propagating wave behaviour in both layers (Figure 2.17). The dominant time scale in the top layer (approximately 50 days) is longer than in the bottom layer (5 to 10 days). Both time scales are represented by peaks in the power spectrum (Figure 2.8).

Intermittency. The strange attractor in Figure 2.10 is characterised by intermittent transitions between long time episodes of nearly stationary behaviour and episodes with eastward propagating waves in the bottom layer and non-propagating waves in the top layer, see Figure 2.18.

2.4 Discussion

The results of our investigation are consistent with the hypothesis that one of the basic physical processes underlying low-frequency atmospheric variability in the northern hemisphere consists of irregular planetary-scale waves with non-propagating and temporally persistent character. Such waves are associated to mixed baroclinic/barotropic instabilities, where the baroclinic character is non-standard and a fundamental role is played by the interaction of the westerly flow with orography. These features agree qualitatively not only with observational evidence, but also with previous theories mainly based on linear instabilities, such as orographic resonance and orographic baroclinic instability (Benzi, Malguzzi, Speranza and Sutera, 1986; Benzi, Speranza and Sutera, 1986; Benzi and Speranza, 1989; Cessi and Speranza, 1985; Fraedrich and Böttger, 1978; Hansen and Sutera, 1986, 1995).

We contribute novel dynamical mechanisms to the on-going discussion on the nature of atmospheric low-frequency variability. Irregularly recurring persistent behaviour is explained in terms of intermittency associated to codimension-1 bifurcations. Specifically, irregular waves arise from two branches of periodic orbits through period doubling cascades, Hopf-Neĭmark-Sacker bifurcations followed by breakdown of a 2-torus attractor, and saddle-node bifurcations taking place on strange attractors (see Figure 2.1 and §2.3.2). Dominant time scales and propagation patterns are inherited from the periodic orbits and are in broad quantitative agreement with observational evidence (also see §2.1.2). This intermittent behaviour persists in a large domain of physically relevant parameter values.

Many studies invoking the multiple-equilibria approach following Charney and DeVore (1979) are based on barotropic models. The dynamics typically involves a Shil′nikov homoclinic bifurcation near a Hopf-saddle-node bifurcation of an equilibrium, see Broer and Vitolo (2008) for an overview. We do not take a definite stance on the multiple mode/equilibria versus single mode/equilibrium issue. The approach in this work is more akin to the spectral analysis ideas of Benzi and Speranza (1989) and Fraedrich and Böttger (1978), see §2.1.1. It has already been proposed that regimes, as identified by modes of probability distribution functions, need not be associated to (metastable) steady states of the dynamical equations (Majda et al., 2006). We do not rule out that the intermittency phenomena described in this study might provide a dynamical mechanisms for the onset of statistical modes unrelated to metastable steady states. This issue deserves specific investigation.

Our modelling approach has major advantages with respect to the barotropic quasi-geostrophic models often used to study low-frequency variability. Orography is a perturbative (small) parameter in quasi-geostrophic theories (Bannon, 1983). Instabilities in barotropic flows are fuelled by the kinetic energy of the flow rather than by the available potential energy (Benzi, Speranza and Sutera, 1986). Consequently, the transitions between the quasi-stable equilibria of barotropic models either involve variations of the zonal wind which of the order of 40 m/s, which are much larger than in reality (Benzi, Malguzzi, Speranza and Sutera, 1986; Malguzzi and Speranza, 1981), or occur at low orography (200 m). Our usage of shallow-water models with baroclinic-like forcing has allowed us:

1. to highlight the essential role of orography height in determining the propagating versus non-propagating character of the waves (the latter is only found for orography larger than 850 m);

2. to identify the mixed barotropic/baroclinic character of the waves excited on the zonal flow by the orography.

That our minimal model exhibits temporal variability in the appropriate range is already a non-trivial accomplishment, given the strongly nonlinear nature of the phenomena which we are trying to understand. We believe, however, that a more important achievement is the identification of the underlying physical process, possessing qualitative features in broad agreement with the observational evidence and previous theories. Our admittedly unrealistic 'minimal modelling' approach has allowed us to perform an extensive dynamical analysis (see e.g. Figure 2.1) offering the useful physical insight enumerated above. In this sense, we subscribe to the viewpoint of Held (2005) that the price to pay for adopting models which are overly

complex—though (potentially) more 'realistic'—with respect to the research question at hand is the risk of reduced understanding.

The most compelling issue at this point is to assess the consistence and robustness of the explanation which we have identified. For example: do nonlinear interactions of waves of different spatial scales play an essential role in the onset or the maintenance of low-frequency atmospheric variability? We just mention one amongst the many possible ways for this to occur: the North Atlantic Oscillation (NAO) low-frequency large-scale pattern is found by Benedict et al. (2004) to result from breaking of synoptic-scale waves, where the anticyclonic (cyclonic) wave breakings evolve into the positive (negative) NAO phase, also see Athanasiadis and Ambaum (2010) and references therein.

Future work. We summarise some of the many issues for future research work. From the more physical viewpoint:

1. to characterise the physical patterns associated with the regular and irregular waves, in more complex models and further away from the Hopf bifurcations;

2. to investigate nonlinear wave-wave interactions in a simple modelling framework, incorporating a few, carefully selected spatial scales beyond the planetary wave number 3 considered here;

3. to analyse the energy cycle of the waves along the lines of Lorenz (1967), see e.g. Speranza and Malguzzi (1988);

4. to analyse the relation between multimodal statistics and the intermittency scenarios identified here.

In this study we also did not touch a large number of important issues of a more computational and mathematical nature. An open issue is the structure near the organising centres of the bifurcation diagram, particularly the Hopf-saddle-node bifurcation of periodic orbits (see Figure 2.1). Near this point, a number of gaps interrupts the Hopf-Neĭmark-Sacker bifurcation curve and it is unclear whether the gaps are related to (strong) resonances or to a global mechanism as in Broer et al. (2008a).

Acknowledgements. This chapter is based on the joint paper *New nonlinear mechanisms of midlatitude atmospheric low-frequency variability* by Sterk, Vitolo, Broer,

Simó and Dijkstra (2010). Three anonymous referees are warmly thanked for constructive and insightful comments, which led to significant improvement of presentation. The authors are indebted to Professor Peter Ashwin, Professor Antonio Speranza, Professor David Stephenson, Professor Robert MacKay and Dr Sebastian Wieczorek for stimulating discussions and useful comments.

The authors kindly thank their institutions for mutual hospitality. AES is financially supported by the Netherlands Organisation for Scientific Research (NWO) by grant ALW 854.00.036. The research of CS has been supported by grant MTM2006-05849/Consolider (Spain). RV gratefully acknowledges support by the Willis Research Network.[2]

[2]http://www.willisresearchnetwork.com

Chapter 3

The Atlantic Multidecadal Oscillation

3.1 Introduction

In this chapter we develop a low-order model for thermally driven ocean flows. We use this model to study the effect of annual atmospheric forcing on the Atlantic Multidecadal Oscillation. In the next chapter we will couple the model to the low-order atmosphere model of Chapter 2.

3.1.1 The Atlantic Multidecadal Oscillation

There is ample observational evidence that the time series of the North Atlantic sea surface temperature (SST) feature a signal of variability with a time scale of several decades.

Observations. From a century of marine observations Kushnir (1994) determined the spatial structure of the temperature anomalies. The difference of the SST pattern between the relatively warm years 1970–1980 and the relatively cold years 1950–1964 shows negative anomalies near Newfoundland and positive anomalies in the rest of the basin. Delworth and Mann (2000) compare simulations of a coupled ocean-atmosphere model with a record consisting of instrumental and proxy data. They found an oscillatory mode of variability with an approximate time scale of 70 years.

The name Atlantic Multidecadal Oscillation (AMO) was coined by Kerr (2000). An index for the AMO was defined by Enfield et al. (2001) as the 10-year running mean of the detrended Atlantic SST anomalies north of the equator. Figure 3.1 shows a plot of this index computed from the HadSST2 dataset.[1]

[1] http://badc.nerc.ac.uk/data/hadsst2

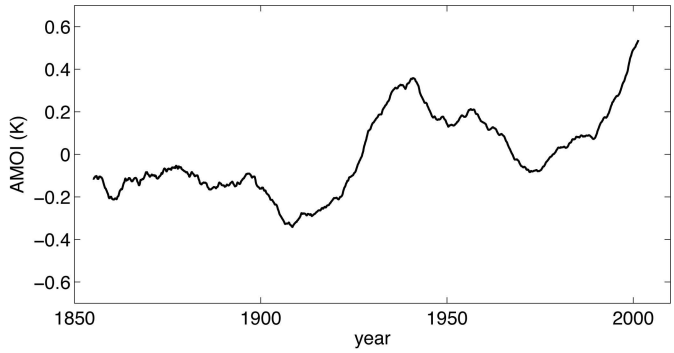

Figure 3.1. Atlantic sea surface temperature anomaly (in K) averaged from 10°N to 90°N and smoothed with a 10-year running mean.

Models and mechanisms. The study of multidecadal oscillations in thermally driven flows in idealised ocean basins goes back to Greatbatch and Zhang (1995) and Chen and Ghil (1995). In the latter paper it was suggested that the multidecadal oscillation can be related to the crossing of a critical parameter value. The relation between multidecadal oscillations and Hopf bifurcations was further investigated by Colin de Verdière and Huck (1999), Huck and Vallis (2001), and Te Raa and Dijkstra (2002).

Te Raa and Dijkstra (2002, 2003) computed three-dimensional steady flows and their linear stability in a single hemispheric sector basin. By varying a horizontal diffusivity parameter a steady state becomes unstable through a Hopf bifurcation, which gives rise to an oscillatory mode with a multidecadal time scale. This mode, called the Multidecadal Mode (MM), is characterised by a westward propagation of temperature anomalies and an out-of-phase response between the meridional and zonal overturning flows. Te Raa et al. (2004) used this characterisation to trace the MM through a hierarchy of ocean-only models, and it was found that the MM persists in this hierarchy.

Dijkstra et al. (2006) traced the spatial and temporal characteristics of the MM through a hierarchy of models while monitoring mechanistic indicators. This resulted in an explanation of the AMO based on changes in the spatial patterns of variability through the model hierarchy. The persistent nature of the MM signature supports the idea that it might provide a prototypal explanation for the AMO, see Dijkstra (2005, Chapter 6). Hereafter, we will also refer to the MM as the AMO mode.

Climate variability related to the AMO. The alternating warmer and colder phases of the AMO seem to be correlated with many types of climate variability. For

example, Enfield et al. (2001) found that during warm phases of the AMO most of the United States experience less rainfall, and between warm and cool phases Mississippi River outflow varies by 10%. Goldenberg et al. (2001) demonstrated that there is a correlation between the warm phases of the AMO and the increase in Atlantic hurricane activity. At present, however, there are no detailed mechanisms known on how the AMO might drive these climate variations.

3.1.2 A low-order model for the AMO

In this chapter we derive a low-order model for the AMO. This means that we aim for a model with the minimum number of ingredients which still captures the phenomenology of the AMO. More specifically:

1. our model only resolves the minimal amount of physics which is necessary to describe the AMO (which is explained below);

2. the governing equations of the model are reduced to a finite-dimensional system of ordinary differential equations.

In a hierarchy of models for the AMO, our low-order model is the simplest possible model. This allows us to give a coherent overview of the dynamics by studying the parameter space and the geometric structure of the attractors in detail.

In this chapter we study how the AMO is amplified by an annual cycle (modelled by parametric forcing). In Chapter 4 we investigate whether the AMO in its damped regime can be excited by atmospheric variability (possibly through a form of intermittency).

Ingredients of the model. We consider ocean flows in a rectangular ocean basin. These flows are thermally driven by relaxation of the sea surface temperature to an idealised atmospheric temperature gradient. In particular, salinity and wind stress are not taken into account. The governing equations only involve a thermal wind balance (relating vertical shear in the velocity field to horizontal temperature gradients) and an equation for the advection of temperature. These equations are formulated in terms of a system of five partial differential equations together with suitable boundary conditions.

We derive a low-order model by expanding the velocity and temperature field in a truncated series of orthogonal functions and applying a Galerkin projection. This gives a system of 27 ordinary differential equations for the time-dependent expansion coefficients.

Dynamics of the low-order model. We study the dynamics of the low-order model by means of techniques and concepts of dynamical systems. We use two parameters to study bifurcations of attractors and the associated routes to chaos: Δ controls the equator-to-pole atmospheric temperature gradient and γ controls atmospheric damping on sea surface temperature anomalies.

First, we study the dynamics of the autonomous low-order model. Next, we apply a periodic forcing modelling annual variations in heat flux at the ocean surface, and we study the associated Poincaré stroboscopic map. In the autonomous low-order model equilibria and periodic attractors are prevalent. The latter bifurcate through (cascades of) period doubling bifurcations, giving rise to Hénon-like strange attractors. The periodic attractors of the autonomous model become invariant tori of the periodically forced system (invariant circles for the Poincaré map) and they bifurcate through quasi-periodic period doubling bifurcations, giving rise to quasi-periodic Hénon-like strange attractors.

Outline. In §§3.2.1, 3.2.2 we formulate the governing equations and describe how the low-order model is obtained. In §3.3.1 we study equilibria and their stability, and in §3.3.2 we study periodic attractors and explain how they are related to the AMO. In §3.3.3 we impose a time-periodic component in the forcing terms and study quasi-periodic attractors by means of a Poincaré map. This chapter is concluded in §3.4 with a discussion of the results.

3.2 Model

In this section we give a detailed description of the governing equations and sketch the derivation of the low-order model.

3.2.1 The governing equations

In the present work we use the model of Te Raa and Dijkstra (2002) and Dijkstra (2006) with the difference that our equations are formulated in Cartesian instead of spherical coordinates. In what follows, the coordinates (x, y, z) represent longitude, latitude, and depth, respectively. In addition, we restrict to an f-plane approximation (i.e., the Coriolis force is constant). According to the mechanism of the multi-decadal variability as presented by Te Raa and Dijkstra, the AMO is still expected to occur on the f-plane. Only the spatial structure of the observed temperature fields and the amplitude of overturning circulations will differ from those obtained from models expressed in spherical coordinates. The ocean length and width of the

basin is denoted with L and the depth is denoted with D. The dynamical variables are the velocity field (u^*, v^*, w^*), the pressure field p^*, and the temperature field T^*, where the asterisks indicate that the variable is dimensional.

Forcing. Flows are forced by a restoring heat flux, which is proportional to the difference between the temperature at the sea surface and a the atmospheric temperature T_S^*. The transfer of heat occurs in a thin boundary layer, which is not resolved in our model. Hence, the surface heat flux forcing is distributed as a body force over a depth H_m of the ocean using the profile function

$$G(z) = \begin{cases} 1 & \text{if } z \geq -H_m, \\ 0 & \text{otherwise.} \end{cases}$$

Hence, the forcing heat flux is given by

$$Q_{\text{rest}} = \frac{\lambda_T}{\rho_0 C_p H_m}(T_S^* - T^*)G(z), \tag{3.1}$$

where λ_T (in W m^{-2} K^{-1}) is a constant heat exchange coefficient, ρ_0 is a reference density, and C_p is the specific heat capacity. Observe that the coefficient λ_T is related to a surface adjustment time scale τ_T through the expression

$$\tau_T = \frac{\rho_0 C_p H_m}{\lambda_T}.$$

The prescribed surface temperature of the atmosphere is idealised as

$$T_S^* = T_0 + \frac{\Delta}{2}\cos(\pi y/L),$$

where T_0 is a reference temperature and Δ is the equator-to-pole temperature difference.

Governing equations. Temperature differences cause density differences according to

$$\rho = \rho_0(1 - \alpha_T(T^* - T_0)),$$

where α_T is the volumetric expansion coefficient. Moreover, we make the following approximations:

- the effects of density differences are considered only in volume forces, but not in the equations for momentum, temperature and mass conservation (the Boussinesq approximation);

- the vertical pressure gradient balances the buoyancy force (the hydrostatic approximation);
- horizontal and vertical mixing of momentum and heat are represented by constant eddy coefficients (denoted with A_H, A_V, K_H, and K_V, respectively).

We introduce dimensionless variables by using scales L, D, U, and L/U for length, depth, velocity, and time respectively, and we define a rescaled temperature T and non-dimensional pressure p by

$$T^* = T_0 + T, \quad p^* = -\rho_0 g z + f \rho_0 L U p.$$

As the Rossby number $Ro = U/fL$ is small we neglect inertia terms in the momentum equations. Hence, the governing equations for the rescaled variables are given by

$$-v + \frac{\partial p}{\partial x} = E_H \left(\frac{\partial^2 u}{\partial x^2} + \frac{\partial^2 u}{\partial y^2} \right) + E_V \frac{\partial^2 u}{\partial z^2}, \tag{3.2}$$

$$u + \frac{\partial p}{\partial y} = E_H \left(\frac{\partial^2 v}{\partial x^2} + \frac{\partial^2 v}{\partial y^2} \right) + E_V \frac{\partial^2 v}{\partial z^2}, \tag{3.3}$$

$$\frac{\partial p}{\partial z} = Ra\, T, \tag{3.4}$$

$$\frac{\partial u}{\partial x} + \frac{\partial v}{\partial y} + \frac{\partial w}{\partial z} = 0, \tag{3.5}$$

$$\frac{DT}{dt} = P_H \left(\frac{\partial^2 T}{\partial x^2} + \frac{\partial^2 T}{\partial y^2} \right) + P_V \frac{\partial^2 T}{\partial z^2} + B(T_S - T)G(z), \tag{3.6}$$

where

$$\frac{D}{dt} = \frac{\partial}{\partial t} + u\frac{\partial}{\partial x} + v\frac{\partial}{\partial y} + w\frac{\partial}{\partial z}$$

is the advection operator. In the governing equations several nondimensional parameters appear: the horizontal and vertical Ekman numbers E_H and E_V, the Rayleigh number Ra, the inverse horizontal and vertical Péclet numbers P_H and P_V, and the Biot number B. These numbers have the following expressions in terms of the dimensional parameters:

$$E_H = \frac{A_H}{L^2 f},\ E_V = \frac{A_V}{D^2 f},\ Ra = \frac{\alpha_T g D}{f L U},\ P_H = \frac{K_H}{LU},\ P_V = \frac{K_V L}{D^2 U},\ B = \frac{L}{\tau_T U}.$$

In what follows, all dimensional parameters have the values listed in Table 3.1 unless specified otherwise. For the value of the Coriolis parameter f, the high-latitude value at 65°N is taken as being representative.

Parameter		Value	
D	depth of ocean basin	4.0×10^3	[m]
L	length and width of ocean basin	6.0×10^6	[m]
U	typical velocity scale	1.0	[m s^{-1}]
H_m	depth of surface layer	2.5×10^2	[m]
f	Coriolis parameter	1.4×10^{-4}	[s^{-1}]
α_T	volumetric expansion coefficient	1.0×10^{-4}	[K^{-1}]
τ_T	surface adjustment time scale of heat	30	[days]
ρ_0	reference density	1.0×10^3	[kg m^{-3}]
C_p	heat capacity	4.2×10^3	[J kg^{-1} K^{-1}]
A_H	horizontal eddy coefficient of momentum	3.0×10^7	[m^2 s^{-1}]
A_V	vertical eddy coefficient of momentum	1.0×10^{-3}	[m^2 s^{-1}]
K_H	horizontal eddy coefficient of heat	1.0×10^3	[m^2 s^{-1}]
K_V	vertical eddy coefficient of heat	1.0×10^{-2}	[m^2 s^{-1}]
T_0	reference temperature	15.0	[°C]
Δ	equator-to-pole temperature difference	20.0	[°C]

Table 3.1. Standard values of the dimensional parameters.

Boundary conditions. The governing equations are considered on a rectangular ocean basin, see Figure 3.2. The nondimensional spatial coordinates belong to the domain

$$(x, y, z) \in [0, 1] \times [0, 1] \times [-1, 0],$$

and on the boundaries of this domain we impose the conditions

$$x = 0, 1 \quad : \quad u = v = w = \frac{\partial T}{\partial x} = 0, \tag{3.7}$$

$$y = 0, 1 \quad : \quad u = v = w = \frac{\partial T}{\partial y} = 0, \tag{3.8}$$

$$z = -1, 0 \quad : \quad \frac{\partial u}{\partial z} = \frac{\partial v}{\partial z} = w = \frac{\partial T}{\partial z} = 0. \tag{3.9}$$

Stream function formulation. We obtain a divergence-free velocity field by introducing two scalar velocity potentials ϕ and ψ and setting

$$\begin{pmatrix} u \\ v \\ w \end{pmatrix} = \nabla \times \begin{pmatrix} \phi \\ 0 \\ 0 \end{pmatrix} + \nabla \times \begin{pmatrix} 0 \\ \psi \\ 0 \end{pmatrix} = \left(-\frac{\partial \psi}{\partial z}, \quad \frac{\partial \phi}{\partial z}, \quad \frac{\partial \psi}{\partial x} - \frac{\partial \phi}{\partial y} \right)^\top. \tag{3.10}$$

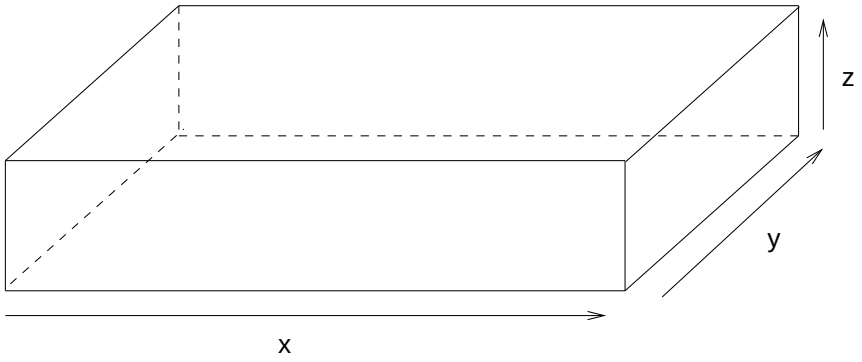

Figure 3.2. Basin of the model: the coordinates (x, y, z) represent longitude, latitude, and depth, respectively.

With this, the continuity equation (3.5) is eliminated, and the governing equations (3.2)-(3.6) can be reduced to a system of four partial differential equations for ϕ, ψ, p, and T. The boundary conditions for ϕ and ψ follow immediately from equations (3.7)-(3.9). Note that the boundary condition for the vertical velocity w at the top and bottom of the basin leads to

$$\frac{\partial \psi}{\partial x} - \frac{\partial \phi}{\partial y} = 0.$$

The equations for the velocity field (u, v, w) are diagnostic (i.e., they do not contain derivatives with respect to time) and therefore the boundary conditions for the velocity field play a less important role. To simplify the derivation of a low-order model we impose the more strict condition

$$\frac{\partial \phi}{\partial y} = \frac{\partial \psi}{\partial x} = 0$$

to ensure mass conservation.

An advantage of using stream functions is that we can eliminate the pressure gradient in the low-order model since a gradient is orthogonal to a divergence-free field with a vanishing normal component at the boundary (see Appendix A.3). Hence, the fields ψ, ϕ, and T are the only variables in the low-order model.

3.2.2 The low-order model

The governing equations in (3.2)-(3.6) form a dynamical system with an infinite-dimensional state space. We derive a system with a finite-dimensional state space by

means of a Galerkin projection. We expand the unknown fields T, ψ, and ϕ in a series of orthogonal functions with unknown time-dependent coefficients. An orthogonal projection onto the basis functions gives a set of finitely many ordinary differential equations for the expansion coefficients.

Basis functions. We use sine and cosine functions with half wave numbers

$$s_m(x) = \sqrt{2}\sin(m\pi x), \quad c_m(x) = \begin{cases} 1 & \text{if } m = 0, \\ \sqrt{2}\cos(m\pi x) & \text{if } m \neq 0, \end{cases}$$

and the functions

$$b_m(x) = \cosh(\lambda_m x) - \cos(\lambda_m x) - \frac{\cosh(\lambda_m) - \cos(\lambda_m)}{\sinh(\lambda_m) - \sin(\lambda_m)}[\sinh(\lambda_m x) - \sin(\lambda_m x)],$$

which are solutions of the boundary eigenvalue problem

$$\begin{cases} \dfrac{d^4 b_m}{dx^4} - \lambda_m^4 b_m = 0, \quad 0 < x < 1, \\ b_m(0) = b_m'(0) = 0, \\ b_m(1) = b_m'(1) = 0, \end{cases}$$

where the numbers λ_m (with $m \geq 1$) are given by the positive roots of the equation

$$\cos(\lambda) = \frac{1}{\cosh(\lambda)}.$$

The Galerkin projection. Denote with

$$R_T = \{(m, n, k) \mid 0 \leq m, n, k \leq 2\},$$
$$R_S = \{(m, n, k) \mid 1 \leq m, n, k \leq 2\},$$

the sets of wave number triplets which are retained in the Galerkin projection. This choice of the retained basis functions gives the smallest possible model in which we still can qualitatively represent the patterns in the temperature and velocity fields which were observed in previous studies of the AMO (see, for example, Te Raa and Dijkstra (2002) for pictures of such patterns).

The temperature and velocity potentials are expanded as

$$T(x,y,z,t) = \sum_{(p,q,r)\in R_T} \widehat{T}_{p,q,r}(t)c_p(x)c_q(y)c_r(z),$$
$$\phi(x,y,z,t) = \sum_{(p,q,r)\in R_S} \widehat{\phi}_{p,q,r}(t)b_p(x)b_q(y)s_r(z),$$
$$\psi(x,y,z,t) = \sum_{(p,q,r)\in R_S} \widehat{\psi}_{p,q,r}(t)b_p(x)b_q(y)s_r(z).$$

In this way, the truncated expansions satisfy the boundary conditions. By projecting the equations (3.2)-(3.6) onto the basis functions, we obtain a system of 27 ordinary differential equations for $\widehat{T}_{p,q,r}$, and a set of 16 linear algebraic equations to compute the coefficients $\widehat{\psi}_{p,q,r}$ and $\widehat{\phi}_{p,q,r}$. See Appendix A.3 for details.

3.3 Results

First, we study equilibria and their stability. For suitable parameter ranges there is a unique equilibrium which loses stability through a supercritical Hopf bifurcation when we increase a damping parameter (§3.3.1). The resulting periodic orbit has the spatio-temporal characteristics of the AMO and bifurcates through (cascades) of period doubling bifurcations (§3.3.2). With time-periodic forcing (modelling an annual cycle) the Hopf bifurcation of the autonomous system becomes a Hopf-Neĭmark-Sacker bifurcation, which gives birth to a 2-torus attractor. The latter bifurcates through quasi-periodic period doubling bifurcations (§3.3.3).

The bifurcations of equilibria and periodic orbits discussed in this section are standard; they are discussed in detail in standard text books on dynamical systems, see, for example, Guckenheimer and Holmes (1983), Kuznetsov (2004), or Broer and Takens (2010). For a discussion on quasi-periodic attractors and their bifurcations see Broer et al. (1990, 1996) or Broer and Sevryuk (2009).

3.3.1 The autonomous system: equilibria

Throughout this section, we denote state vectors of the low-order model by

$$\widehat{T} = (\widehat{T}_{0,0,0}, \widehat{T}_{0,0,1}, \ldots, \widehat{T}_{2,2,2}),$$

see §3.2.2 for the meaning of the components. We denote equilibria with $\widehat{T}_{\mathrm{E}}^{(\Delta)}$, where the superscript emphasises the dependence upon Δ.

For $\Delta = 0°\mathrm{C}$ the zero vector $\widehat{T}_{\mathrm{E}}^{(0)} = (0, \ldots, 0)$ is an equilibrium of the low-order model, which corresponds to a motionless ocean with a constant temperature in the entire basin. By continuation we compute an equilibrium $\widehat{T}_{\mathrm{E}}^{(20)}$ for the standard value $\Delta = 20°\mathrm{C}$, and this equilibrium corresponds to a steady ocean flow. In this section we discuss the physical characteristics and the linear stability of such flows.

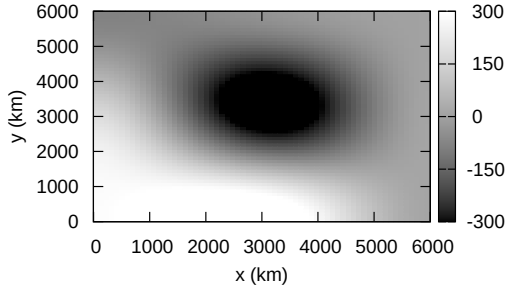

Figure 3.3. Downward heat flux (in W m^{-2}) computed from equilibrium $\widehat{T}_{\mathrm{E}}^{(20)}$. Positive (negative) values indicate heat gain (loss) from the atmosphere.

Physical characteristics. The stable equilibrium $\widehat{T}_{\mathrm{E}}^{(20)}$ corresponds to a steady ocean flow; the corresponding surface heat flux is shown in Figure 3.3. The sea surface temperature is zonally almost homogeneous. In the northern half of the basin the temperature field is vertically almost homogeneous, whereas in the southern half warmer water masses are located near the surface (Figure 3.4).

To represent 3-dimensional flows by 2-dimensional plots, we introduce the meridional and zonal overturning stream functions defined by the relations

$$\frac{\partial \Psi_{\mathrm{M}}}{\partial y} = \int_0^1 w(x,y,z)dx, \quad \frac{\partial \Psi_{\mathrm{M}}}{\partial z} = -\int_0^1 v(x,y,z)dx,$$

and

$$\frac{\partial \Psi_{\mathrm{Z}}}{\partial x} = \int_0^1 w(x,y,z)dy, \quad \frac{\partial \Psi_{\mathrm{Z}}}{\partial z} = -\int_0^1 u(x,y,z)dy.$$

The dimensional values of both stream functions are expressed in Sverdrups ($1\,\mathrm{Sv} \equiv 10^6\,\mathrm{m}^3\,\mathrm{s}^{-1}$). The meridional and zonal overturning circulations form single cells (Figure 3.5). The surface velocity is anticyclonic (i.e., clockwise) and the bottom velocity is cyclonic (i.e., counterclockwise), which is consistent with the unicellular overturnings (Figure 3.6).

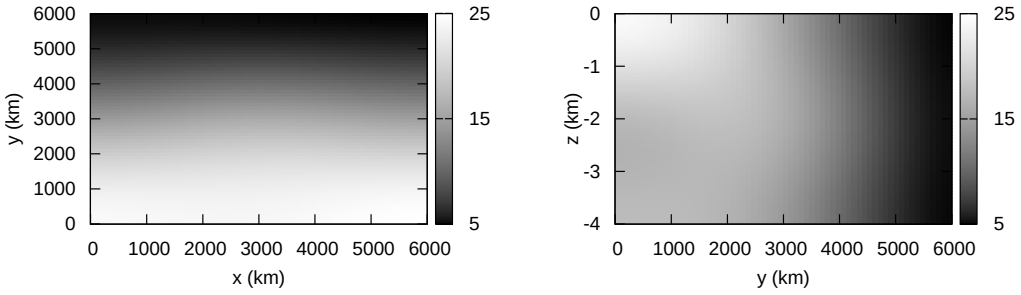

Figure 3.4. Physical characteristics of the steady flow associated with the equilibrium $\widehat{T}_{\mathrm{E}}^{(20)}$. Sea surface temperature (left) and a cross section of the temperature field at $x = 4000$ km (right).

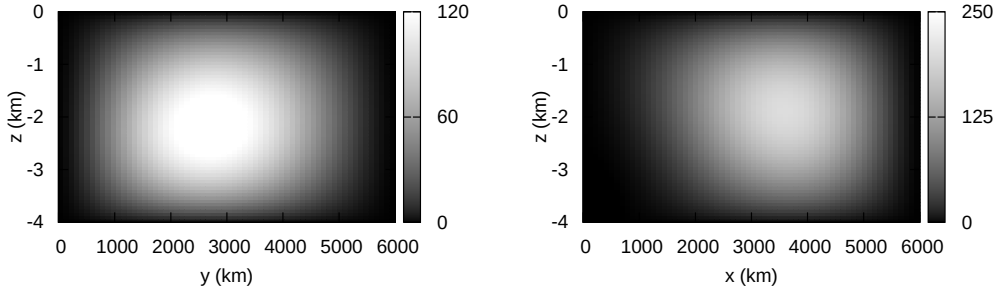

Figure 3.5. Physical characteristics of the steady flow associated with the equilibrium $\widehat{T}_{\mathrm{E}}^{(20)}$. Meridional (left) and zonal (right) overturning circulations in Sv (1 Sv $= 10^6$ m s^{-1}).

The amplitude of the overturning circulations is relatively large compared to observations. This has several reasons, the most important one being the large value of vertical heat diffusion coefficient K_V. We chose this value to prevent unstable stratifications, i.e., cold water on top of warm water. Lower values of K_V can be chosen when a so-called convective adjustment procedure is implemented to prevent unstable stratifications, see Te Raa and Dijkstra (2002) for details. Moreover, the low-order model has limited spatial resolution. In particular, the ocean basin is too large near the north pole due to the rectangular shape of the basin.

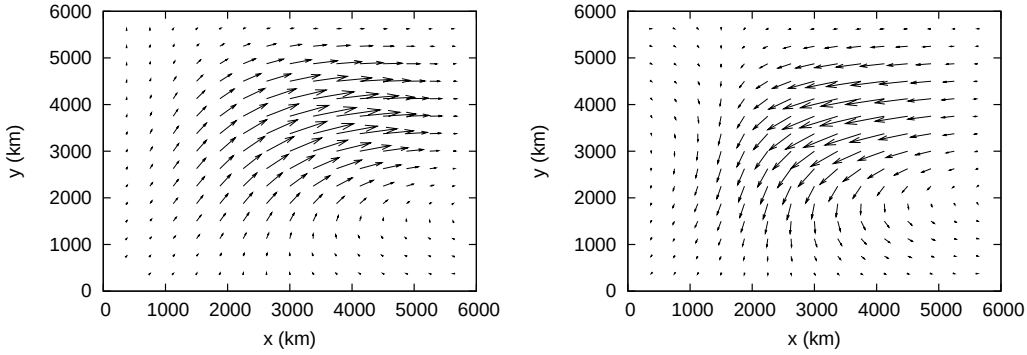

Figure 3.6. Physical characteristics of the steady flow associated with the equilibrium $\widehat{T}_{\mathrm{E}}^{(20)}$. Velocity field at the surface (left) and bottom (right) of the basin.

Stability under prescribed heat flux. We define a prescribed heat flux associated with the equilibrium $\widehat{T}_{\mathrm{E}}^{(\Delta)}$ by

$$Q_{\mathrm{pres}} = B(\widehat{T}_S - \widehat{T}_{\mathrm{E}}^{(\Delta)}).$$

We define a new heat flux

$$Q_\gamma = (1-\gamma)Q_{\mathrm{rest}} + \gamma Q_{\mathrm{pres}}, \tag{3.11}$$

which interpolates between restoring ($\gamma = 0$) and prescribed heat flux ($\gamma = 1$). The parameter γ essentially modifies the atmospheric damping of sea surface temperature anomalies: $\gamma = 0$ corresponds to the damping time scale τ_T (see §3.2.1), which increases to infinity (no damping) when γ increases to 1. In what follows, we replace (3.1) in the equations by (3.11). By construction, the equilibrium $\widehat{T}_{\mathrm{E}}^{(\Delta)}$ remains an equilibrium with the forcing Q_γ for all values of γ. Hence, we can study how atmospheric damping on the sea surface temperature affects the stability of the equilibrium.

In the parameter range

$$2 \times 10^7 \leq A_H \leq 1 \times 10^8, \quad 5 \times 10^{-4} \leq K_V \leq 1 \times 10^{-2},$$

the equilibrium $\widehat{T}_{\mathrm{E}}^{(20)}$ is stable for $\gamma = 0$. By varying γ from 0 to 1, however, the equilibrium can become unstable. Figure 3.7 shows the number of unstable eigenvalues as a function of the parameter A_H for different values of K_V when $\gamma = 1$. Clearly, the equilibrium loses stability through a succession of bifurcations. These bifurcations can only be pitchfork, transcritical, or Hopf bifurcations. Indeed, since the equilibrium $\widehat{T}_{\mathrm{E}}^{(\Delta)}$ persists for all values of γ, the possibility of saddle-node bifurcations is ruled out.

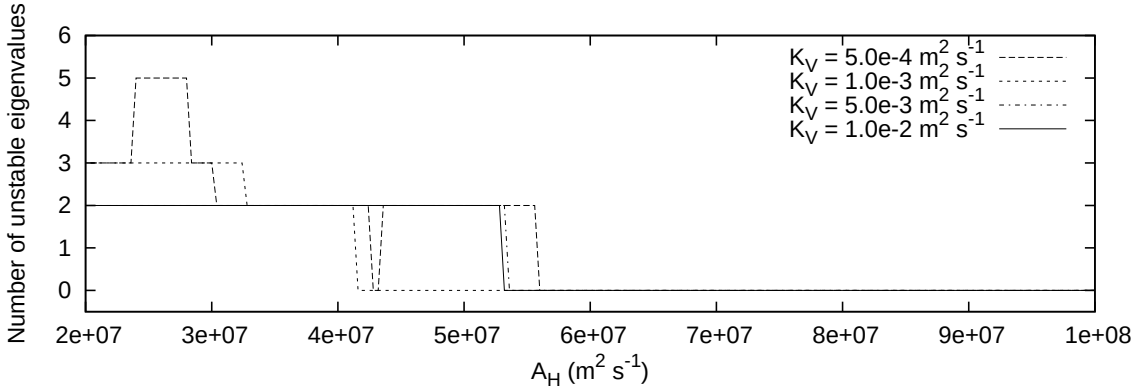

Figure 3.7. Stability of the equilibrium $\widehat{T}_{\mathrm{E}}^{(20)}$ under prescribed heat flux ($\gamma = 1$). The number of eigenvalues with positive real part is plotted as a function of A_H for fixed values of K_V.

3.3.2 The autonomous system: periodic attractors

Now we fix the values of A_H and K_V as in Table 3.1. Then the equilibrium of the previous section only loses stability through a supercritical Hopf bifurcation, which gives birth to a periodic attractor. In turn, for $\Delta \geq 22°\mathrm{C}$, this periodic attractors bifurcates through (cascades of) period doublings.

The Hopf bifurcation. By increasing the parameter γ from 0 to 1 the equilibrium $\widehat{T}_{\mathrm{E}}^{(20)}$ becomes unstable through a supercritical Hopf bifurcation which occurs at $\gamma_H \approx 0.951$ (left panel of Figure 3.8). Observe that close to the Hopf bifurcation the radius of the periodic orbit is of the order $O(\sqrt{\gamma - \gamma_H})$ as predicted by normal form theory (right panel of Figure 3.8).

Linearising the vector field around the Hopf bifurcation gives two eigenvalues $\pm\sigma_{\mathrm{im}} i$ on the imaginary axis. Let $\Phi_{\mathrm{re}} \pm i\Phi_{\mathrm{im}}$ denote corresponding eigenvectors. Then

$$P(t) = \cos(\sigma_{\mathrm{im}} t)\, \Phi_{\mathrm{re}} - \sin(\sigma_{\mathrm{im}} t)\, \Phi_{\mathrm{im}} \tag{3.12}$$

is a periodic orbit of the vector field obtained by linearisation around the equilibrium undergoing the Hopf bifurcation. This periodic orbit can be interpreted as a periodic anomaly imposed on the steady background flow associated with the equilibrium $\widehat{T}_{\mathrm{E}}^{(20)}$. The physical signature of the anomalies can be studied by looking at the patterns associated with the phases $P(-\pi/2\sigma_{\mathrm{im}}) = \Phi_{\mathrm{im}}$ and $P(0) = \Phi_{\mathrm{re}}$. The sea surface temperature associated with the eigenvectors are shown in the top panels of Figure 3.9. A warm tongue at the sea surface travels westward during one quarter

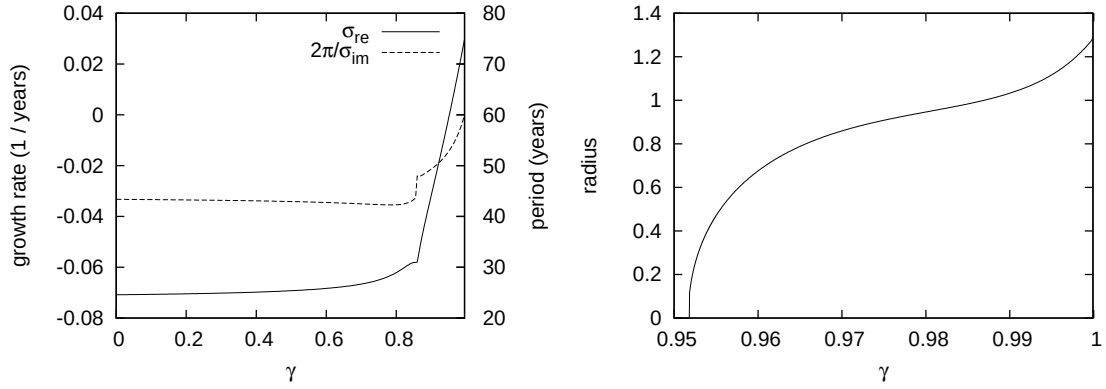

Figure 3.8. The Hopf bifurcation of the equilibrium $\widehat{T}_{\mathrm{E}}^{(20)}$. Left panel: the growth factor (σ_{re}) and period ($2\pi/\sigma_{\mathrm{im}}$) of the least stable eigenvalue pair is plotted as a function of γ for A_H and K_V fixed as in Table 3.1. A Hopf bifurcation takes place for $\gamma_H \approx 0.951$ where the growth rate becomes positive. Right panel: radius of the periodic attractor as a function of γ.

of the oscillation. In addition, there is a phase lag between the meridional and zonal overturning flows, see the bottom panel of Figure 3.9. In summary, these characteristics qualitatively agree with those of the multidecadal mode detected by Te Raa and Dijkstra (2002).

The period doubling bifurcations. For $\Delta = 20°\mathrm{C}$ the periodic orbit remains stable up to $\gamma = 1$. For larger values of Δ, however, the periodic attractor bifurcates through one or more period doublings.

Figure 3.10 shows 1-dimensional projections of attractors of a Poincaré map defined by the section $\{\widehat{T}_{0,0,1} = 2\}$. For each parameter value we computed 500 iterates of the Poincaré map, and we only plotted the last 100 iterates. Then we increase the parameter γ with 5×10^{-5} and we use the last computed point as initial condition for a new loop. For $\Delta = 22°\mathrm{C}$ only two period doublings occur, but for larger values we observe a full cascade. The bifurcation diagram shows windows of periodic behaviour which interrupt the regions of chaotic behaviour.

The locations of the period doubling bifurcations indicated in Figure 3.10 are slightly larger than the actual locations. This is due to intermittency near the bifurcations: the periodic orbits which lose stability are only weakly unstable near the bifurcation point. Therefore a large number of iterations (larger than the number used to produce Figure 3.10) is required to converge to the 'doubled' orbit. This results in tiny 'delays' in the apparent location of the period doubling bifurcations. See

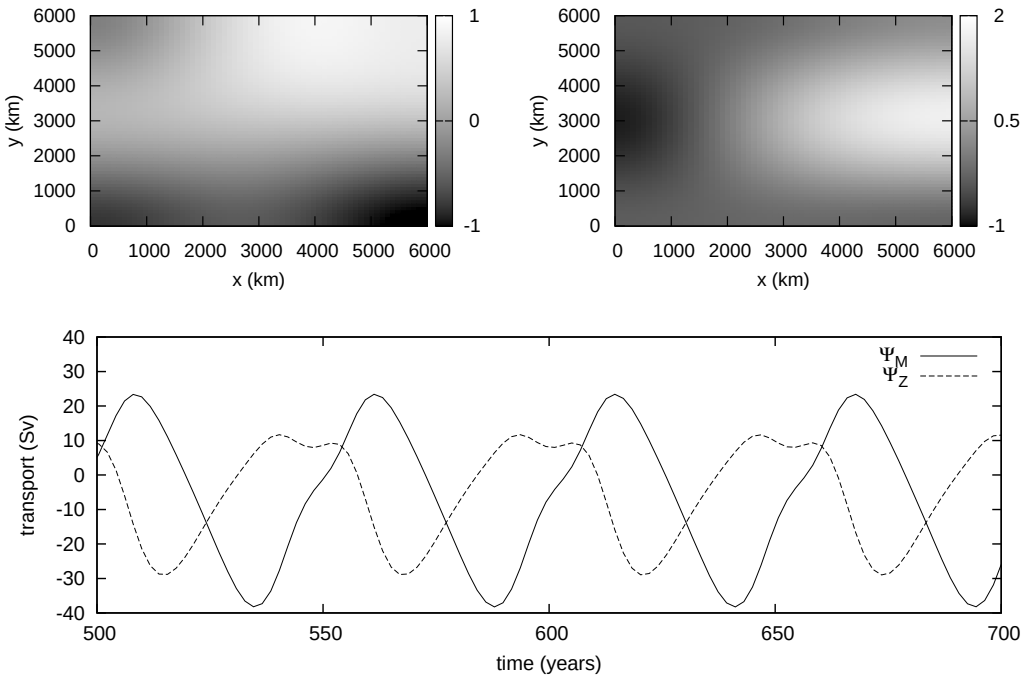

Figure 3.9. Physical characteristics of the periodic anomaly $P(t)$ defined in (3.12). Top panels: westward propagation of the sea surface temperature anomalies $P(-\pi/2\sigma_{\text{im}})$ (left panel) and $P(0)$ (right panel); contour values are omitted as the scales are arbitrary (any scalar multiple of (3.12) is also a solution of the linearised system). Bottom panel: basin averaged values of the meridional and zonal overturning circulations; observe the phase difference.

Neishtadt et al. (1995) and references therein for a detailed discussion on bifurcation delay.

At the first period doubling, the periodic orbit associated with the AMO loses stability, and gives birth to a new periodic orbit which makes two loops before closing; the period is roughly twice the original period. The doubled periodic orbit inherits the physical characteristics of the AMO: the westward propagation of temperature and the phase difference between the zonal an meridional overturning circulations. The period doubling introduces a harmonic of approximately 100 years in the variability. At subsequent period doublings more harmonics (200, 400, 800 years, etc.) are introduced in the power spectrum (not shown).

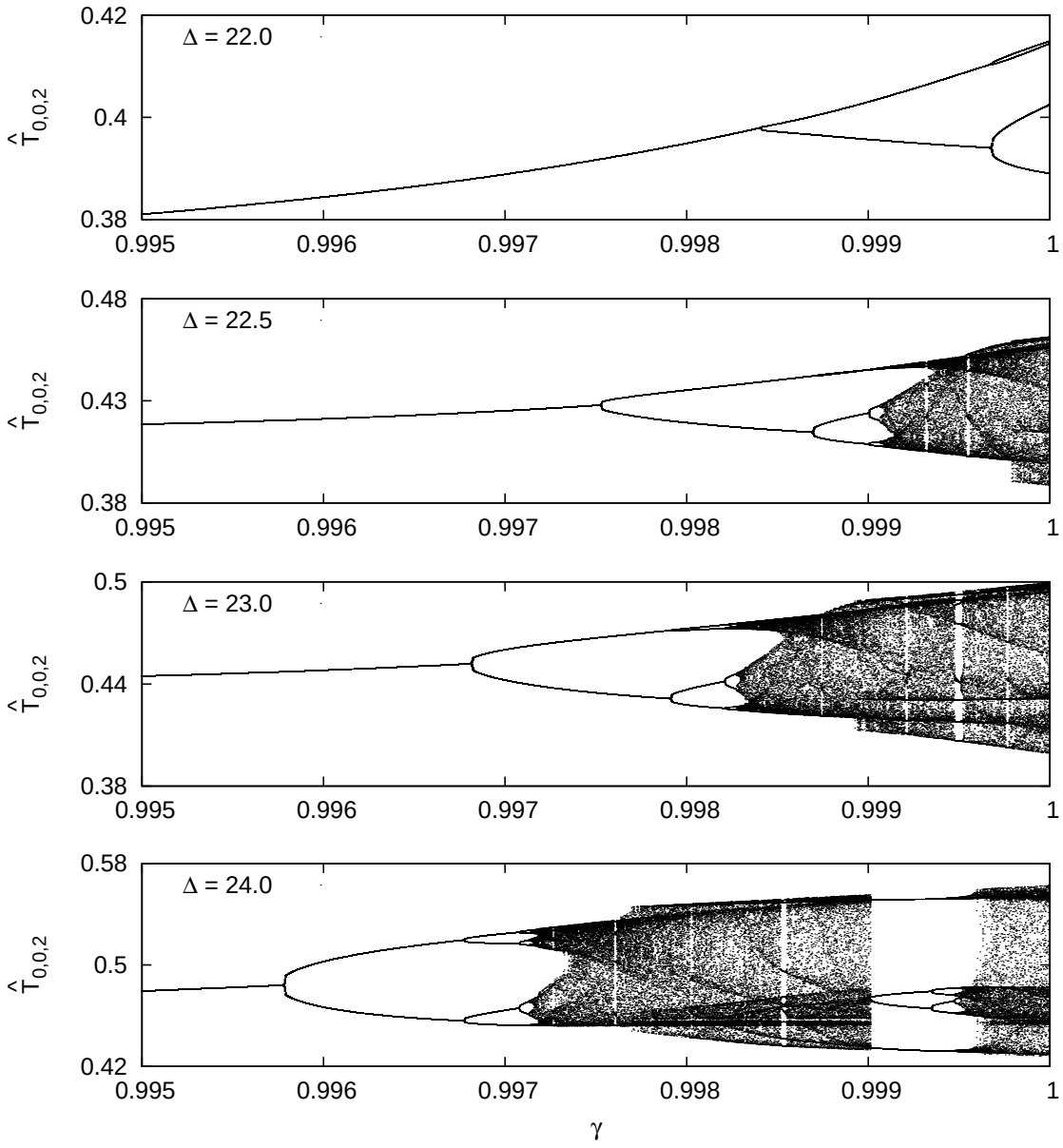

Figure 3.10. Period doubling bifurcations of the AMO mode in the autonomous system for various values of Δ, visualised in the Poincaré section $\widehat{T}_{0,0,1} = 2$. The components $\widehat{T}_{0,0,2}$ are plotted as a function of γ. For each parameter value 500 iterates of the Poincaré map are computed and only the last 100 iterates are plotted. Then the parameter γ is increased with 5×10^{-5} and the last computed iterate is used to start a new loop.

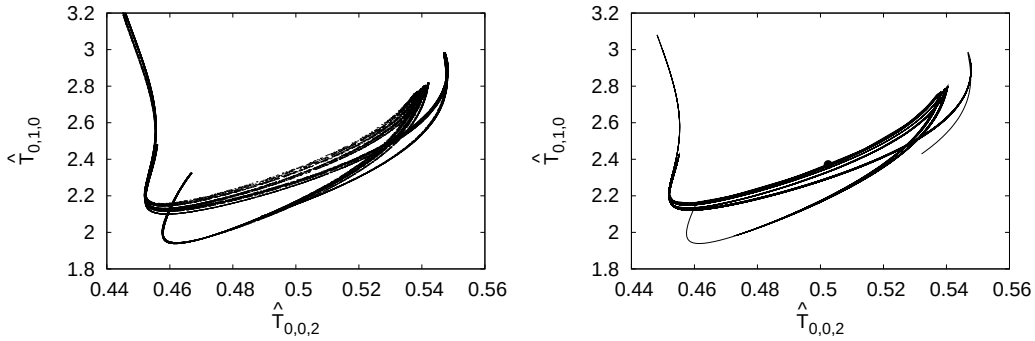

Figure 3.11. Left: strange attractor obtained for $(\Delta, \gamma) = (24; 0.998)$. Right: the 1-dimensional unstable manifold of the unstable fixed point (marked as a dot on the plot) of the Poincaré map obtained by continuation of the stable fixed point detected at $\gamma = 0.995$. Note the similarity between this curve and the strange attractor. However, there are differences in the structure of the attractor and the displayed part of the manifold; for a complete agreement one should compute a longer piece of each side of the manifold, counted from the fixed point. This requires more iterations and produces a huge file.

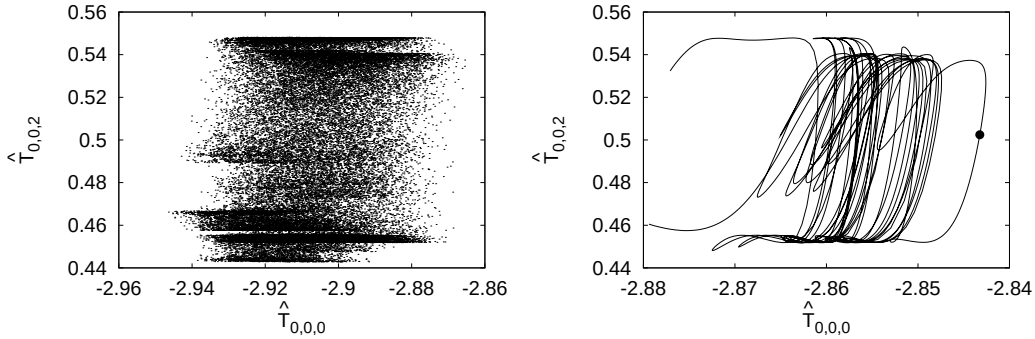

Figure 3.12. Same as in Figure 3.11, but in a different projection. Observe the wild foldings in the unstable manifold: this causes the 'white noise'-like behaviour in the variable $\widehat{T}_{0,0,0}$.

Hénon-like strange attractors. Figure 3.11 (left panel) shows a strange attractor which appears for $(\Delta, \gamma) = (24; 0.998)$ after the period doubling cascade of a fixed point of the Poincaré map defined by the section $\{\widehat{T}_{0,0,1} = 2\}$ (see the bottom panel of Figure 3.10). Figure 3.11 (right panel) shows a short piece of the 1-dimensional unstable manifold of an unstable fixed point obtained by continuation of the stable fixed point which is present for $\gamma = 0.995$. This unstable manifold almost coincides with the strange attractor, which suggests that the latter is indeed Hénon-like. Fig-

ure 3.12 is the same as Figure 3.11, but a different projection has been used. Observe that the unstable manifold is folding in very wild way. This causes the component $\widehat{T}_{0,0,0}$ to seem to behave in a noisy way.

The reader is referred to, e.g., Simó (1990) for the methodology of computing invariant manifolds.

Attractors for $\gamma > 1$. The parameter γ only has a physical meaning when its value is between 0 and 1, but attractors appearing for $\gamma = 1$ can persist for values $\gamma > 1$. We have used the same algorithm of Figure 3.10 to extend the computation of the attractors to values $\gamma > 1$ (not shown). The results are sensitive with respect to the choice of initial condition and of the step size γ_s which is used to increase the parameter γ. Not all initial conditions converge to an attractor: orbits may diverge to infinity, depending on the initial point. Also, when starting from an initial point p on an attractor for some value $\gamma = \gamma_0$, the point p may fall outside the basin of the attractor occurring at $\gamma = \gamma_0 + \gamma_s$, if the step size γ_s is too large. The orbit of p would then diverge to infinity.

3.3.3 The annually forced system: quasi-periodic attractors

In this section we study the effect of periodic forcing (modelling annual variations in the heat flux) on the AMO mode. In this setting we detect a Hopf-Neĭmark-Sacker bifurcation which gives rise to an invariant 2-torus. The dynamics on this torus correspond to the periodic forcing imposed on the AMO mode.

Forcing heat flux. Define

$$Q_{\text{per}} = (1-\gamma)Q_{\text{rest}} + \gamma Q_{\text{pres}} + P(t)S(x,y)$$

Here, P and S are functions setting the time scale and spatial structure of the forcing, respectively. We set

$$P(t) = \epsilon \cos\left(\frac{2\pi t}{\mathcal{T}}\right) \quad \text{and} \quad S(x,y) = \frac{1}{4}\left[1-\cos\left(\frac{2\pi x}{L_x}\right)\right]\left[1-\cos\left(\frac{2\pi y}{L_y}\right)\right],$$

where the parameters ϵ and $\mathcal{T}$ denote the strength and the period of the forcing, respectively. We take $\mathcal{T} = 365$ days (unless specified otherwise), and for ϵ we will use values in the range of 0.1 to 1.0. The value $\epsilon = 0.5$ corresponds approximately to 10% of the difference between the maximum and minimum over the basin of the heat flux Q_{pres}. The periodic component $P(t)S(x,y)$ can be interpreted as a very rough approximation to fluctuations observed in surface heat fluxes over the North Atlantic (Cayan, 1992a,b).

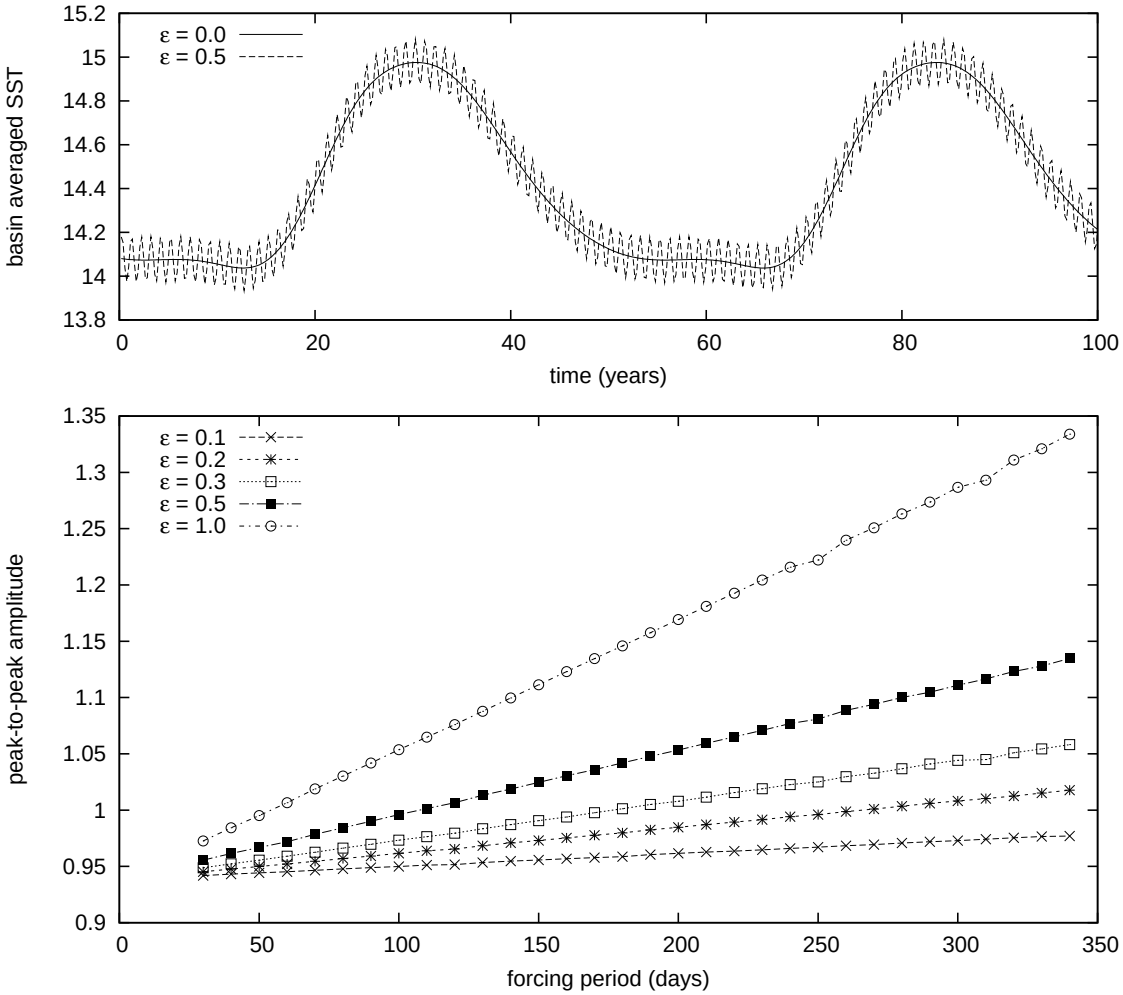

Figure 3.13. Top panel: time series of the AMO mode (solid) and a quasi-periodic attractor obtained with periodic forcing for $\epsilon = 0.5$ and $\mathcal{T} = 365$ days (dashed). The basin averaged sea surface temperature is plotted against the time in years. Bottom panel: The peak-to-peak amplitude of the basin averaged sea surface temperature as a function of the forcing period (in days) for different values of ϵ.

Amplification of the AMO mode. We fix the equator-to-pole temperature gradient at $\Delta = 20°\text{C}$ and the forcing period $\mathcal{T} = 365$ days. For $\gamma = 0.95$ the autonomous system ($\epsilon = 0$) has an equilibrium destabilising through a supercritical Hopf bifurcation which gives rise to the AMO mode. In the periodically forced system ($\epsilon > 0$) a stable periodic orbit bifurcates into an attracting 2-dimensional torus through a Hopf-Neĭmark-Sacker bifurcation where two complex conjugate Floquet multipliers cross the unit circle. This bifurcation occurs for almost the same value of γ for which the corresponding Hopf bifurcation occurred in the autonomous system.

In physical terms, the dynamics on the 2-torus attractor corresponds to the annual cycle imposed on the original AMO signal, see Figure 3.13. For most parameter values the dynamics on the 2-torus is quasi-periodic. Only for parameter values in very narrow domains the periods of the forcing and of the AMO mode become commensurate, which leads to a periodic attractor on the 2-torus. The size of the forcing amplitude ϵ determines the size of the 2-torus (in state space), or, equivalently, the amplification of the AMO.

Figure 3.13 shows the peak-to-peak amplitude of the basin averaged sea surface temperature as function of the forcing period $\mathcal{T}$ for different values of ϵ. For fixed $\mathcal{T}$ the variability increases with increasing ϵ. For fixed ϵ a larger value of $\mathcal{T}$ (i.e., a lower forcing frequency) is more effective in amplifying the AMO mode. Observe that for the different values of ϵ the variability is linear in $\mathcal{T}$. In addition, the slopes are linear functions of ϵ: computing a linear fit gives the relation

$$\text{peak-to-peak SST} = a + (c + d\epsilon)\mathcal{T},$$

with $a = 0.938549$, $c = -0.00135510$, and $d = 0.00116036$.

The Poincaré map and its attractors. The state space of the periodically forced system is 28-dimensional and is given by the Cartesian product of a circle (containing the time-periodicity) with the 27-dimensional state space of the autonomous system. We study this system by means of a Poincaré stroboscopic map (also known as a time-$\mathcal{T}$ map). We obtain this map numerically by sampling the integration output of the periodically forced system at integer multiples of the forcing period $\mathcal{T}$. This procedure reduces the dimension of the state space by one and gives a discrete time dynamical system with a 27-dimensional state space. Moreover, the complexity of attractors is reduced: an invariant 2-torus becomes an invariant circle, and a periodic orbit becomes a periodic point. In what follows, we denote the Poincaré map with P.

Now we fix the parameters $\epsilon = 0.25$ and $\mathcal{T} = 365$ and give an overview of the attractors that occur for various values in the (Δ, γ)-plane. An overview of the

dynamics of the Poincaré map P is obtained by brute force iteration. We fix the value of Δ and increase the value of γ from 0.995 up to 1.0 in steps of 10^{-5}. For each value of γ we compute 10^4 iterates of P and plot the last 500 computed points; the final point of the last attractor serves as an initial condition for the next loop. Simultaneously we compute the three largest Lyapunov exponents to classify the attractor. See Figure 3.15 and Figure 3.16. Note that this procedure does not detect the coexistence of different attractors. This can be detected by using more refined procedures with varying initial conditions. Also observe that the second Lyapunov exponent is always negative but increases to zero when the amount of damping (controlled by γ) is decreased.

As in the autonomous case, we also found attractors for values $\gamma > 1$. However, orbits may escape to infinity depending on the initial point, see a remark at the end of §3.3.2.

Quasi-periodic and periodic dynamics. For most values of the parameters the dynamics of P is quasi-periodic, meaning that evolutions densely fill an invariant circle. Only in narrow windows of the (Δ, γ)-parameter plane phase locking can be observed, where the dynamics on the invariant circle locks onto a periodic point attractor, as in Figure 3.14. This behaviour occurs when parameter values move through so-called Arnol′d tongues. These are regions in the (Δ, γ)-plane bounded by pairs of saddle-node bifurcation curves of periodic orbits originating from a common resonant Hopf-Neĭmark-Sacker bifurcation. It is precisely in these regions where the periods of the forcing and the AMO mode become commensurate.

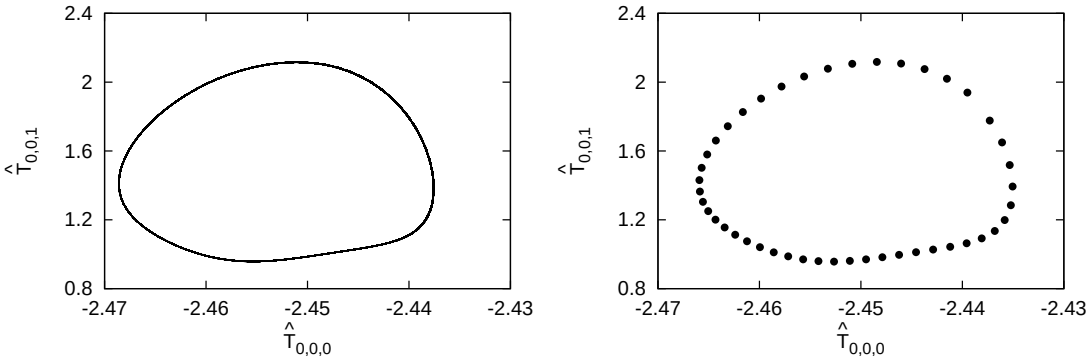

Figure 3.14. Two different attractors of the Poincaré map for $\Delta = 22°$C. Left panel: an invariant circle with quasi-periodic dynamics ($\gamma = 0.9967347$). Right panel: a periodic point attractor ($\gamma = 0.9967379$) having period 45.

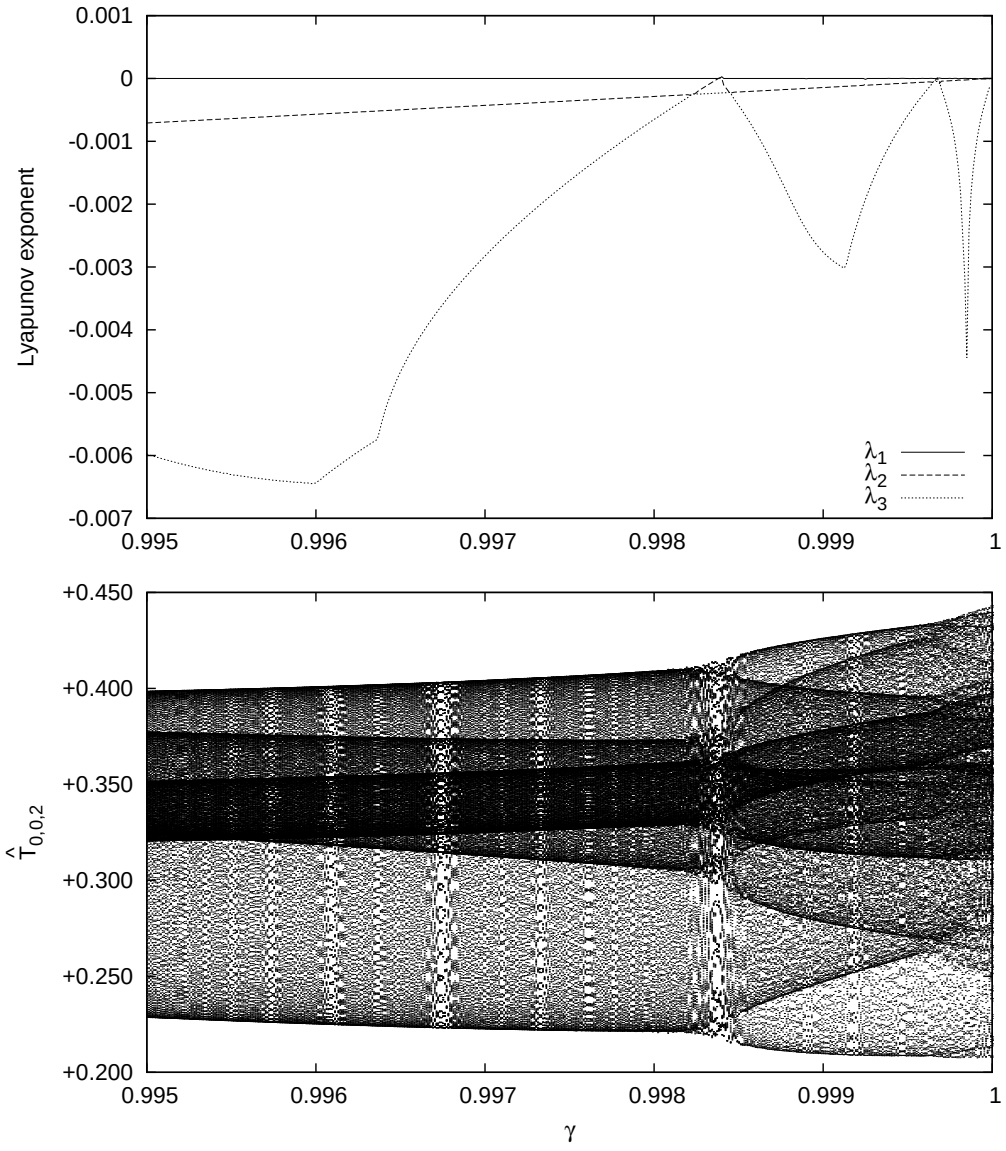

Figure 3.15. Top: the three largest Lyapunov exponents $\lambda_{1,2,3}$ as a function of γ for $\Delta = 22°\mathrm{C}$. Bottom: projections on $\widehat{T}_{0,0,2}$ of attractors of the Poincaré map as a function of γ.

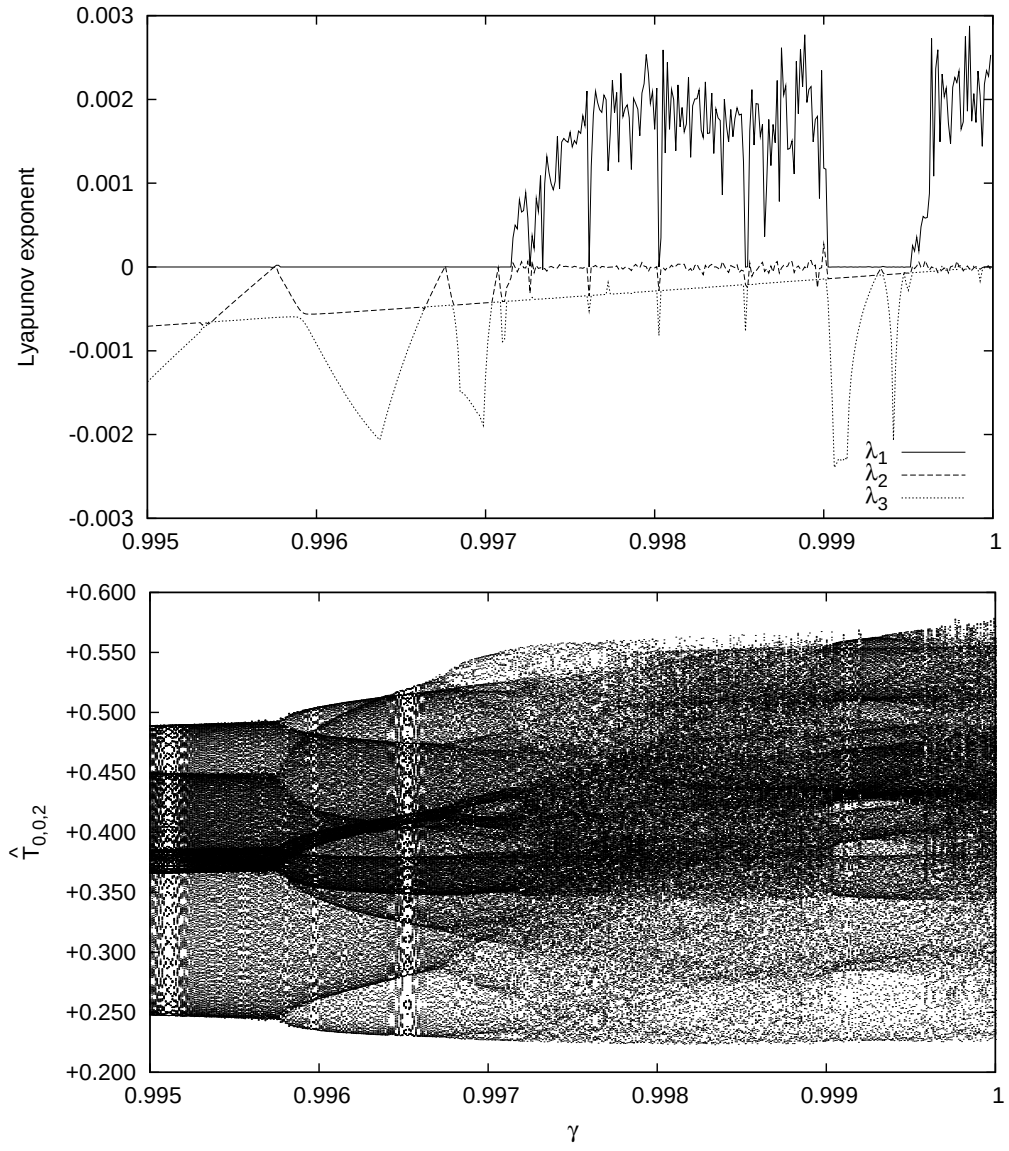

Figure 3.16. Top: the three largest Lyapunov exponents $\lambda_{1,2,3}$ as a function of γ for $\Delta = 24°\mathrm{C}$. Bottom: projections on $\widehat{T}_{0,0,2}$ of attractors of the Poincaré map as a function of γ.

Quasi-periodic period doublings. The periodically forced system exhibits doublings of the P-invariant circle (known as quasi-periodic period doublings). These bifurcations can be seen as perturbations arising for $\epsilon > 0$ from the period doublings in the autonomous system, see §3.3.2 and Figure 3.10. Indeed, the values of γ where the quasi-periodic period doublings occur for $\epsilon > 0$ are close to those where period doublings occur for $\epsilon = 0$. Period doubling bifurcations can be identified in the Lyapunov diagrams of Figure 3.15 and Figure 3.16 as the locations where the second Lyapunov exponent becomes zero.

We only detected two doublings for $\Delta = 22°\text{C}$. At least eleven doublings are detected for $\Delta = 24°\text{C}$, but only three of them are visible in the Lyapunov diagram due to the large step size in γ. The parameter values of the first eleven doublings are listed in Table 3.2, and we expect that they are followed by infinitely many additional period doublings. Figure 3.17 shows a sequence of four consecutive circle doublings.

Note, however, that further refinement of the values in Table 3.2 requires a huge computational effort. For a careful determination of the location of the period doubling the Lyapunov exponents have to be determined with an error below 10^{-6}. This requires a great number of Poincaré iterates, and usage of extrapolation techniques, see, e.g., Broer and Simó (1998) and Simó (2005). Up to 5×10^6 iterates have been used for some selected values of γ after a transient of 10^6 iterates. See Appendix B.3.2 for additional details and illustrations.

Two different types of quasi-periodic period doubling bifurcations are possible (Broer et al., 1990): as a parameter is varied, an attracting invariant circle loses stability and gives birth

1. to a single attracting invariant circle of roughly double length;

2. to a pair of disjoint circles, each mapped onto the other by the Poincaré map P (also referred to as a period-2 invariant circle).

A priori there is no reason to expect that only one of the two types occurs, but in our model we only found doublings of type 1. In cases where the invariant circle is reducible, the type of bifurcation can be deduced from the eigenvalues of an associated Floquet matrix, see Jorba (2001), Broer et al. (2008a), and Vitolo et al. (2010) for details.

From the parameter values in Table 3.2 (see also Figure B.1 in Appendix B.3.2) we conjecture that

$$\lim_{n\to\infty} \frac{\gamma_n - \gamma_{n-1}}{\gamma_{n+1} - \gamma_n} = F,$$

where $F \approx 4.6692$ is Feigenbaum's constant. The end of the period doubling cascade, γ_∞, will be located very close to $\gamma = 0.997150334$. Figure 3.16 shows that, despite the

n	γ_n	r_n	n	γ_n	r_n
1	0.9957520		7	0.997150177	4.7
2	0.99675927	3.18	8	0.997150300	4.6
3	0.99707620	5.46	9	0.9971503270	4.8
4	0.997134254	4.59	10	0.99715033265	4.8
5	0.997146898	4.68	11	0.99715033382	
6	0.997149598	4.66			

Table 3.2. Approximate locations of the first eleven quasi-periodic period doublings for $\Delta = 24°\text{C}$. In the third column the ratios $r_n = (\gamma_n - \gamma_{n-1})/(\gamma_{n+1} - \gamma_n)$ of the successive distances between the bifurcations are listed.

too large spacing in γ, this is indeed the approximate location for which the dominant Lyapunov exponent becomes positive. In similar models it is common that only a *finite number* of quasi-periodic period doublings appears, see e.g. Vitolo et al. (2010). In the present model it seems that a full cascade is present for $\Delta = 24°\text{C}$.

A full description of the quasi-periodic period doubling bifurcation of invariant circles requires in fact two parameters. Loosely speaking, one parameter is necessary to unfold the loss of normal hyperbolicity and another parameter is required to enforce a Diophantine condition for the rotation number, necessary for KAM-like persistence of the 'undoubled' invariant circle, see Broer et al. (1996, 2002); Broer, Simó and Vitolo (2010); Broer et al. (2008a,b).

In 2-dimensional parameter space the quasi-periodic bifurcation set is a Cantor set which is contained in a smooth curve, its gaps being filled with resonance bubbles, giving rise to a 'frayed' boundary. The quasi-periodic period doubling bifurcation admits a simple description only if parameters are restricted to any of the codimension one manifolds (curves in parameter space) where the rotation number is Diophantine. Much more intricate bifurcation structures are expected within the resonance 'bubbles', but the quasi-periodic bifurcation theory does not predict the generic behaviour there, see Broer et al. (2008a) for a case-study of the quasi-periodic Hopf bifurcation.

When varying only one parameter from panel (A) to (B) in Figure 3.17, the theory predicts that a quasi-periodic doubling occurs with positive probability, although one cannot exclude that a resonance 'bubble' is being crossed instead. See Broer et al. (2008a), Vitolo et al. (2010), and Chenciner (1985a,b, 1988) for a more complete discussion.

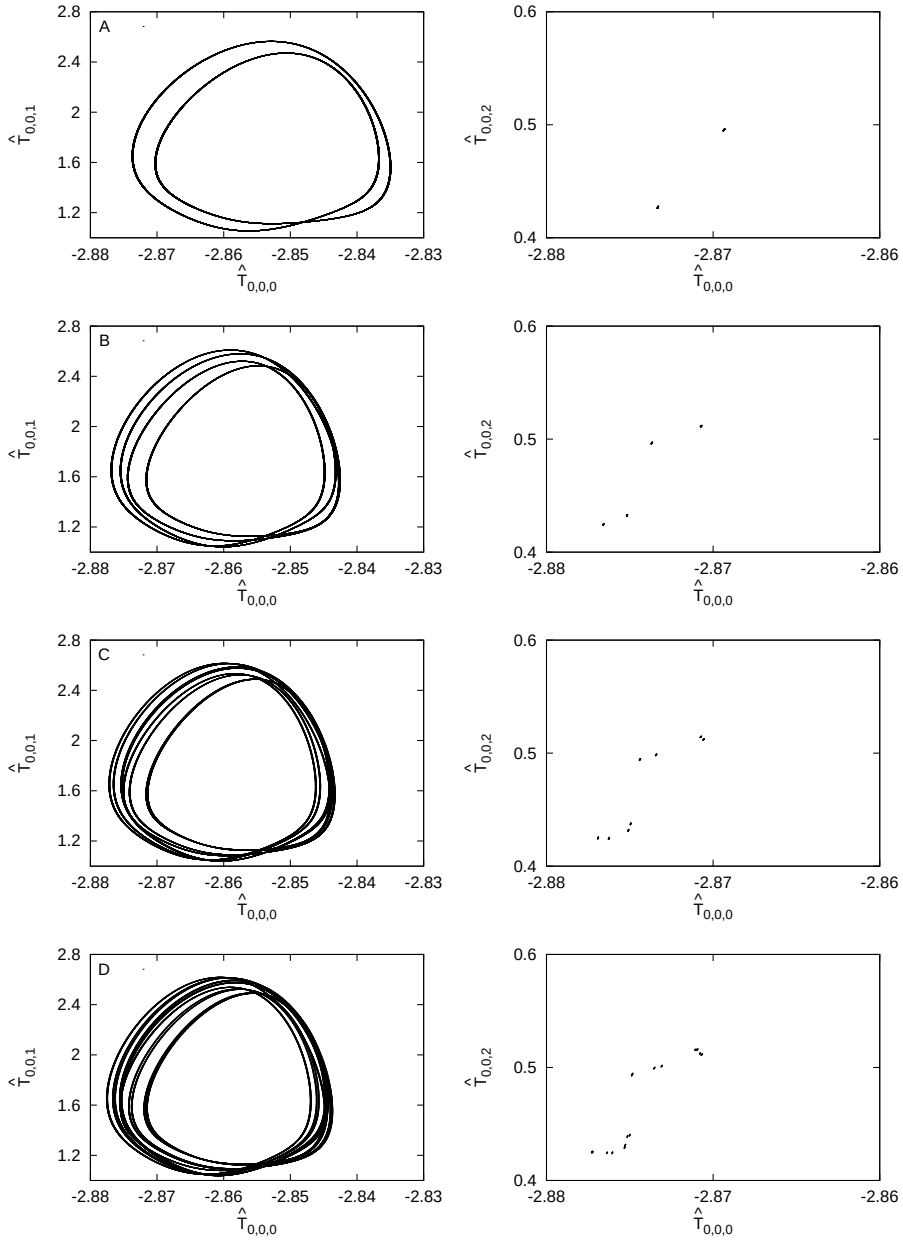

Figure 3.17. Invariant circles of the Poincaré map for $\Delta = 24°\mathrm{C}$ appearing after the first four period doublings. See Table 3.3 for the values of γ and Lyapunov exponents. Left panels: projections on $(\widehat{T}_{0,0,0}, \widehat{T}_{0,0,1})$. Right panels: projections on $(\widehat{T}_{0,0,0}, \widehat{T}_{0,0,2})$ of the points belonging to the fattened slice $|\widehat{T}_{0,0,1} - 1.8| \leq 5.0 \times 10^{-3}$.

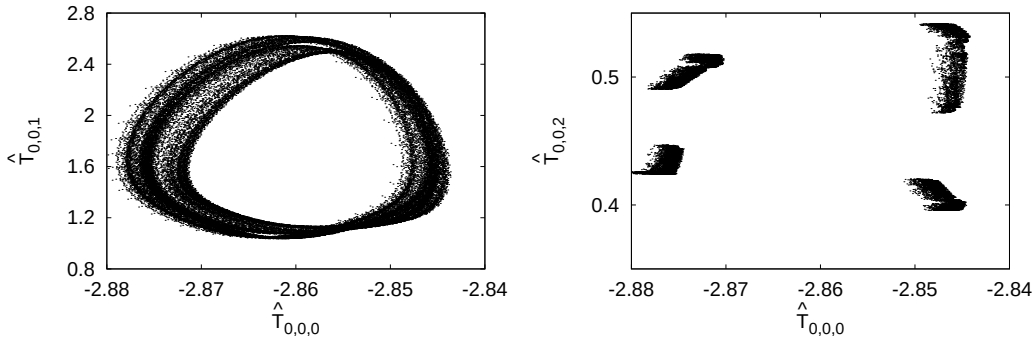

Figure 3.18. Strange attractor of the Poincaré map for $\Delta = 24°\text{C}$ appearing after the end of the period doubling cascade. Left panel: projection on $(\widehat{T}_{0,0,0}, \widehat{T}_{0,0,1})$. Right panel: projections on $(\widehat{T}_{0,0,0}, \widehat{T}_{0,0,2})$ of the points belonging to the fattened slice $|\widehat{T}_{0,0,1} - 1.8| \leq 5.0 \times 10^{-3}$.

Strange attractors. For $\gamma = 0.997185$, the strange attractor in Figure 3.18 (left panel) is detected. On this type of attractors the dynamics is chaotic: the dominant Lyapunov exponent is positive, which means that nearby evolutions separate exponentially fast.

The structure of the attractor is visualised by a 'slice', that is points contained in thin layers (width 5.0×10^{-3}) centred around hyperplanes of the form $\{\widehat{T}_{0,0,1} = 1.8\}$, see Figure 3.18 (right panel). Observe that points in this slice are rather scattered. We emphasise that this is not an error in the computations. Nor it is due to the chosen thickness of the slice: the 'fuzziness' of points in the slice persists when the thickness of the slice is reduced. The fuzziness probably results from wild foldings of an unstable manifold as in the case of the Hénon-like attractor of Figure 3.12.

The attractor shown in Figure 3.18 is reminiscent of the so-called quasi-periodic Hénon-like strange attractors, which are the closure of the unstable manifold of a saddle invariant circle. These attractors have been detected numerically in a seasonally forced Lorenz-84 model studied by Broer et al. (2002, 2005). In that case, both types of quasi-periodic doublings (1 and 2 above) have been found to occur in the same sequence, and the strange attractor appears when a homoclinic tangency of a saddle-periodic point destroys the twice-doubled invariant circle.

Invariant circles in the chaotic range. Figure 3.16 shows that the range of values of γ for which the dominant Lyapunov exponent is positive is interrupted with small windows for which the dominant Lyapunov exponent is zero. This means that the

γ	Figure	λ_1	λ_2	λ_3
0.99650	3.17A	3.2×10^{-7}	-4.9×10^{-4}	-1.2×10^{-3}
0.99700	3.17B	-2.2×10^{-7}	-4.2×10^{-4}	-1.3×10^{-3}
0.99709	3.17C	-6.0×10^{-7}	-4.1×10^{-4}	-8.9×10^{-4}
0.99714	3.17D	-1.8×10^{-7}	-1.9×10^{-4}	-4.0×10^{-4}
0.997185	3.18	4.5×10^{-4}	-5.8×10^{-5}	-4.0×10^{-4}

Table 3.3. Lyapunov exponents for the attractors shown in the listed figures.

γ	Number of windings	γ	Number of windings
0.997261	10-circle	0.998026	7-circle
0.997450	11-circle	0.998536	11-circle
0.997540	6-circle	0.998554	doubled 11-circle
0.997546	doubled 6-circle	0.999025	4-circle
0.997606	5-circle	0.999355	doubled 4-circle
0.997615	doubled 5-circle	0.999499	quadrupled 4-circle

Table 3.4. Values of γ in the chaotic range for $\Delta = 24°\mathrm{C}$ for which invariant circles occur and their number of windings.

parameter domains characterised by the occurrence of strange attractors are interrupted by parameter sets where invariant circles occur. In turn, these invariant circles can bifurcate again through quasi-periodic period doublings. This scenario is similar to what happens in cascades of period doublings for periodic orbits, cf. Figure 3.10.

The invariant circles can be detected numerically by taking small step sizes ($\gamma_s < 3 \times 10^{-6}$) in the chaotic range and brute force iteration of the Poincaré map. This procedures results shows the existence of invariant circles with a number of windings that differs from window to window. A summary of the results is presented in Table 3.4.

3.4 Discussion

In this chapter we have studied the dynamics of a model for the Atlantic Multidecadal Oscillation. Instead of using the traditional high-dimensional models (often obtained by finite-difference discretisation schemes) we have derived a low-order model by means of a Galerkin projection of the governing equations onto a finite-dimensional function space.

In our model, the AMO mode appears through a supercritical Hopf bifurcation

of a stable equilibrium (associated with a steady ocean flow) when switching from restoring ($\gamma = 0$) to prescribed heat flux ($\gamma = 1$). This is the typical bifurcation scenario associated with the AMO (Te Raa and Dijkstra, 2002; Dijkstra et al., 2008). In addition, our low-order model captures the physical signatures of the AMO mode: the multidecadal period, the westward propagation of sea surface temperature anomalies, and the phase difference between the anomalous meridional and zonal overturning circulations. The period doubling bifurcations of the AMO mode have also been detected in a high-dimensional model studied by Te Raa et al. (2004).

The new element of this study is the introduction of periodic forcing in the surface heat flux which can be interpreted as an annual cycle. Then, the stable equilibria of the low-order model are replaced by stable periodic orbits. In particular, the AMO now appears as a quasi-periodic attractor through a Hopf-Neĭmark-Sacker bifurcation of the periodic attractor associated with the annual cycle. For most parameter values the dynamics is quasi-periodic which means that the periods of the AMO and the annual cycle are incommensurate. In turn, the 2-torus can undergo various quasi-periodic period doublings, and this leads to strange attractors which are reminiscent to the quasi-periodic Hénon-like strange attractors discussed in Broer et al. (2002, 2005).

The AMO mode only has a positive growth rate near $\gamma = 1$, i.e., for almost prescribed heat flux. Prescribed heat flux in ocean models, however, is a strong idealisation since it amounts to net zero atmospheric damping. In reality sea surface temperature anomalies are substantially damped by the atmosphere. The results of this chapter show that annual atmospheric forcing increases the amplitude of the AMO in supercritical conditions, but it does not shift the supercritical regime to lower values of γ. On the other hand, atmospheric variability is not purely periodic. In fact, the atmosphere shows variability on a multitude of time scales. The central question of Chapter 4 is:

> Can atmospheric low-frequency variability excite a weakly damped AMO mode?

Here, weakly damped refers to the parameter range $\gamma < \gamma_H$, but for values of γ not too far away from the Hopf bifurcation. We speak of excitation when multidecadal variability related to the AMO mode occurs in this parameter range. In Chapter 4 we study the low-order ocean model with additional forcing from the low-order atmosphere model of Chapter 2.

Acknowledgements. This chapter is based on the joint paper *The dynamics of a low-order model for the Atlantic Multidecadal Oscillation* by Broer, Dijkstra, Simó, Sterk

and Vitolo (2010). The anonymous referee is kindly thanked for useful comments. The authors thank Leela Frankcombe (IMAU/UU) for making Figure 3.1.

AES is supported by the Netherlands Organisation for Scientific Research (NWO) by grant ALW 854.00.036. RV gratefully acknowledges support of the Willis Research Network.[2] The research of CS has been supported by grant MTM2006-05849/Consolider (Spain). The University of Barcelona is kindly thanked for its hospitality.

[2]http://www.willisresearchnetwork.com

Chapter 4

Excitation of the Atlantic Multidecadal Oscillation

4.1 Introduction

In Chapters 2 and 3 we have studied low-frequency dynamics of the atmosphere and ocean, treating them as isolated subsystems of the North Atlantic climate system. In this chapter we investigate the effect of deterministic atmospheric forcing on the AMO mode in its weakly damped regime.

4.1.1 Stochastic forcing in ocean models

A classical approach in the study of ocean-atmosphere interactions is to model the atmospheric forcing of the ocean by stochastic noise.

Preferred time scales. Hasselmann (1976) proposed a stochastic model to study climate variability. In this model he attributes climate variability to forcing of a slow subsystem (e.g., the ocean) with a noisy fast subsystem (e.g., weather). The slow subsystem acts as an integrator of white noise forcing which leads to a red noise response.

Saravanan and McWilliams (1998) point out that white or red noise spectra do not have preferred time scales, whereas realistic climate records do show preferred time scales. They show that spatially coherent patterns of variability can lead to preferred time scales of oceanic variability through spatial resonance. Their results do not require the existence of oscillatory modes in either the ocean or atmosphere.

Griffies and Tziperman (1995) studied a four-box ocean model of the thermohaline circulation which has one damped oscillatory eigenmode in addition to purely damped eigenmodes. They observed that stochastic forcing, modelling atmospheric 'weather,' can excite the oscillatory mode.

The effect of noise on Hopf bifurcations. Juel et al. (1997) studied the effect of noise on pitchfork and Hopf bifurcations by both physical experiments (using an electronic oscillator) and numerical integrations of normal forms. For parameter values slightly below the critical value for which a supercritical Hopf bifurcation occurs, they observed low-frequency variations in the form of correlated oscillations in the envelope of the time series. Moreover, they observed that noise can shift the critical value of the bifurcation parameter in both sub- and supercritical direction.

Stochastic excitation of the AMO. Dijkstra et al. (2008) and Frankcombe et al. (2009) studied the effect of stochastic forcing on the AMO mode. In their model the AMO mode appears through a supercritical Hopf bifurcation of a steady ocean flow when the forcing changes from restoring to prescribed heat flux (the scenario as described in §3.3.2). Stochastic noise excites the AMO mode in the sense that in the subcritical regime multidecadal variability with the spatio-temporal characteristics of the AMO mode occurs. Moreover, white noise only weakly excites the AMO mode, but the introduction of spatial and temporal coherence in the forcing increases the amplitude of the variability to levels corresponding with observations. The physical mechanism behind this excitation is explained in terms of rectification of a mean state: noise increases the time-mean meridional overturning circulation, making the time-mean state more unstable to the AMO mode.

4.1.2 Deterministic excitation of the AMO

In the low-order ocean model of Chapter 3 the AMO mode appears through a supercritical Hopf bifurcation when switching from restoring ($\gamma = 0$) to prescribed heat flux ($\gamma = 1$). Prescribed heat flux in ocean models is a strong idealisation since it amounts to net zero atmospheric damping. In reality sea surface temperature anomalies are substantially damped by the atmosphere. The central question of this chapter is:

> Can atmospheric low-frequency variability excite the weakly damped AMO mode?

Here, weakly damped refers to the parameter range $\gamma < \gamma_H$, but for values of γ not too far away from the Hopf bifurcation. We speak of excitation when multidecadal variability related to the AMO mode occurs in this parameter range.

We study the low-order ocean model of Chapter 3 with additional forcing from the low-order atmosphere model of Chapter 2. The resulting model should not be considered as a coupled ocean-atmosphere model, but rather as an ocean model with additional atmospheric forcing.

4.2 Model

In this section we derive a formula to parametrise a heat flux from the atmosphere model providing additive forcing in the ocean model.

4.2.1 The atmosphere and ocean models

We briefly recall the setup of the atmosphere model of Chapter 2 and the ocean model of Chapter 3.

Atmosphere. The low-order atmosphere model in Chapter 2 is derived from the 2-layer shallow water equations. The governing equations are given by a system of six partial differential equations for the eastward velocity u_ℓ, the northward velocity v_ℓ, and the thickness h_ℓ of each layer ($\ell = 1, 2$). The equations are formulated on a β–plane channel having dimensions $L_x^a = 29000$ km (longitude) and $L_y^a = 2500$ km (latitude). The model is forced by orography in the bottom layer and a zonal wind profile, of which the amplitudes are controlled by the parameters h_0 and U_0, respectively. The low-order model is a system of 46 ordinary differential equations.

Ocean. The low-order ocean model in Chapter 3 is derived from a model for thermally driven ocean flows in a 3-dimensional rectangular basin having dimensions $L_x^o = 6000$ km (longitude), $L_y^o = 6000$ km (latitude), and $L_z^o = 4$ km (depth). A system of five partial differential equations governs the evolution of the velocity field (u, v, w), the pressure p, and the temperature T. The thermal wind balance relates the velocity field to the temperature field.

Ocean flows are forced by a restoring heat flux Q_{rest}, which is proportional to the difference between the sea surface temperature and an idealised atmospheric temperature. The parameter Δ determines the equator-to-pole atmospheric temperature gradient. With restoring heat flux the ocean model has a stable equilibrium representing a steady ocean flow. From this equilibrium we compute the corresponding heat flux which we use as prescribed heat flux, which we denote by Q_{pres}. Finally, we define a new heat flux

$$Q_\gamma = (1 - \gamma)Q_{\text{rest}} + \gamma Q_{\text{pres}}, \tag{4.1}$$

which interpolates between restoring ($\gamma = 0$) and prescribed heat flux ($\gamma = 1$). The low-order model is a system of 27 ordinary differential equations.

4.2.2 Additive atmospheric forcing for the ocean

From the layer thickness fields h_ℓ of the low-order atmosphere model we parameterise a heat flux, which we use as additive forcing in the low-order ocean model. The resulting model should not be interpreted as a coupled ocean-atmosphere model, but as an ocean model with additional forcing by atmospheric low-frequency variability.

Heat flux. The downward heat flux Q_{oa} at the ocean-atmosphere interface is decomposed in a part independent of air-sea interaction ($\overline{Q}_{oa}$), and a part proportional to the difference in temperatures of the atmosphere and ocean at the interface. Hence,

$$Q_{oa} = \overline{Q}_{oa} + K_S(T_S^a - T), \tag{4.2}$$

where T_S^a is the atmospheric surface temperature and T is the sea surface temperature. To obtain a closed system of equations, the quantities $\overline{Q}_{oa}$ and T_S^a are parameterised from the variables of the atmosphere and ocean model.

Parameterisations. We parameterise the mean heat flux $\overline{Q}_{oa}$ by Q_γ defined in (4.1). As in Van der Avoird et al. (2002) we will model T_S^a as

$$T_S^a = \kappa T + (1-\kappa)T^a,$$

where T^a is the temperature at the interface between the two layers in the atmosphere and $0 \leq \kappa \leq 1$ is a non-dimensional coupling coefficient. By the thermal wind relation we have approximately

$$T^a = -\alpha(h_1 - h_2),$$

where $h_1 - h_2$ is related to the vertical pressure difference between the two layers. Hence, (4.2) becomes

$$Q_{oa} = Q_\gamma + K_S(\kappa - 1)[T + \alpha(h_1 - h_2)]. \tag{4.3}$$

Parameter		Value	
K_S	heat transfer coeffcient	40	[W m^{-2}]
α	coupling coefficient	1.0×10^{-3}	[K m^{-1}]
κ	coupling coefficient	0.8	[–]

Table 4.1. Values of the coupling parameters. For the values of the parameters of the atmosphere and ocean model see Tables 2.2 and 3.1.

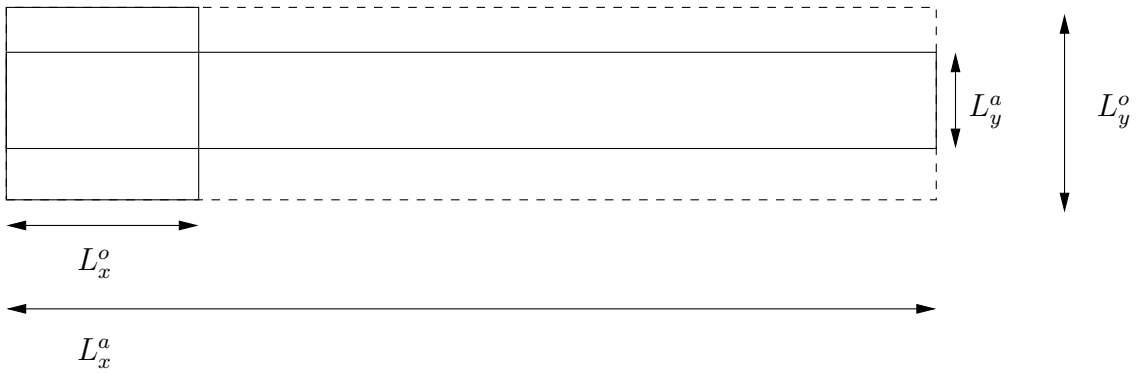

Figure 4.1. The atmospheric channel and the ocean basin are placed such that their western boundaries and their centre lines are aligned. In addition, the atmospheric channel is stretched in the meridional direction.

Galerkin projection of the heat flux. The projection of the first term in (4.3) already occurs as a term in the autonomous ocean model. We only need to compute the projection of the second term. Observe that in the meridional direction the atmospheric channel is smaller than the ocean basin. We solve this problem by aligning the line $y = 3000$ km of the ocean basin and the line $y = 1250$ km of the atmospheric channel and stretching the atmospheric channel, see Figure 4.1.

The surface heat flux will be distributed over a surface layer of the ocean having thickness H_m. The contribution of the second term in (4.3) in the equation for $\widehat{T}_{m,n,k}$ of the low-order ocean model can be written as

$$K_S(\kappa - 1) \iiint [T(x, y, z) + \alpha(h_1(x, y) - h_2(x, y))]c_m(x)c_n(y)c_k(z)dxdydz, \quad (4.4)$$

where the integral is computed over the box $[0, L_x^o]\times[0, L_y^o]\times[-H_m, 0]$. Since the fields h_ℓ and T are expanded in Fourier modes, this integral gives a linear combination of the state variables $\widehat{h}_\ell$ and $\widehat{T}_{p,q,r}$. The numerical coefficients in this linear combination are given by the integral of the product of two Fourier modes.

The low-order coupled system. Denote with $\widehat{A} \in \mathbb{R}^{46}$ and $\widehat{T} \in \mathbb{R}^{27}$ the state space variables of the atmosphere and ocean model, respectively. Then ocean model with atmospheric forcing can be symbolically written as the skew-coupled system:

$$\begin{aligned} \varepsilon \frac{\widehat{A}}{dt} &= F(\widehat{A}; U_0, h_0) \\ \frac{d\widehat{T}}{dt} &= G(\widehat{T}; \Delta, \gamma) + B(\widehat{T}, \widehat{A}). \end{aligned} \quad (4.5)$$

In these equations B is a bilinear operator which gives the contribution of the atmospheric heat flux according to (4.4). The parameter $\varepsilon = 1/60$ is needed to rescale the time scale of the atmosphere model to the time scale of the ocean model.

4.3 Results

In this section we study how the AMO mode is excited by chaotic forcing from the low-order atmosphere model, and we give a preliminary explanation in terms of intermittency.

4.3.1 Excitation of the AMO

The parameters of the autonomous ocean model ($K_S = 0$ W m^{-2}) are fixed at $\Delta = 20$°C and $\gamma = 0.90$, for which a steady ocean flow appears. A supercritical Hopf bifurcation at $\gamma_H = 0.951$ gives rise to the AMO mode. Next, we force the ocean model with a time-dependent heat flux computed from the intermittent strange attractor of the atmosphere, see Figure 4.2 ($K_S = 40$ W m^{-2}). This strange attractor has a significant amount of spectral power of several months up to years. It is to be expected that for sufficiently small values of K_S hyperbolic attractors of the autonomous ocean model persist as non-autonomous analogues in the skew-coupled model and that transversality properties persist in some form.

Using the formerly existing equilibrium as an initial condition, we obtain irregular oscillatory behaviour in the state variables of the ocean model. The top panel of

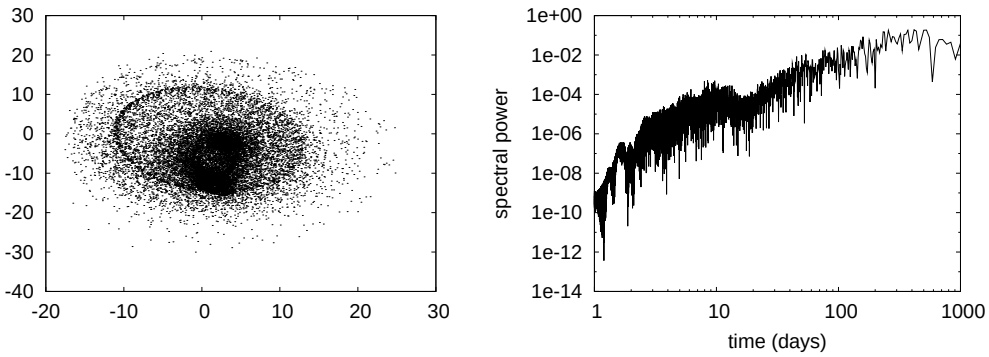

Figure 4.2. Strange attractor and its power spectrum ($U_0 = 15$ m s^{-1} and $h_0 = 800$ m). This attractor occurs in the atmosphere model after a stable periodic orbit disappears through a saddle-node bifurcation. See §2.3.2 for details.

γ	max. SST	min. SST	time scale	maximum spectral power
0.90	14.03	13.84	39.5 years	3.39×10^{-6}
0.91	14.01	13.81	39.5 years	4.47×10^{-6}
0.92	13.98	13.78	39.5 years	6.18×10^{-6}
0.93	13.95	13.73	39.5 years	9.12×10^{-6}
0.94	13.91	13.68	39.5 years	1.47×10^{-5}
0.95	13.87	13.61	39.5 years	2.74×10^{-5}

Table 4.2. Maximum and minimum values of the basin averaged sea surface temperature for different values of γ computed over a time span of 4000 years. Maximal spectral power and the corresponding period.

Figure 4.3 shows a time series of the basin averaged sea surface temperature. This time series shows high-frequency fluctuations which are due to the fast variability of the atmosphere, but one can also observe a slower time scale. This is confirmed by computing both a 10-year running average (middle panel) and a power spectrum (bottom panel). The power spectrum shows that the multidecadal time scales have a significant amount of power.

Closer to the Hopf bifurcation the multidecadal peak of the power spectrum becomes stronger, see Figure 4.4. The maximum and minimum values of the basin averaged sea surface temperature decrease, but their difference remains nearly constant (see Table 4.2).

For clarity, Figure 4.3 and Figure 4.4 only show a part of a time series computed up to 5000 years. Time series computed up to 20000 years show that the oscillatory behaviour does not decay after some time.

4.3.2 Preliminary interpretation

Chaotic atmospheric forcing causes high-frequency, irregular fluctuations in the state variables of the ocean model. Despite this irregularity the power spectrum still reveals a preferred time scale as a distinct peak at 39 years. Hence, the following question arises:

> What causes the distinct decadal time scale in the irregular fluctuations of the oceanic variables?

The main idea is the following. The atmospheric forcing does not cause the ocean variables to wander randomly through state space, but they move in preferred directions which are determined by the stable manifolds of the formerly existing

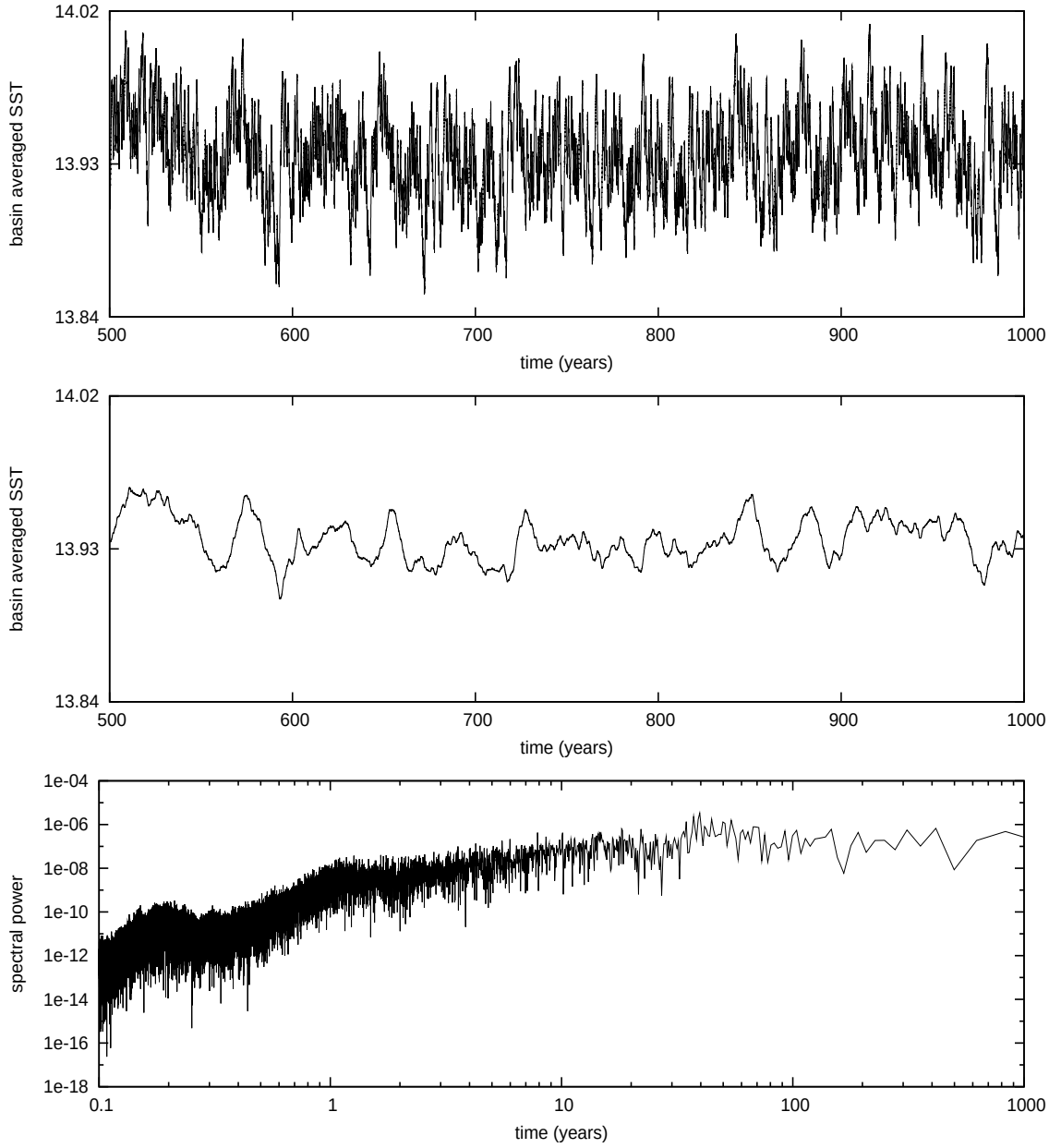

Figure 4.3. Induced multidecadal variability for $\gamma = 0.90$. Top: basin averaged sea surface temperature as a function of time. Middle: 10-year running mean of the time series in the top panel. Bottom: power spectrum.

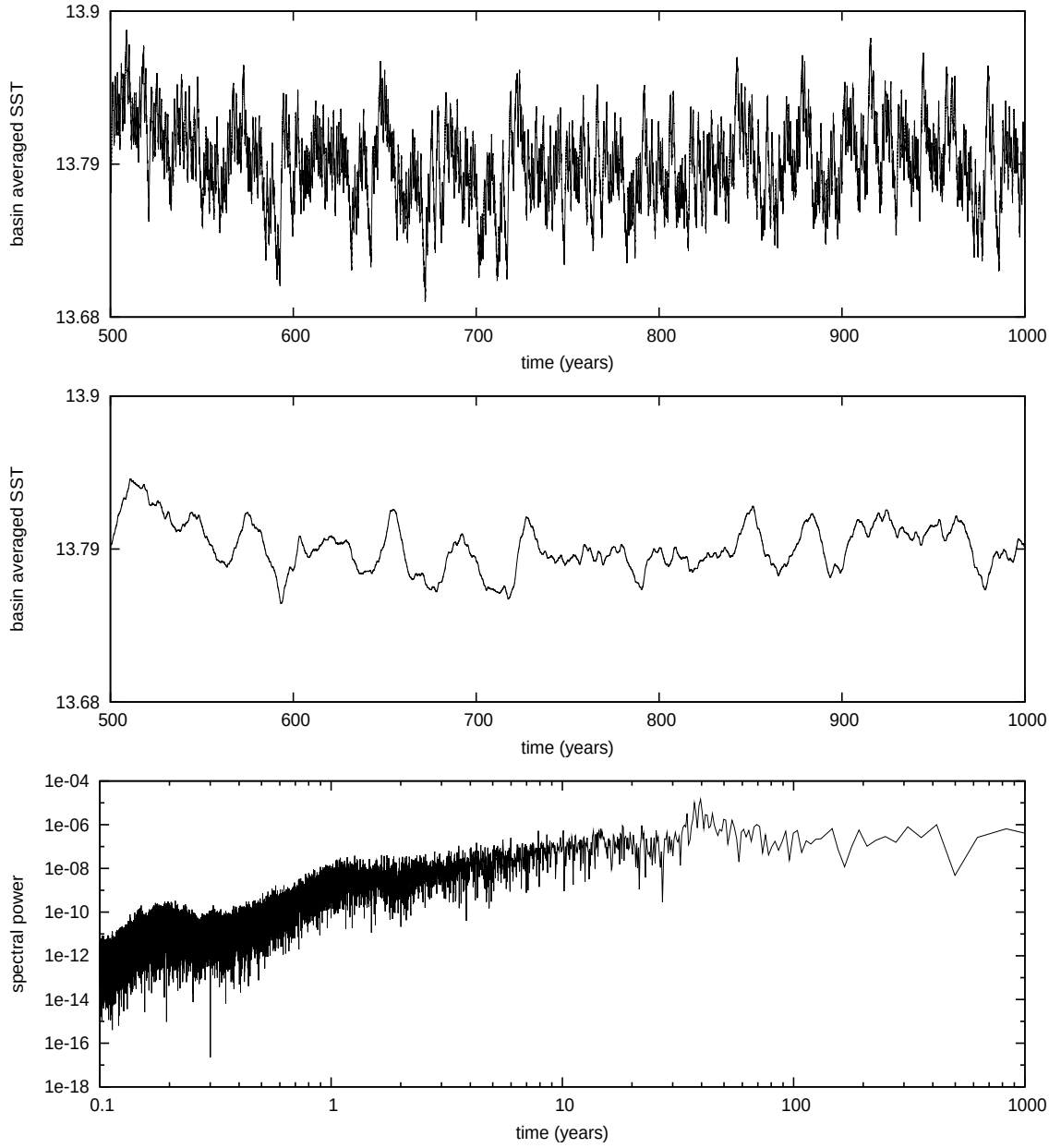

Figure 4.4. The same as Figure 4.3 but for $\gamma = 0.94$.

equilibrium. Loosely speaking, the 'ghost' of the formerly existing nearby Hopf bifurcation still influences the dynamics.

To fix thoughts, consider again the autonomous ocean model. For $\Delta = 20°\text{C}$ and $0.90 \leq \gamma < \gamma_H = 0.951$ the model has a stable equilibrium. Hence, the Jacobian matrix of the vector field linearised around this equilibrium only has eigenvalues with negative real part. The least stable eigenvalue (i.e., the eigenvalue closest to the imaginary axis) is complex and its imaginary part corresponds with a time scale of approximately 40 years. Denote with $\mathbf{\Phi}_1 \pm i\mathbf{\Phi}_2$ eigenvectors associated with the least stable eigenvalue. Note that they depend on γ, but this is supressed in the notation.

Define the subspace

$$\mathcal{M} = \text{span}\,\{\mathbf{\Phi}_1, \mathbf{\Phi}_2\}.$$

At the Hopf bifurcation ($\gamma = \gamma_H$) the subspace $\mathcal{M}$ is precisely the tangent plane to the centre manifold. Let $P_{\mathcal{M}}$ be the orthogonal projection from the ocean state space $\mathbb{R}^{27}$ onto the subspace $\mathcal{M}$. The ratio

$$\rho(t) = \frac{\|P_{\mathcal{M}}\widehat{T}(t)\|_2}{\|\widehat{T}(t)\|_2}$$

measures how well the ocean state variable $\widehat{T}$ projects onto the subspace spanned by the eigenvectors of the least stable eigenvalue. Time series of the ratio ρ for different values of γ are shown in Figure 4.5. Indeed, it is evident that ρ becomes larger when γ is moved towards the Hopf bifurcation.

4.4 Discussion

The results presented in this chapter show that the AMO mode can be excited for $\gamma < \gamma_H$ by atmospheric forcing. Moreover, closer to the Hopf bifurcation the multidecadal variability becomes more pronounced. These results are in agreement with those of Dijkstra et al. (2008) and Frankcombe et al. (2009). Also their interpretation in terms of rectification of the time-mean state is applicable here: the meridional overturning circulation of the time-mean state is stronger than that of the equilibrium (not shown).

Excitation versus amplification. On the other hand, the results in this chapter are very different from the results obtained with annual forcing in §3.3.3. With annual forcing the dynamics is either periodic or quasi-periodic, whereas chaotic forcing causes highly irregular fluctuations in the ocean state variables. A second difference

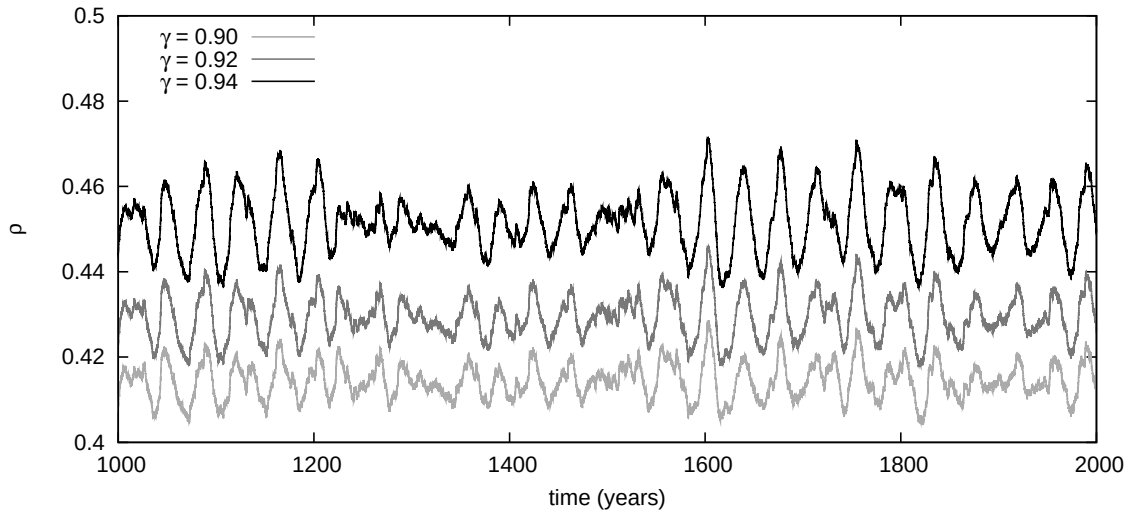

Figure 4.5. Time series of the ratio ρ for three values of γ.

is that purely periodic forcing only amplifies the AMO mode (see Figure 3.13). The AMO mode is, however, not excited because the Hopf-Neĭmark-Sacker bifurcation takes place for almost the same parameter value as the orginal Hopf bifurcation of the autonomous system.

Intermittency scenarios. The preliminary results of this chapter provide a starting point for future research. In particular, the following question should be addressed:

> What is the reason for the occurrence of the oscillatory behaviour in Figure 4.5?

We only have given an interpretation in terms of 'preferred directions' in which the ocean variables move due to formerly existing stable manifolds, i.e., how the 'ghost' of the formerly existing nearby Hopf bifurcation still influences the dynamics. Such behaviour is possibly related to intermittency, but of which form is not yet clear.

The classical intermittency scenario described by Pomeau and Manneville (1980) involves the bifurcation of a periodic orbit. For example, type I intermittency occurs when a periodic orbit disappears through a saddle-node bifurcation and when the global dynamics causes typical evolutions to return to the position of the formerly existing periodic orbit. In this situation time series of the evolutions show switching between periodic and chaotic behaviour. An example of this type of intermittency is discussed in §2.3.2 (see Figures 2.10 and 2.10). Other types of intermittency are related to period doubling bifurcations or Hopf-Neĭmark-Sacker bifurcations.

The scenarios described by Pomeau and Manneville all involve a codimension-1 bifurcation. In this chapter (at least) two parameters must be tuned: the parameter γ must be near the critical value of the Hopf bifurcation and the parameter K_S must be nonzero. Possibly, our results can be explained by intermittency scenario's related to bifurcations of higher codimension.

For a detailed investigation a model with a lower-dimensional state space is more convenient. That is, we should develop 'models of models.' One possibility is to study the normal form of a Hopf bifurcation coupled to suitable dynamical systems with a chaotic attractor.

Appendix A

Derivation of the low-order models

The Galerkin projection of a partial differential equation (PDE) amounts to an expansion of the unknown fields in a truncated series of orthogonal functions with time-dependent coefficients. Ordinary differential equations for the coefficients are derived by substituting the truncated expansions in the PDE and taking the innerproduct with the basis functions.

A.1 Basis functions

As basis functions we use the solutions of the following Sturm–Liouville eigenvalue problems on a bounded interval $[0, a]$:

$$\frac{d^2 f}{dx^2} = \lambda f(x), \quad f(0) = f(a) = 0, \tag{A.1}$$

$$\frac{d^2 f}{dx^2} = \lambda f(x), \quad f'(0) = f'(a) = 0, \tag{A.2}$$

$$\frac{d^4 f}{dx^4} = \lambda f(x), \quad f(0) = f'(0) = f(a) = f'(a) = 0. \tag{A.3}$$

The solutions of (A.1) and (A.2) are the usual Fourier modes with half wave numbers:

$$s_k(x; a) = \sqrt{\frac{2}{a}} \sin(\mu_k x), \quad c_k(x; a) = \begin{cases} \sqrt{\dfrac{1}{a}} & \text{if } k = 0, \\ \sqrt{\dfrac{2}{a}} \cos(\mu_k x) & \text{if } k \neq 0, \end{cases}$$

where $\mu_k = k\pi/a$ and the eigenvalues are given by $\lambda_k = -\mu_k^2$. The functions s_k and c_k are orthonormal with respect to the standard innerproduct. The solutions of

(A.3) are the so-called 'beam functions,' which are given by

$$b_k(x;a) = \cosh(\mu_k x) - \cos(\mu_k x) - \frac{\cosh(\mu_k a) - \cos(\mu_k a)}{\sinh(\mu_k a) - \sin(\mu_k a)}\{\sinh(\mu_k x) - \sin(\mu_k x)\},$$

where the numbers μ_k are given by the positive roots of the equation

$$\cos(\mu a) = \frac{1}{\cosh(\mu a)},$$

and the eigenvalues are given by $\lambda_k = \mu_k^4$. The functions b_k form an orthogonal family.

In the following sections we simplify the notation for the functions $s_k(x;a)$, $c_k(x;a)$, and $b_k(x;a)$ by omitting the end point a. The upper limits of the integration signs indicate the value of a.

A.2 The low-order atmosphere model

To simplify the notation we omit subscripts of the summation signs: all index pairs (p,q) and (r,s) run through the set

$$R_A = \{\, (m,n) \mid m \in \{0,3\}, n \in \{0,1,2\} \,\},$$

see §2.2.2. All projections are derived similarly, and therefore we only give the projection of the equation for $\widehat{u}_\ell$ onto the basis function $c_{2m}(x)c_n(y)$:

$$\begin{aligned}
\frac{d\widehat{u}^c_{1,m,n}}{dt} = F_{m,n} &- \sum \{H^c_{(p,q),(m,n)}(\widehat{h}^c_{1,p,q} + \widehat{h}^c_{2,p,q}) + H^s_{(p,q),(m,n)}(\widehat{h}^s_{1,p,q} + \widehat{h}^s_{2,p,q}) \\
&\qquad + C^c_{(p,q),(m,n)}\widehat{v}^c_{1,p,q} + C^s_{(p,q),(m,n)}\widehat{v}^s_{1,p,q} \\
&\qquad + D^c_{(p,q),(m,n)}\widehat{u}^c_{1,p,q} + D^s_{(p,q),(m,n)}\widehat{u}^s_{1,p,q}\} \\
&- \sum\sum \{A^{cc}_{(p,q),(r,s),(m,n)}\widehat{u}^c_{1,p,q}\widehat{u}^c_{1,r,s} + A^{cs}_{(p,q),(r,s),(m,n)}\widehat{u}^c_{1,p,q}\widehat{u}^s_{1,r,s} \\
&\qquad + A^{sc}_{(p,q),(r,s),(m,n)}\widehat{u}^s_{1,p,q}\widehat{u}^c_{1,r,s} + A^{ss}_{(p,q),(r,s),(m,n)}\widehat{u}^s_{1,p,q}\widehat{u}^s_{1,r,s} \\
&\qquad + B^{cc}_{(p,q),(r,s),(m,n)}\widehat{v}^c_{1,p,q}\widehat{u}^c_{1,r,s} + B^{cs}_{(p,q),(r,s),(m,n)}\widehat{v}^c_{1,p,q}\widehat{u}^s_{1,r,s} \\
&\qquad + B^{sc}_{(p,q),(r,s),(m,n)}\widehat{v}^s_{1,p,q}\widehat{u}^c_{1,r,s} + B^{ss}_{(p,q),(r,s),(m,n)}\widehat{v}^s_{1,p,q}\widehat{u}^s_{1,r,s}\} .
\end{aligned}$$

Set $a = L_x/L$ and $b = L_y/L$.

Constant terms. The projection of the zonal wind and orography terms give the linear terms in the low-order model:

$$F_{m,n} = \sigma\mu\alpha_1 U_0 U^{-1}\sqrt{ab}\int_0^a c_0(x)c_{2m}(x)dx\int_0^b c_0(y)c_n(y)dy$$
$$- \sigma\mu\alpha_1 U_0 U^{-1}\sqrt{ab/2}\int_0^a c_0(x)c_{2m}(x)dx\int_0^b c_2(y)c_n(y)dy$$
$$- h_0 D^{-1}\sqrt{ab/2}\int_0^a c_6'(x)c_{2m}(x)dx\int_0^b c_0(y)c_n(y)dy.$$

Linear terms. The linear terms arise from the projection of the pressure gradient terms, the Coriolis force terms, and the dissipation terms. The projection of the pressure gradient gives the coefficients

$$H^c_{(p,q),(m,n)} = F\frac{\rho_1}{\rho_0}\int_0^a c_{2p}'(x)c_{2m}(x)dx\int_0^b c_q(y)c_n(y),$$

and the projection of the Coriolis force gives the coefficients

$$C^c_{(p,q),(m,n)} = Ro^{-1}\int_0^a c_{2p}(x)c_{2m}(x)dx\int_0^b s_q(y)c_n(y)dy$$
$$+ \beta\int_0^a c_{2p}(x)c_{2m}(x)dx\int_0^b s_q(y)c_n(y)ydy.$$

Finally, the projection of the dissipation terms gives the coefficients

$$D^c_{(p,q),(m,n)} = Ro^{-1}E_H\int_0^a c_p''(x)c_{2m}(x)dx\int_0^b c_q(y)c_n(y)dy$$
$$- \sigma(\mu + \delta_{\ell,2}r)\int_0^a c_p(x)c_{2m}(x)dx\int_0^b c_q(y)c_n(y)dy.$$

The coefficients H^s, C^s, and D^s have similar expressions, in which the basis function $c_{2p}(x)$ is replaced with the basis function $s_{2p}(x)$.

Quadratic terms. The quadratic terms in the low-order model arise from the projection of the advection terms in the shallow-water equations. The coefficients for the

quadratic terms are given by

$$
\begin{aligned}
A^{cc}_{(p,q),(r,s),(m,n)} &= \int_0^a c_{2p}(x)c'_{2r}(x)c_{2m}(x)dx \int_0^b c_q(y)c_s(y)c_n(y)dy,\\
A^{cs}_{(p,q),(r,s),(m,n)} &= \int_0^a c_{2p}(x)s'_{2r}(x)c_{2m}(x)dx \int_0^b c_q(y)c_s(y)c_n(y)dy,\\
A^{sc}_{(p,q),(r,s),(m,n)} &= \int_0^a s_{2p}(x)c'_{2r}(x)c_{2m}(x)dx \int_0^b c_q(y)c_s(y)c_n(y)dy,\\
A^{ss}_{(p,q),(r,s),(m,n)} &= \int_0^a s_{2p}(x)s'_{2r}(x)c_{2m}(x)dx \int_0^b c_q(y)c_s(y)c_n(y)dy,
\end{aligned}
$$

with similar expressions for the coefficients B, in which the basis function $c_q(y)$ is replaced with the basis function $s_q(y)$.

A.3 The low-order ocean model

To simplify the notation we omit subscripts of the summation signs by making the following convention. Indices of the vectors $\widehat{T}$ run through the set R_T, and indices of the vectors $\widehat{\psi}$ and $\widehat{\phi}$ run through the set R_S, where

$$
\begin{aligned}
R_T &= \{\, (m,n,k) \mid m,n,k \in \{0,1,2\} \,\},\\
R_S &= \{\, (m,n,k) \mid m,n,k \in \{1,2\} \,\},
\end{aligned}
$$

see §3.2.2.

The thermal wind balance. After substitution of the stream functions, the thermal wind balance becomes

$$
-E_H\left(\frac{\partial^3\psi}{\partial x^2\partial z}+\frac{\partial^3\psi}{\partial y^2\partial z}\right)-E_V\frac{\partial^3\psi}{\partial z^3}+\frac{\partial\phi}{\partial z} = \frac{\partial p}{\partial x}, \tag{A.4}
$$

$$
E_H\left(\frac{\partial^3\phi}{\partial x^2\partial z}+\frac{\partial^3\phi}{\partial y^2\partial z}\right)+E_V\frac{\partial^3\phi}{\partial z^3}+\frac{\partial\psi}{\partial z} = \frac{\partial p}{\partial y}, \tag{A.5}
$$

$$
Ra\,T = \frac{\partial p}{\partial z}. \tag{A.6}
$$

These equations are called *diagnostic* since they do not contain any time-derivatives. The Galerkin projections of these equations are linear algebraic equations from which

$\widehat{\psi}$ and $\widehat{\phi}$ can be solved in terms of $\widehat{T}$:

$$\begin{aligned}\sum M_{(p,q,r),(m,n,k)}\widehat{\psi}_{p,q,r} - C_{(p,q,r),(m,n,k)}\widehat{\phi}_{p,q,r} &= f_{m,n,k},\\ \sum M_{(p,q,r),(m,n,k)}\widehat{\phi}_{p,q,r} + C_{(p,q,r),(m,n,k)}\widehat{\psi}_{p,q,r} &= g_{m,n,k}.\end{aligned}$$

In these equations, the coefficients due to mixing of momentum are given by

$$\begin{aligned}M_{(p,q,r),(m,n,k)} = E_H &\int_0^1 b_p''(x)b_m(x)dx \int_0^1 b_q(y)b_n(y)dy \int_{-1}^0 s_r'(z)s_k'(z)dz\\ &+ E_H \int_0^1 b_p(x)b_m(x)dx \int_0^1 b_q''(y)b_n(y)dy \int_{-1}^0 s_r'(z)s_k'(z)dz\\ &+ E_V \int_0^1 b_p(x)b_m(x)dx \int_0^1 b_q(y)b_n(y)dy \int_{-1}^0 s_r'''(z)s_k'(z)dz\end{aligned}$$

and the coefficients due to the Coriolis force are given by

$$C_{(p,q,r,),(m,n,k)} = \int_0^1 b_p(x)b_m(x)dx \int_0^1 b_q(y)b_n(y)dy \int_{-1}^0 s_r'(z)s_k'(z)dz.$$

Finally, the coefficients of the right hand side are given by

$$\begin{aligned}f_{m,n,k} &= -Ra\sum \widehat{T}_{p,q,r} \int_0^1 c_p(x)b_m'(x)dx \int_0^1 c_q(y)b_n(y)dy \int_{-1}^0 c_r(z)s_k(z)dz,\\ g_{m,n,k} &= \quad Ra\sum \widehat{T}_{p,q,r} \int_0^1 c_p(x)b_m(x)dx \int_0^1 c_q(y)b_n'(y)dy \int_{-1}^0 c_r(z)s_k(z)dz.\end{aligned}$$

Observe that the pressure gradient is eliminated in the projected equations. Indeed, by performing an integration by parts the pressure gradient vanishes since a gradient is orthogonal to a divergence-free field with a vanishing normal component at the boundary.

The advection equation. After substitution of the stream functions, the advection equation is given by

$$\begin{aligned}\frac{\partial T}{\partial t} - \frac{\partial \psi}{\partial z}\frac{\partial T}{\partial x} + \frac{\partial \phi}{\partial z}\frac{\partial T}{\partial y} + \left(\frac{\partial \psi}{\partial x} - \frac{\partial \phi}{\partial y}\right)\frac{\partial T}{\partial z} = P_H\left(\frac{\partial^2 T}{\partial x^2} + \frac{\partial^2 T}{\partial y^2}\right) + P_V\frac{\partial^2 T}{\partial z^2}\\ + B(T_S - (T + T_0))g(z).\end{aligned}$$

This equation is called *prognostic* since it does contain a time-derivative. The Galerkin projection of this equation is a system of ordinary differential equations

with quadratic nonlinearities for the time-dependent expansion coefficients of the temperature field:

$$\frac{d\widehat{T}_{m,n,k}}{dt} = \sum A_{(p,q,r),(h,i,j),(m,n,k)}\widehat{\psi}_{p,q,r}\widehat{T}_{h,i,j} + B_{(p,q,r),(h,i,j),(m,n,k)}\widehat{\phi}_{p,q,r}\widehat{T}_{h,i,j} + D_{m,n,k}\widehat{T}_{m,n,k} + \sum F_{(p,q,r),(m,n,k)}(\widehat{T}_{S,p,q,r} - \widehat{T}_{p,q,r}).$$

In this equation, the coefficient $A_{(p,q,r),(h,i,j),(m,n,k)}$ equals

$$\int_0^1 b_p'(x)c_h(x)c_m(x)dx \int_0^1 b_q(y)c_i(y)c_n(y)dy \int_{-1}^0 s_r(z)c_j'(z)c_k(z)dz - \int_0^1 b_p(x)c_h'(x)c_m(x)dx \int_0^1 b_q(y)c_i(y)c_n(y)dy \int_{-1}^0 s_r'(z)c_j(z)c_k(z)dz,$$

and the coefficient $B_{(p,q,r),(h,i,j),(m,n,k)}$ equals

$$\int_0^1 b_p(x)c_h(x)c_m(x)dx \int_0^1 b_q(y)c_i'(y)c_n(y)dy \int_{-1}^0 s_r'(z)c_j(z)c_k(z)dz - \int_0^1 b_p(x)c_h(x)c_m(x)dx \int_0^1 b_q'(y)c_i(y)c_n(y)dy \int_{-1}^0 s_r(z)c_j'(z)c_k(z)dz.$$

The dissipation coefficients are given by

$$D_{m,n,k} = -\pi^2\left[P_H(m^2+n^2) + P_V k^2\right].$$

Finally, the coefficients of the forcing terms are given by.

$$F_{(p,q,r),(m,n,k)} = B\int_0^1 c_p(x)c_m(x)dx \int_0^1 c_q(y)c_n(y)dy \int_{-1}^0 c_r(z)c_k(z)g(z)dz.$$

Appendix B

Numerical methods

We study the low-order models with numerical tools which are briefly described in this appendix. We mainly used AUTO–07p (Doedel and Oldeman, 2007) to compute the bifurcation curves of equilibria and periodic orbits. Most of the theoretical and computational aspects behind this software are described by Kuznetsov (2004). We have written tailored software for numerical integration and the computation of Lyapunov exponents. The algorithms are sketched in the sections below.

B.1 The Taylor integrator

The low-order models of Chapters 2 and 3 are systems of ordinary differential equations with quadratic nonlinearities:

$$\frac{dx_i}{dt} = C_i + \sum_{j=1}^{d} L_{ij} x_j + \sum_{j,k=1}^{d} Q_{ijk} x_j x_k, \quad i = 1, \ldots, d, \tag{B.1}$$

where d is the dimension of the state space ($d = 46$ for the atmosphere, and $d = 27$ for the ocean). Typically, the constant terms represent forcing terms, the linear terms represent dissipation and Coriolis forces, and the quadratic terms are due to the nonlinear advection terms.

The system (B.1) is integrated numerically using a truncated Taylor expansion of the solution around time t_0:

$$x_i(t_0 + h) = \sum_{n=0}^{N} x_i^{[n]}(t_0) h^n + O(h^{N+1}),$$

where the coefficients are given by

$$x_i^{[n]}(t_0) = \frac{1}{n!} \frac{d^n x_i}{dt^n}(t_0). \tag{B.2}$$

Given a point $x_i^{[0]}(t_0)$, which is either an initial condition or a previously computed point on the trajectory, we first compute

$$x_i^{[1]} = C_i + \sum_{j=1}^{d} L_{ij} x_j^{[0]} + \sum_{j,k=1}^{d} Q_{ijk} x_j^{[0]} x_k^{[0]}.$$

Then, for $n > 0$, we have the recurrent relation

$$x_i^{[n+1]} = \frac{1}{n+1} \left(\sum_{j=1}^{d} L_{ij} x_j^{[n]} + \sum_{j,k=1}^{d} \sum_{m=0}^{n} Q_{ijk} x_j^{[m]} x_k^{[n-m]} \right),$$

which follows by substituting the truncated Taylor series in (B.1) using the Leibniz rule for differentiation of products.

We have chosen a tolerance $\epsilon = 10^{-16}$ which gives $N = 20$ as the optimal order. The step size is computed as $h = \min\{h_1, h_2\}$, where

$$h_1 = \exp\left\{ \frac{1}{N-1} \log\left(\epsilon \frac{\left\| x^{[1]} \right\|_\infty}{\left\| x^{[N]} \right\|_\infty} \right) \right\},$$
$$h_2 = \exp\left\{ \frac{1}{N-2} \log\left(e^2 \epsilon \frac{\left\| x^{[1]} \right\|_\infty}{\left\| x^{[N-1]} \right\|_\infty} \right) \right\}.$$

A very convenient aspect of the Taylor integration method is the possibility of producing dense output by just evaluating the Taylor polynomial at time $t + h'$ for any desired value of $h' < h$; the cost of evaluating the Taylor polynomial is negligible in comparison to the computation of the coefficients.

The reader is referred to Jorba and Zou (2005) for a detailed discussion on the Taylor method and a ready-to-use implementation.

B.2 Power spectra

From the numerical integration of a vector field we obtain a scalar time series $(c_k)_{k=0}^{N-1}$ by computing some observable of the state vectors for which we usually take the Euclidean norm. From this time series we compute a discrete Fourier transform (DFT) by

$$\widehat{c}_k = \frac{1}{N} \sum_{n=0}^{N-1} c_n \exp\left(-2\pi i \frac{nk}{N} \right). \tag{B.3}$$

The power spectrum is, by definition, a plot of $|\widehat{c}_k|^2$ as a function of the Fourier frequency $f_k = k/N$.

Before computing a power spectrum, we subtract the mean from the time series:

$$u_k = c_k - \frac{1}{N}\sum_{n=0}^{N-1} c_n.$$

Moreover, we apply a Hamming window to reduce leakage of frequencies. Define the array $(H_k)_{k=0}^{N-1}$ by

$$H_k = 0.54 - 0.46\cos\left(\frac{2\pi k}{N}\right),$$

and set $v_k = H_k u_k$. We compute a DFT of the array $(v_k)_{k=0}^{N-1}$, and we normalise the resulting array $(\widehat{v}_k)_{k=0}^{N-1}$ by dividing by the norm of the array $(H_k)_{k=0}^{N-1}$.

All frequencies are computed modulo 1. Due to the discrete sampling procedure, all other frequencies are shifted within the interval $[0, 1)$, a phenomenon referred to as aliasing. Moreover, since our time series is real-valued, its DFT is symmetric around the frequency $f = 1/2$. Indeed, from (B.3) it follows that $\widehat{c}_{N-k} = \widehat{c}_k^*$.

The DFT is computed by means of a fast Fourier transform implemented in the FFTW library (Frigo and Johnson, 2005).

B.3 Lyapunov exponents

We compute Lyapunov exponents using the algorithm described by Benettin et al. (1980a,b), using refinements described by Broer and Simó (1998) and Simó (1990, 2005). For alternative methods to compute Lyapunov exponents, see Dieci et al. (1997) and Dieci (2002).

B.3.1 Lyapunov exponents of the atmosphere model

We start by computing a transient of $T_{\text{trans}} = 10^4$ units. During the integration it is checked if the orbit converges to an equilibrium or a periodic attractor.

Lyapunov exponents of equilibria and periodic orbits. To detect a stable equilibrium it is checked whether the the norm of the vector field remains less than 10^{-6} for 50 consecutive integration steps. If an equilibrium x_e is detected, then the Lyapunov exponents are given by $\operatorname{Re}\lambda$, where λ is an eigenvalue of the matrix $D_x f(x_e)$.

To detect a stable periodic orbit it is checked whether a locally defined Poincaré map P has a fixed point. If such a fixed point x_f is detected, then the Lyapunov

exponents are given by $\log|\lambda|/T_p$, where λ is an eigenvalue of the matrix $D_x P(x_f)$ and T_p is the period of the periodic orbit.

Lyapunov exponents of general orbits. If no equilibrium or periodic orbit is detected, we compute Lyapunov exponents by integrating the variational equations. Let $x(0)$ denote the initial condition of the vector field.

To compute the first k Lyapunov exponents we choose at random a set of k orthonormal vectors $v_i(0), i = 1, \ldots, k$. Then we simultaneously integrate the vector field and the first variational equations:

$$\begin{aligned} \frac{dx}{dt} &= f(x), \\ \frac{dv_i}{dt} &= D_x f(x(t))v_i, \quad i = 1, \ldots, k. \end{aligned} \tag{B.4}$$

Starting from the initial condition, we integrate (B.4) for T time units, which gives the vectors $x(T)$ and $v_i(T)$.

During the integration the vectors $v_i(t)$ align themselves along the direction of maximal expansion (or minimal compression). To prevent the vectors v_i from collapsing onto one we apply Gram–Schmidt orthonomalisation. The vectors $v_i(T)$ are orthogonalised (not yet normalised), which give vectors $w_i(T)$. Next, we integrate again for T time units using $x(T)$ and the normalised vectors $w_i(T)/\left\|w_i(T)\right\|_2$ as initial conditions. Repeating this procedure N times gives the following estimate for the Lyapunov exponents:

$$\lambda_i = \frac{1}{NT}\sum_{n=1}^{N} \log\left\|w_i(nT)\right\|_2, \quad i = 1, \ldots, k. \tag{B.5}$$

In the computations we have used $T = 10$ and $N \leq 1000$.

Projection of attractors. Attractors of Chapter 2 are plotted by projecting them onto a subspace V in which the orbits undergo maximal expansion (or minimal compression). This subspace can be obtained by integrating the variational equations. Assume that v_1 and v_2 are orthonormal basis vectors for V. The projection of an orbit $x(t)$ onto V is then given by

$$P_V x(t) = \langle x(t), v_1\rangle\, v_1 + \langle x(t), v_2\rangle\, v_2$$

and the plots of Chapter 2 are just plots of $\langle x(t), v_1\rangle$ versus $\langle x(t), v_2\rangle$.

B.3.2 Lyapunov exponents of the ocean model

After a transient of L iterates of the Poincaré map P, let $x^{(0)}$ be the current point on the orbit. In order to compute k Lyapunov exponents, we randomly generate a set of orthonormal vectors ξ_j $(j = 1, \ldots, k)$. The differential of the Poincaré map is applied to the ξ_j obtaining the vectors $\eta_j = DP(x^{(0)})\xi_j$. The vectors η_j are orthogonalised (not yet normalised) to obtain vectors ζ_j. The vectors ζ_j are normalised to obtain the new vectors ξ_j and a new point is computed on the orbit: $x^{(1)} = P(x^{(0)})$. The process is iterated up to a maximum of N iterates. From this procedure we compute the so-called *Lyapunov sums*

$$S_j(n) = \sum_{i=1}^{n} \log \|\zeta_j(n)\|_2$$

as a function of the number of iterations n.

The Lyapunov exponents are computed as the limit slopes of the sequences $S_j(n)$ as follows. Every M iterates of the Poincaré map we compute a linear fit for the points $(n, S_j(n))$ based on the last fraction α_i $(i = 1, 2, 3)$ of the iterations; this gives the slopes $s_j^{(i)}$. We stop the computations if either the maximum number of iterations N is exceeded or when the slopes satisfy

$$\Delta := \max_{j=1,\ldots,k} \{|s_j^{(1)} - s_j^{(2)}|, |s_j^{(3)} - s_j^{(2)}|\} < \mu,$$

where μ is a given tolerance. The last computed $s_j^{(2)}$ are used as estimates for the Lyapunov exponents and the last value of Δ is used as an estimate for the error. Typical values used in the computations are

$$k = 3,\ L = 10^5,\ M = 10^4,\ N = 10^6,\ \alpha_1 = 0.2,\ \alpha_2 = 0.4,\ \alpha_3 = 0.6.$$

Detecting quasi-periodic doublings. The computation is especially delicate if Lyapunov exponents are used to detect period doubling of invariant curves, because then the error should be small. The values in Table 3.2 are obtained with the values of parameters given above and typical errors in the Lyapunov exponents are $\approx 10^{-6}$. This is checked by repeating computations with different random seeds. Figure B.1 shows the estimated behaviour of the accumulation of γ_n to a limit value, the evidence of the existence of strange attractors shortly after the limit and the different bifurcations in a suitable scale.

Finally, we consider it also relevant to display the behaviour of the Lyapunov sums as a function of the number of iterates. In the reducible case (Jorba, 2001;

Broer and Simó, 1998; Vitolo et al., 2010) we can expect the typical pattern of a linear system modulated by a quasi-periodic change of variables. This is what can be guessed from Figure B.2 left, which corresponds to $\gamma \approx \gamma_4$. Similar patterns are seen for smaller values of γ. For larger γ, as in Figure B.2 right for $\gamma \approx \gamma_{10}$, slightly wilder patterns are detected. They become very wild beyond the end of the cascade, see Figure B.2 (bottom panel).

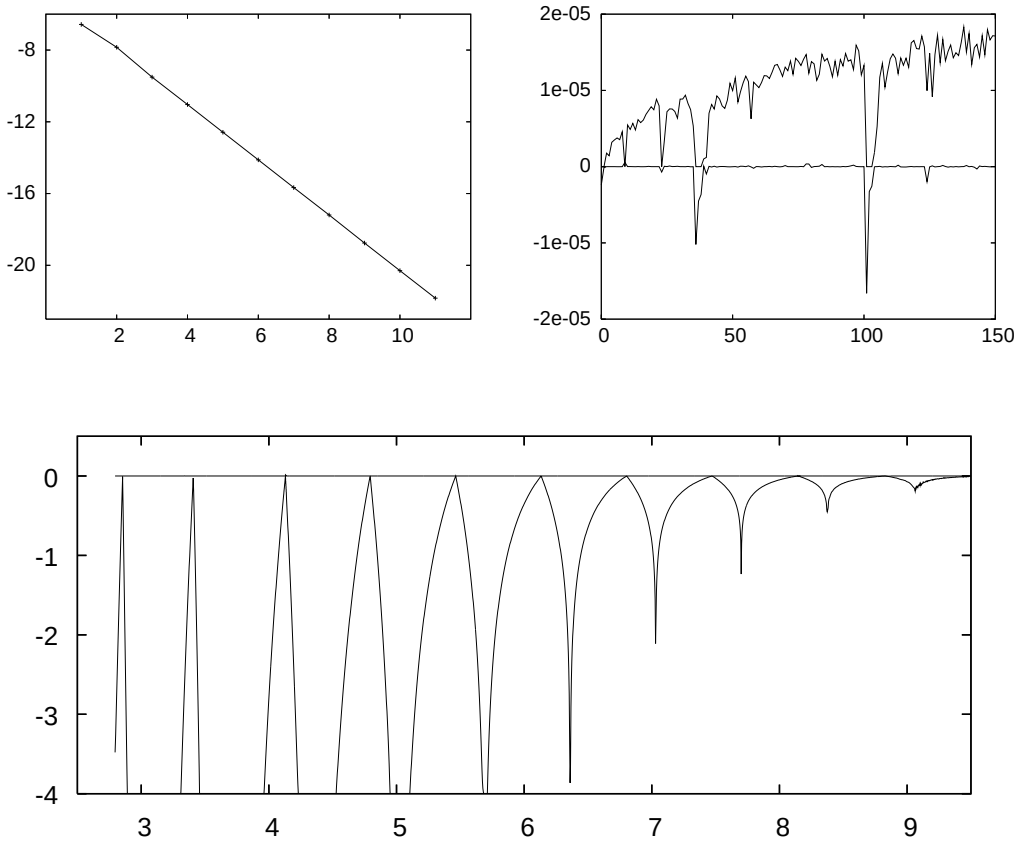

Figure B.1. Top left: $\log(\ell - \gamma_n)$ is plotted as a function of n, where $\ell \approx 0.99715033413$ is the estimated limit of the cascade. Top right: Lyapunov exponents after the end of the cascade as a function of γ. The horizontal variable is $10^{10} \times (\gamma - 0.997150334)$. Bottom: The cascade is visualised by plotting the first two Lyapunov exponents, multiplied by 10^4, as a function of $-\log_{10}(\ell - \gamma)$.

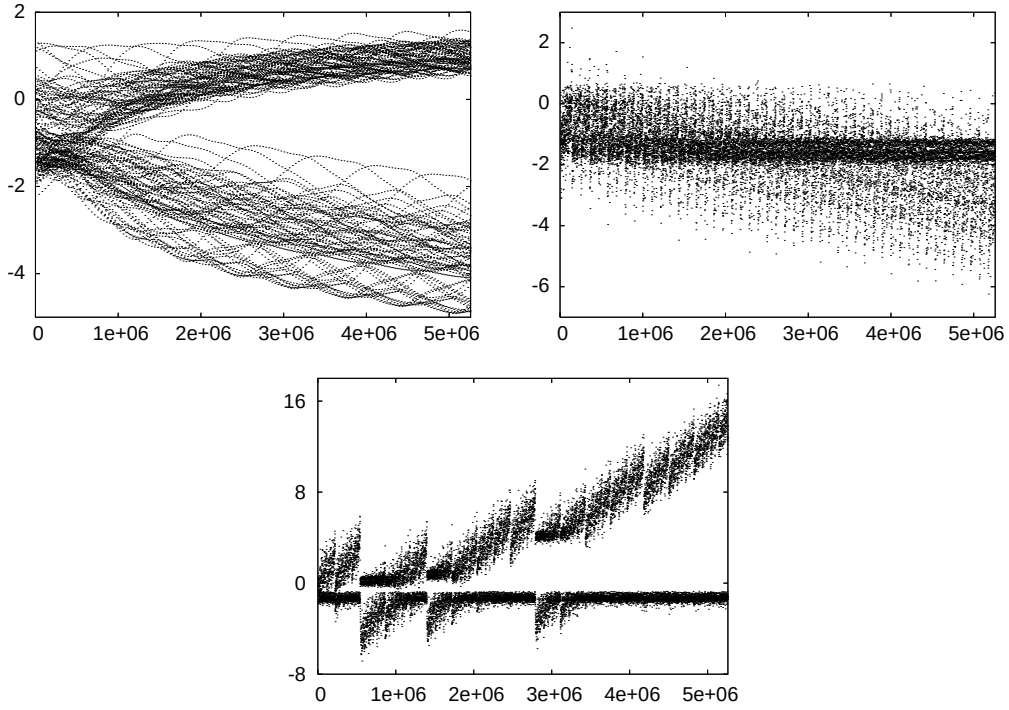

Figure B.2. First two Lyapunov sums as a function of time. A transient with $L = 10^6$ followed by $M = 10^6$ additional iterates of the Poincaré map has been used. Only one point every 100 iterates is plotted. Top left: The value of γ is close to γ_4. Top right: The value of γ is close to γ_{10}. Bottom: $\gamma = 0.997150335$, after the end of the period doubling cascade.

Bibliography

Ambaum, M.H.P. (2008), Unimodality of Wave Amplitude in the Northern Hemisphere, *Journal of the Atmospheric Sciences* **65**, pp. 1077–1086.

Athanasiadis, P.J. and Ambaum, M.H.P. (2010), Do High-Frequency Eddies Contribute to Low-Frequency Teleconnection Tendencies?, *Journal of the Atmospheric Sciences* **67**, pp. 419–433.

Bannon, P.R. (1983), Quasi-geostrophic frontogenesis over topography, *Journal of the Atmospheric Sciences* **40**, pp. 2266–2277.

Baur, F. (1951), Extended range weather forecasting, *in* T.F. Malone (ed.), *Compendium of Meteorology*, American Meteorlogical Society, pp. 814–833.

Benedict, J.J., Lee, S. and Feldstein, S.B. (2004), Synoptic View of the North Atlantic Oscillation, *Journal of the Atmospheric Sciences* **61**, pp. 121–144.

Benettin, G., Galgani, L., Giorgilli, A. and Strelcyn, J.-M. (1980a), Lyapunov characteristic exponents for smooth dynamical systems and for Hamiltonian systems; a method for computing all of them. Part 1: theory, *Meccanica* **15**, pp. 9–20.

Benettin, G., Galgani, L., Giorgilli, A. and Strelcyn, J.-M. (1980b), Lyapunov characteristic exponents for smooth dynamical systems and for Hamiltonian systems; a method for computing all of them. Part 2: numerical application, *Meccanica* **15**, pp. 21–30.

Benzi, R., Malguzzi, P., Speranza, A. and Sutera, A. (1986), The statistical properties of general atmospheric circulation: observational evidence and a minimal theory of bimodality, *Quartly Journal of the Royal Meteorological Society* **112**, pp. 661–674.

Benzi, R. and Speranza, A. (1989), Statistical properties of low frequency variability in the Northern Hemisphere, *Journal of Climate* **2**, pp. 367–379.

Benzi, R., Speranza, A. and Sutera, A. (1986), A Minimal Baroclinic Model for the Statistical Properties of Low-Frequency Variability, *Journal of the Atmospheric Sciences* **43**, pp. 2962–2967.

Broer, H.W., Dijkstra, H.A, Simó, C., Sterk, A.E. and Vitolo, R. (2010), The dynamics of a low-order model for the Atlantic Multidecadal Oscillation. Discrete and Continuous Dynamical Systems B (to appear).

Broer, H.W., Huitema, G.B. and Sevryuk, M.B. (1996), *Quasi-Periodic Motions in Families of Dynamical Systems; Order amidst Chaos*, Vol. 1645 of *Lecture Notes in Mathematics*, Springer.

Broer, H.W., Huitema, G.B., Takens, F. and Braaksma, B.L.J. (1990), *Unfoldings and bifurcations of quasi-periodic tori*, Vol. 83 of *Memoirs of the American Mathematical Society*, American Mathematical Society.

Broer, H.W., Roussarie, R. and Simó, C. (1993), On the Bogdanov-Takens bifurcation for planar diffeomorphisms, *in* C. Perelló, C. Simó and J. Solà-Morales (eds), *Equadiff 1991, Proceedings Western European Conference on Differential Equations, Barcelona 1991*, World Scientific, pp. 81–92.

Broer, H.W. and Sevryuk, M.B. (2009), KAM theory: quasi-periodicity in dynamical systems. To appear as a handbook chapter. Available at:
`http://www.math.rug.nl/~broer/pdf/Ultimate.pdf`.

Broer, H.W. and Simó, C. (1998), Hill's equation with quasi-periodic forcing: resonance tongues, instability pockets and global phenomena, *Bulletin of the Brazilian Mathematical Society* **29**, pp. 253–293.

Broer, H.W., Simó, C. and Tatjer, J.C. (1998), Towards global models near homoclinic tangencies of dissipative diffeomorphisms, *Nonlinearity* **11**, pp. 667–770.

Broer, H.W., Simó, C. and Vitolo, R. (2002), Bifurcations and strange attractors in the Lorenz-84 climate model with seasonal forcing, *Nonlinearity* **15**, pp. 1205–1267.

Broer, H.W., Simó, C. and Vitolo, R. (2005), Quasi-periodic Hénon-like attractors in the Lorenz-84 climate model with seasonal forcing, *in* F. Dumortier, H.W. Broer, J. Mahwin, A. Vanderbauwhede and S.M. Verduyn-Lunel (eds), *Equadiff 2003, Proceedings International Conference on Differential Equations, Hasselt 2003*, World Scientific, pp. 714–719.

Broer, H.W., Simó, C. and Vitolo, R. (2008a), Hopf saddle-node bifurcation for fixed points of 3D-diffeomorphisms: Analysis of a resonance 'bubble', *Physica D* **237**, pp. 1773–1799.

Broer, H.W., Simó, C. and Vitolo, R. (2008b), The Hopf-saddle-node bifurcation for fixed points of 3D-diffeomorphisms: the Arnol′d resonance web, *Bulletin of the Belgian Mathematical Society Simon Stevin* **15**, pp. 769–787.

Broer, H.W., Simó, C. and Vitolo, R. (2010), Chaos and quasi-periodicity in diffeomorphisms of the solid torus, *Discrete and Continuous Dynamical Systems B* **14**, pp. 871–905.

Broer, H.W. and Takens, F. (2010), *Dynamical Systems and Chaos*, Vol. 172 of *Applied Mathematical Sciences*, Springer.

Broer, H.W. and Vitolo, R. (2008), Dynamical systems modelling of low-frequency variability in low-order atmospheric models, *Discrete and Continuous Dynamical Systems B* **10**, pp. 401–419.

Cayan, D.R. (1992a), Latent and Sensible Heat Flux Anomalies over the Northern Oceans: Driving the Sea Surface Temperature, *Journal of Physical Oceanography* **22**, pp. 859–881.

Cayan, D.R. (1992b), Latent and Sensible Heat Flux Anomalies over the Northern Oceans: The Connection to Monthly Atmospheric Cirulation, *Journal of Climate* **5**, pp. 354–369.

Cessi, P. and Speranza, A. (1985), Orographic Instability of Nonsymmetric Baroclinic Flows and Nonpropagating Planetary Waves, *Journal of the Atmospheric Sciences* **42**, pp. 2585–2596.

Charney, J.G. and DeVore, J.G. (1979), Multiple Flow Equilibria in the Atmosphere and Blocking, *Journal of the Atmospheric Sciences* **36**, pp. 1205–1216.

Charney, J.G. and Eliassen, A. (1949), A Numerical Method for Predicting the Perturbations of the Middle-Latitude Westerlies, *Tellus* **1**, pp. 38–54.

Chen, F. and Ghil, M. (1995), Interdecadal Variability of the Thermohaline Circulation and High-Latitude Surface Fluxes, *Journal of Physical Oceanography* **25**, pp. 2547–2568.

Chenciner, A. (1985a), Bifurcations de points fixes elliptiques I. Courbes invariantes, *Publications Mathématiques de L'IHÉS* **61**, pp. 67–127.

Chenciner, A. (1985b), Bifurcations de points fixes elliptiques II. Orbites péridiques et ensembles de Cantor invariants, *Inventiones mathematicae* **80**, pp. 81–106.

Chenciner, A. (1988), Bifurcations de points fixes elliptiques III. Orbites péridiques de "petites" périodes et élimination résonnante des couples de courbes invariantes, *Publications Mathématiques de L'IHÉS* **66**, pp. 5–91.

Colin de Verdière, A. and Huck, T. (1999), Baroclinic Instability: An Oceanic Wavemaker for Interdecadal Variability, *Journal of Physical Oceanography* **29**, pp. 893–910.

Corti, S., Molteni, F. and Palmer, T.N. (1999), Signature of recent climate change in frequencies of natural atmospheric circulation regimes, *Nature* **398**, pp. 799–802.

Crommelin, D.T. (2002), Homoclinic Dynamics: A Scenario for Atmospheric Ultralow-Frequency Variability, *Journal of the Atmospheric Sciences* **59**, pp. 1533–1549.

Crommelin, D.T. (2003), Regime Transitions and Heteroclinic Connections in a Barotropic Atmosphere, *Journal of the Atmospheric Sciences* **60**, pp. 229–246.

Crommelin, D.T., Opsteegh, J.D. and Verhulst, F. (2004), A Mechanism for Atmospheric Regime Behavior, *Journal of the Atmospheric Sciences* **61**, pp. 1406–1419.

de Swart, H.E. (1989), Analysis of a six-component atmospheric spectral model: chaos, predictability and vacillation, *Physica D* **36**, pp. 222–234.

Delworth, T.L. and Mann, M.E. (2000), Observed and simulated multidecadal variability in the Northern Hemisphere, *Climate Dynamics* **16**, pp. 661–676.

Devaney, R.L. (1989), *An Introduction to Chaotic Dynamical Systems*, second edn, Westview press.

Díaz, L.J., Rios, I.L. and Viana, M. (2001), The intermittency route to chaotic dynamics, *in* H.W. Broer, B. Krauskopf and G. Vegter (eds), *Global analysis of dynamical systems; Festschrift dedicated to Floris Takens for his 60th birthday*, Institute of Physics Publishing.

Dieci, L. (2002), Jacobian Free Computation of Lyapunov Exponents, *Journal of Dynamics and Differential Equations* **14**, pp. 697–717.

Dieci, L., Russel, R.D. and van Vleck, E.S. (1997), On the Computation of Lyapunov Exponents for Continuous Dynamical Systems, *SIAM Journal on Numerical Analysis* **34**, pp. 402–423.

Dijkstra, H.A. (2005), *Nonlinear Physical Oceanography: A Dynamical Systems Approach to the Large Scale Ocean Circulation and El Niño*, second edn, Springer.

Dijkstra, H.A. (2006), Interaction of SST Modes in the North Atlantic Ocean, *Journal of Physical Oceanography* **36**, pp. 286–299.

Dijkstra, H.A. (2008), *Dynamical Oceanography*, Springer.

Dijkstra, H.A., Frankcombe, L.M. and von der Heydt, A.S. (2008), A Stochastic Dynamical Systems View of the Atlantic Multidecadal Oscillation, *Philosophical Transactions of the Royal Society A* **366**, pp. 2545–2560.

Dijkstra, H.A., Te Raa, L.A., Schmeits, M. and Gerrits, J. (2006), On the physics of the Atlantic Multidecadal Oscillation, *Ocean Dynamics* **56**, pp. 36–50.

Doedel, E.J. and Oldeman, B.E.: 2007, *AUTO–07p: continuation and bifurcation software for ordinary differential equations*, Concordia University, Montreal, Canada.

Dole, R.M. (1983), Persistent anomalies of the extratropical Northern Hemisphere wintertime circulation, *in* B.J. Hoskins and R.P. Pearce (eds), *Large-scale Dynamical Processes in the Atmosphere*, Elsevier, pp. 95–109.

Dole, R.M. (1986), The life cycles of persistent anomalies and blocking over the North Pacific, *in* R. Benzi, B. Saltzman and A. Wiin-Nielsen (eds), *Advances in Geophysics*, Vol. 29, Academic Press, pp. 31–69.

Enfield, D.B., Mestas-Nuñez, A.M. and Trimble, P.J. (2001), The Atlantic multidecadal oscillation and its relation to rainfall and river flows in the continental U.S., *Geophysical Research Letters* **28**, pp. 2077–2080.

Fraedrich, K. and Böttger, H. (1978), A Wavenumber-Frequency Analysis of the 500 mb Geopotential at 50°N, *Journal of the Atmospheric Sciences* **35**, pp. 745–750.

Frankcombe, L.M., Dijkstra, H.A. and von der Heydt, A.S. (2009), Noise Induced Multidecadal Variability in the North Atlantic: Excitation of Normal Modes, *Journal of Physical Oceanography* **39**, pp. 220–233.

Frigo, M. and Johnson, S.G. (2005), The Design and Implementation of FFTW3, *Proceedings of the IEEE*, Vol. 93, pp. 216–231.

Goldenberg, S.B., Landsea, C.W., Mestas-Nuñez, A.M. and Gray, W.M. (2001), The Recent Increase in Atlantic Hurricane Activity: Causes and Implications, *Science* **293**, pp. 474–479.

Greatbatch, R.J. and Zhang, S. (1995), An Interdecadal Oscillation in an Idealized Ocean Basin Forced by Constant Heat Flux., *Journal of Climate* **8**, pp. 81–91.

Griffies, S.M. and Tziperman, E. (1995), A Linear Thermohaline Oscillator Driven by Stochastic Atmospheric Forcing, *Journal of Climate* **8**, pp. 2240–2453.

Guckenheimer, J. and Holmes, P. (1983), *Nonlinear oscillations, dynamical systems and bifurcations of vector fields*, Vol. 42 of *Applied Mathematical Sciences*, Springer.

Hansen, A.R. and Sutera, A. (1986), On the Probability Density Distribution of Planetary-Scale Atmospheric Wave Amplitude, *Journal of the Atmospheric Sciences* **43**, pp. 3250–3265.

Hansen, A.R. and Sutera, A. (1995), The Probability Density Distribution of Planetary-Scale Atmospheric Wave Amplitude Revisited, *Journal of the Atmospheric Sciences* **52**, pp. 2463–2472.

Hasselmann, K. (1976), Stochastic climate models. Part I. Theory, *Tellus* **28**, pp. 473–485.

Held, I.M. (2005), The Gap between Simulation and Understanding in Climate Modeling, *Bulletin of the American Meteorological Society* pp. 1609–1614.

Holton, J.R. (2004), *Introduction to dynamic meteorology*, Vol. 88 of *International Geophysics Series*, fourth edn, Elsevier Academic Press.

Hovmöller, E. (1949), The Trough and Ridge Diagram, *Tellus* **1**, pp. 62–66.

Huck, T. and Vallis, G.K. (2001), Linear stability analysis of the three-dimensional thermally-driven ocean circulation: application to interdecadal oscillations, *Tellus A* **53**, pp. 526–545.

Itoh, H. (1983), An observational study of the amplification of the planetary waves in the troposhere, *Journal of the Meteorological Society Japan* **61**, pp. 568–589.

Jorba, À. (2001), Numerical computation of the normal behaviour of invariant curves of n-dimensional maps, *Nonlinearity* **14**, pp. 943–976.

Jorba, À. and Zou, M. (2005), A Software Package for the Numerical Integration of ODEs by Means of High-Order Taylor Methods, *Experimental Mathematics* **14**, pp. 99–117.

Juel, A., Darbyshire, A.G. and Mullin, T. (1997), The effect of noise on pitchfork and hopf bifurcations, *Proceedings: Mathematical, Physical and Engineering Sciences* **453**, pp. 2627–2647.

Kerr, R.A. (2000), A North Atlantic Climate Pacemaker for the Centuries, *Science* **288**, pp. 1984–1985.

Kushnir, Y. (1994), Interdecadal Variations in North Atlantic Sea Surface Temperature and Associated Atmospheric Conditions, *Journal of Climate* **7**, pp. 141–157.

Kuznetsov, Yu.A. (2004), *Elements of applied bifurcation theory*, Vol. 112 of *Applied Mathematical Sciences*, third edn, Springer.

Legras, B. and Ghil, M. (1985), Persistent Anomalies, Blocking and Variations in Atmospheric Predictability, *Journal of the Atmospheric Sciences* **42**, pp. 433–471.

Lorenz, E.N. (1967), *The Nature and Theory of the General Circulation of the Atmosphere*, World Meteorological Organization. Available at `http://eapsweb.mit.edu/research/Lorenz/publications.htm`.

Lorenz, E.N. (1980), Attractor Sets and Quasi-Geostrophic Equilibrium, *Journal of the Atmospheric Sciences* **37**, pp. 1685–1699.

Lucarini, V., Calmanti, S., Dell'Aquila, A., Ruti, P.M. and Speranza, A. (2007), Intercomparison of the northern hemisphere winter mid-latitude atmospheric variability of the IPCC models, *Climate Dynamics* **28**, pp. 829–848.

Lucarini, V., Speranza, A. and Vitolo, R. (2007), Parametric smoothness and self-scaling of the statistical properties of a minimal climate model: What beyond the mean field theories?, *Physica D* **234**, pp. 105–123.

Majda, A.J., Franzke, C.L., Fischer, A. and Crommelin, D.T. (2006), Distinct metastable atmospheric regimes despite nearly Gaussian statistics: A paradigm model, *Proceedings of the National Academy of Sciences* **103**, pp. 8309–8314.

Malguzzi, P. and Speranza, A. (1981), Local Multiple Equilibria and Regional Atmospheric Blocking, *Journal of the Atmospheric Sciences* **38**, pp. 1939–1948.

Malguzzi, P., Speranza, A., Sutera, A. and Caballero, R. (1996), Nonlinear Amplification of Stationary Rossby Waves Near Resonance. Part I, *Journal of the Atmospheric Sciences* **53**, pp. 298–311.

Malguzzi, P., Speranza, A., Sutera, A. and Caballero, R. (1997), Nonlinear Amplification of Stationary Rossby Waves Near Resonance. Part II, *Journal of the Atmospheric Sciences* **54**, pp. 2441–2451.

Mo, K. and Ghil, M. (1988), Cluster Analysis of Multiple Planetary Flow Regimes, *Journal of Geophysical Research* **93**, pp. 10927–10952.

Neishtadt, A.I., Simó, C. and Treschev, D.V. (1995), *On stability loss delay for a periodic trajectory*, Vol. 19 of *Progress in nonlinear differential equations and their applications*, Birkhauser–Verlag, pp. 253–278.

Nitsche, G., Wallace, J.M. and Kooperberg, C. (1994), Is There Evidence of Multiple Equilibria in Planetary Wave Amplitude Statistics?, *Journal of the Atmospheric Sciences* **51**, pp. 314–322.

Palis, J. and Takens, F. (1993), *Hyperbolicity & sensitive chaotic dynamics at homoclinic bifurcations*, Cambridge University Press.

Palmer, T.N., Doblas-Reyes, F.J., Weisheimer, A. and Rodwell, M.J. (2008), Toward Seamless Prediction: Calibration of Climate Change Projections Using Seasonal Forecasts, *Bulletin of the American Meteorological Society* **89**, pp. 459–470.

Pomeau, Y. and Manneville, P. (1980), Intermittent Transition to Turbulence in Dissipative Dynamical Systems, *Communications in Mathematical Physics* **74**, pp. 189–197.

Puigjaner, D., Herrero, J., Giralt, F. and Simó, C. (2004), Stability analysis of the flow in a cubical cavity heated from below, *Physics of Fluids* **16**, pp. 3639–3655.

Puigjaner, D., Herrero, J., Giralt, F. and Simó, C. (2006), Bifurcation analysis of multiple steady flow patterns for Rayleigh-Bénard convection in a cubical cavity at $Pr = 130$, *Physical Review E* **73**. 046304.

Puigjaner, D., Herrero, J., Simó, C. and Giralt, F. (2008), Bifurcation analysis of steady Rayleigh–Bénard convection in a cubical cavity with conducting sidewalls, *Journal of Fluid Mechanics* **598**, pp. 393–427.

Reinhold, B. (1987), Weather Regimes: The Challenge in Extended-Range Forecasting, *Science* **235**, pp. 437–441.

Rex, D.F. (1950), Blocking Action in the Middle Troposphere and its Effect upon Regional Climate. Part 2: The Climatology of Blocking Action, *Tellus* **2**, pp. 275–301.

Ruti, P.M., Lucarini, V., Dell'Aquila, A., Calmanti, S. and Speranza, A. (2006), Does the subtropical jet catalyze the midlatitude atmospheric regimes?, *Geophysical Research Letters* **33**. L06814.

Saravanan, R. and McWilliams, J.C. (1998), Advective Ocean-Atmosphere Interaction: an Analytical Stochastic Model with Implications for Decadal Variability, *Journal of Climate* **11**, pp. 165–188.

Simó, C. (1990), On the analytical and numerical continuation of invariant manifolds, *in* D. Benest and C. Froeschlé (eds), *Modern Methods in Celestial Mechanics*, Éditions Frontières, pp. 285–330.

Simó, C. (2005), On the use of Lyapunov exponents to detect global properties of the dynamics, *in* F. Dumortier, H.W. Broer, J. Mahwin, A. Vanderbauwhede and S.M. Verduyn-Lunel (eds), *Equadiff 2003, Proceedings International Conference on Differential Equations, Hasselt 2003*, World Scientific, pp. 631–636.

Speranza, A. and Malguzzi, P. (1988), The Statistical Properties of a Zonal Jet in a Baroclinic Atmosphere: A Semilinear Approach. Part I: Quasi-geostrophic, Two-Layer Model Atmosphere, *Journal of the Atmospheric Sciences* **45**, pp. 3046–3061.

Stephenson, D.B., Hannachi, A. and O'Neill, A. (2004), On the existence of multiple climate regimes, *Quartly Journal of the Royal Meteorological Society* **130**, pp. 583–605.

Sterk, A.E., Vitolo, R., Broer, H.W., Simó, C. and Dijkstra, H.A. (2010), New nonlinear mechanisms of midlatitude atmospheric low-frequency variability, *Physica D* **239**, pp. 702–718.

Takens, F. (1987), Intermittancy; global aspects, *Technical Report ZW–8703*, University of Groningen.

Te Raa, L.A. and Dijkstra, H.A. (2002), Instability of the Thermohaline Ocean Circulation on Interdecadal Timescales, *Journal of Physical Oceanography* **32**, pp. 138–160.

Te Raa, L.A. and Dijkstra, H.A. (2003), Modes of internal thermohaline variability in a single-hemispheric ocean basin, *Journal of Marine Research* **61**, pp. 491–516.

Te Raa, L.A., Gerrits, J. and Dijkstra, H.A. (2004), Identification of the Mechanism of Interdecadal Variability in the North Atlantic Ocean, *Journal of Physical Oceanography* **34**, pp. 2792–2807.

Van der Avoird, E., Dijkstra, H.A., Nauw, J.J. and Schuurmans, C.J.E. (2002), Nonlinearly induced low-frequency variability in a midlatitude coupled ocean-atmosphere model of intermediate complexity, *Climate Dynamics* **19**, pp. 303–320.

Van Veen, L. (2003), Baroclinic flow and the Lorenz-84 model, *International Journal of Bifurcation and Chaos* **13**, pp. 2117–2139.

Vitolo, R., Broer, H.W. and Simó, C. (2010), Routes to chaos in the Hopf-saddle-node bifurcation for fixed points of 3D-diffeomorphisms, *Nonlinearity* **23**, pp. 1919–1947.

Wieczorek, S., Krauskopf, B. and Lenstra, D. (2001), Unnested islands of period doublings in an injected semiconductor laser, *Physical Review E* **64**. 056204.

Zeeman, E.C. (1982), Bifurcation, catastrophe and turbulence, *in* P.J. Hilton and G.S. Young (eds), *New Directions in Applied Mathematics: Papers Presented April 25–26, 1980 on the Occasion of the Case Centennial Celebration*, Springer Verlag, pp. 109–153.

Samenvatting

Observaties van de oppervlaktetemperatuur van de Noord-Atlantische Oceaan bevatten aanwijzingen voor schommelingen met een tijdschaal van enkele decennia. Deze variabiliteit wordt ook wel aangeduid als de Atlantische Multidecadale Oscillatie (AMO). Modellen voor de grootschalige oceaancirculatie suggereren dat het patroon van de oppervlaktetemperatuur en de tijdschaal van de AMO worden verklaard door variaties in de thermohaliene circulatie. De amplitude van de AMO wordt echter vermoedelijk bepaald door de bovenliggende atmosfeer.

In dit proefschrift onderzoeken we (1) de dynamica van laagfrequente variabiliteit van de atmosfeer op gemiddelde noorderbreedte en (2) het effect daarvan op de AMO. Daartoe bestuderen we zogenaamde *lage-orde modellen*. Deze modellen worden afgeleid door de (onbekende) oplossing van een stelsel partiële differentiaalvergelijkingen te projecteren op een geschikt gekozen eindig-dimensionale functieruimte. De dynamica van de aldus verkregen modellen wordt bestudeerd in het raamwerk van de wiskundige theorie van dynamische systemen. Door het systematisch bestuderen van aantrekkers en hun bifurcaties wordt een coherent beeld van de dynamica verkregen. Van bijzonder belang zijn de overgangen van ordelijke naar meer gecompliceerde of zelfs chaotische dynamica.

De drie belangrijkste resultaten van het onderzoek zijn (1) een nieuw dynamisch scenario voor atmosferische laagfrequente variabiliteit waarbij vreemde aantrekkers onregelmatige atmosferische planetaire golven representeren, (2) een sterk vereenvoudigd model dat de kwalitatieve eigenschappen van de AMO beschrijft en (3) een deterministisch mechanisme waarbij de AMO wordt aangedreven door een chaotische atmosfeer.

Atmosferische laagfrequente variabiliteit. In Hoofdstuk 2 bestuderen we de dynamica van een lage-orde model voor de planetaire atmosferische circulatie op gemiddelde noorderbreedte. Evenwichtstoestanden worden onstabiel via een Hopf bifurcatie waarna we een periodieke aantrekker vinden. Deze periodieke aantrekker kan vervolgens drie bifurcatiescenarios ondergaan: (1) een cascade van periodeverdubbelingen,

(2) een Hopf-Neĭmark-Sacker bifurcatie gevolgd door de vernietiging van de invariante torus en (3) intermittentie geassocieerd met de zadel-knoop bifurcatie van de periodieke aantrekker.

De periodieke aantrekkers representeren atmosferische planetaire golven met fysische karakteristieken die kwalitatief overeenkomen met observaties. De vreemde aantrekkers die ontstaan na de voorgenoemde bifurcatiescenarios zijn onregelmatige planetaire golven die hun fysische karakteristieken 'erven' van de periodieke aantrekkers.

De Atlantische Multidecadale Oscillatie. In Hoofdstuk 3 bestuderen we een lage-orde model voor thermisch aangedreven oceaanstromingen. Als de atmosferische demping op temperatuuranomalieën aan het oppervlak beneden een kritieke waarde komt, wordt een evenwichtstoestand onstabiel door een Hopf bifurcatie en vinden we een periodieke aantrekker met fysische karakteristieken die kwalitatief overeenkomen met de karakteristieken van de AMO.

Door middel van een Poincaré sectie bestuderen we de bifurcaties van de periodieke aantrekker. Met het toenemen van het noord-zuid verschil van de atmosferische temperatuur, verliest de periodieke aantrekker haar stabiliteit en ondergaat periodeverdubbelingen. Cascades van deze bifurcaties leiden tot vreemde aantrekkers van *Hénon-achtig* type: deze worden gevormd door de afsluiting van de onstabiele variëteit van een periodieke baan van zadel type.

Vervolgens modelleren we het effect van jaarlijkse variabiliteit van de warmtefluxen over het oppervlak van de Noord-Atlantische Oceaan door een periodieke aandrijving te introduceren. Het periodiek aangedreven model bestuderen we door over te gaan op een *stroboscopische afbeelding*. Naast periodieke aantrekkers vinden we nu ook invariante cirkels met quasi-periodieke dynamica. De periodeverdubbelingen in het autonome systeem worden nu quasi-periodieke verdubbelingen, dat wil zeggen verdubbelingen van de invariante cirkel. Deze bifurcaties leiden tot vreemde aantrekkers die vermoedelijk van *quasi-periodiek Hénon-achtig* type zijn: deze worden gevormd door de afsluiting van de onstabiele variëteit van een quasi-periodieke invariante cirkel van zadel type.

Atmosferische excitatie van de AMO. In Hoofdstuk 3 moet steeds de atmosferische demping voldoende laag zijn om AMO-achtige oscillaties te vinden. De verwachting is dat een realistische atmosferische demping hoger is dan in ons model waardoor dergelijke oscillaties uiteindelijk uitsterven. In Hoofdstuk 4 wordt onderzocht of laagfrequente variabiliteit zoals gevonden in Hoofdstuk 2 in staat is om de AMO te kunnen exciteren. Daartoe beschouwen we een scheefgekoppeld oceaan-atmosfeer

model waarbij de atmosfeer de oceaan aandrijft met een warmteflux.

In het scheefgekoppelde model worden AMO-achtige oscillaties gevonden met een atmosferische demping die *lager* is dan de kritische demping in het autonome oceaanmodel. In deze zin kunnen we spreken van excitatie van de AMO ten gevolge van atmosferische aandrijving. Vermoedelijk kan dit fenomeen worden verklaard met een vorm van intermittentie, maar wel een vorm die verschilt van de klassieke scenario's die beschreven zijn in de literatuur.